NTNU

Norwegian University of
Science and Technology

Estimation of Timeshifts and Velocity Changes from 4D Seismic Analysis: A Case Study from the Norne Field

Lene Lykke Erichsen

Petroleum Geoscience and Engineering
Submission date: June 2018
Supervisor: Kenneth Duffaut, IGP

Norwegian University of Science and Technology
Department of Geoscience and Petroleum

Abstract

The scope of this thesis is to investigate whether it is possible to determine the vertical strain in the overburden directly from the 4D seismic data from the Norne field in the Norwegian sea, by using changes in traveltime and amplitudes. This will be a new approach to the problem and represent an alternative to the common approach which is to estimate vertical strain in a dedicated numerical geomechanical model that is used in combination with 4D seismic data.

The data was analyzed using two different methods. Method 1 keeps the seafloor constant and calculates the timeshifts, relative timeshifts and relative velocity changes from the seafloor and down to each interpreted horizon. Thus, the thickness of the intervals increase with depth. Method 2 calculates the timeshifts, relative timeshifts and relative velocity changes between each interpreted horizon, thus the intervals are more unison in thickness.

Both Method 1 and 2 yields the same results when it comes to accumulated timeshifts and accumulated relative timeshifts, while the results for the accumulated relative velocity changes are different when using the two methods.

The calculated strain in this thesis is defined as a product of the relative timeshifts and the relative velocity change and gives the fractional change in thickness of the analyzed interval. Thus, the strain calculation only use data that is obtained directly from the 4D seismic datasets, skipping the geomechanical model.

If the uncertainty of the ΔA Cube and relative velocity changes are disregarded, the calculated strain yielded by Method 2 is more reliable than Method 1 because the strain is not accumulated through the overburden and instead calculated separately in every interval. Thus, a possible miscalculation in a shallow interval does not affect the calculated strain in a deeper interval.

Sammendrag

Formålet med denne masteroppgaven har vært å undersøke om det er mulig å beregne relativ tykkelsesendring i overlagringen over et hydrokarbonfylt reservoar direkte, ved å bruke endringer i gangtid og amplituder, med utgangspunkt i 4D seismikk fra Norne-feltet i Norskehavet. Metoden er ny for vurdering av problemet og er et alternativ til den vanlige fremgangsmåten der relativ tykkelsesendring beregnes ved hjelp av en geomekanisk modell i kombinasjon med 4D seismikk.

Dataene er analysert ved hjelp av to ulike metoder. Metode 1 holder havbunnen konstant og beregner tidsskift, relative tidsskift og relativ hastighetsendring fra havbunnen og ned til hver tolket horisont. Dermed øker tykkelsen på intervallene med dyp. Metode 2 beregner tidsskift, relativ tidsskift og relativ hastighetsendring mellom hver tolket horisont, og dermed er tykkelsen på intervallene relativt lik.

Både Metode 1 og 2 gir de samme resultatene når det gjelder akkumulerte tidsskift og akkumulerte relative tidsskift, mens resultatene for akkumulert relativ hastighetsendring er ulike ved bruk av de to metodene.

Den beregnede tykkelsesendringen i denne masteroppgaven er definert som summen av de relative tidsskiftene og den relative hastighetsendringen og gir den fraksjonelle tykkelsesendringen gjennom det analyserte intervallet. Dermed er det kun data hentet direkte fra seismikken som inngår i beregningen av den relative tykkelsesendringen, og den geomekaniske modellen er ikke lenger nødvendig.

Hvis usikkerheten knyttet til ΔA kuben og de relative hastighetsendringene ses bort ifra, er den beregnede relative tykkelsesendringen ved bruk av Metode 2 mer pålitelig enn ved bruk av Metode 1 i de områdene hvor seismikken er av høy kvalitet. Grunnen til dette er at den relative tykkelsesendringen ikke akkumuleres gjennom overlagringen ved bruk av Metode 2, men i stedet beregnes separat for hvert intervall. Dermed vil ikke en potensiell beregningsfeil i et grunt intervall påvirke beregninger i et dypere intervall.

Acknowledgements

Firts and foremost, I would like to thank my supervisor at NTNU, Kenneth Duffaut for fruitful discussion and excellent supervision throughout the semester.

I also want to thank Dicky Harishidayat for help with Petrel.

Last, but not least, I want to thank my parents and boyfriend for support and encouragement, and especially my dad Harald Erichsen for taking the time to proof read the thesis.

Long nights and hard work on this thesis have been motivated by great fellow students at NTNU.

Contents

List of Figures

List of Tables

Chapter 1

Introduction

1.1 Background

When hydrocarbons are produced from a reservoir, the extraction will, in cases with lack of pressure support from the surrounding aquifer or through injection of water and/or gas, deplete. The pressure depletion may in some cases cause the reservoir to compact, inducing subsidence at the seabed according to the degree of compaction. The seabed and reservoir will not experience the same vertical displacement, and as a consequence, stretching of the overburden will occur. The stretch will lead to a change in the thickness of the overburden, which again will result in changes in the overburden's seismic attributes such as traveltime, wave velocity and pore pressure, as stated by both Landrø [10] and Hatchell [11].

Due to the induced subsidence of the seabed or land surface, the reservoir compaction may be up to several centimeters per year, depending of the reservoir rock type. Røste [12] stated that compaction of a sandstone reservoir yields smaller overburden timeshifts than compaction of a chalk reservoir due to the difference in rock stiffness, making it more difficult to interpret the timeshifts in a sandstone than a chalk reservoir.

Reservoir compaction is an important drive mechanism and can result in significant improvement of the recovery factor in a field compared to estimatates performed without taking compaction into consideration.

However, compaction can also have negative consequences such as seabed subsidence and collapsing casing and tubing in the production and injection wells. As a consequence, significant investments have been done in fields where the reservoir compaction have influenced the infrastructure negatively, such as the Ekofisk and Valhall fields in the Norwegian North sea.

A good understanding of reservoir compaction and how it impacts the overburden is important for a number of reasons, including but not limited to the following [12]:

- Proper dynamic reservoir modelling that reflects the effect of compaction. This will be important for field development planning purposes to optimize the development concept
- Well design and planning to minimize the negative effects of compaction and stretch on the casing and tubing
- Provide a good estimate of the subsidence due to compaction, so that this can be taken into account in the design phase for a field development in order to minimize the negative effects on health, safety and environment (HSE)

By using seismic time lapse data, also known as 4D seismic, where the exact seismic surveys are repeated over time, it is possible to detect physical changes in the reservoir and overburden during the field lifetime [12]. The compaction of the reservoir will be visible on the 4D seismic data as timeshifts in the two-way traveltimes, and as changes in reservoir parameters such as fluid composition and interfaces [13].

The time shift refers to the summation of all the traveltime differences between seismic surveys experienced in the overlying layers [14], and include effects of changes in both velocity and thickness within a layer [10]. The time shift can be expressed as the difference between the change in thickness and the pressure change related P-wave velocity in a given layer, see equation (1.1) below. The equation relates the change in two-way traveltime to the change in thickness and P-wave velocity from one timestep to another [10].

$$\frac{\Delta t}{t} = \frac{\Delta z}{z} - \frac{\Delta V_p^P}{\bar{V_p}}, \tag{1.1}$$

where t represents the two-way traveltime, z represents the thickness and V_p^P represents the P-wave velocity.

The information obtained from a 4D seismic survey is the fractional change in traveltime ($\frac{\Delta t}{t}$), implying that the fractional change in both thickness ($\frac{\Delta z}{z}$) and velocity ($\frac{\Delta V_p}{V_p}$) are unknown. Thus, a common approach is to determine the changes in velocity and thickness based on the 4D seismic and a geomechanical model.

Previously it have been assumed that the overburden behaves uniformly, thus the thickness-term have been substituted by a R-factor [11, 15] expressed as follows

$$R = -\frac{\frac{\Delta V_p}{V_p}}{\frac{\Delta z}{z}}, \tag{1.2}$$

where V_p represents the P-wave velocity and z represents the thickness. By substituting (1.2) into (1.1) the traveltime function can be rewritten into

$$\frac{\Delta t}{t} = \frac{\Delta z}{z}\big(R+1\big), \tag{1.3}$$

To be able to determine the vertical strain in the overburden due to production induced pressure depletion in the reservoir, the time shifts from a 4D seismic survey are interpreted. A common approach today is to define a geomechanical model to determine the modelled vertical strain ($\frac{\Delta z}{z}$) used in addition to the 4D seismic data. It would be a major breakthrough if it was possible to determine the vertical strain without having to construct a geomechanical model, as such, determine the vertical strain directly from the seismic data.

The scope of this project is to investigate whether it is possible to determine the vertical strain in the overburden at the Norne field in the Norwegian sea, by applying changes in traveltime from one survey to the next, relative time shifts ($\frac{\Delta t}{t}$), and amplitude changes from the baseline to monitoring survey. Castagna [16] stated that the zero-offset amplitude across an interface can be expressed as

$$A = \frac{1}{2}\big(\frac{\Delta V_p}{\bar{V_p}} + \frac{\Delta \rho}{\bar{\rho}}\big) \tag{1.4}$$

By rewriting the equation to express the change in intercept from baseline to the monitoring survey and assuming that the density is constant ($\Delta\rho = 0$), equation (1.4) can be rewritten into equation (1.5) below

$$\overline{\Delta A} = \frac{1}{2}\Big(\frac{\Delta(\Delta V_p)}{\overline{V_p}}\Big) = \frac{1}{2}\left(\frac{\Delta V_{p,mon} - \Delta V_{p,base}}{\overline{V}_{p,mon}}\right) \tag{1.5}$$

where A is the intercept and V_p is the P-wave velocity of the media the wave propagates through.

The relative timeshift change for a single layer (equation 1.1) can thus be simplified to the following expression by inserting equation (1.5)

$$\left(\frac{\Delta t}{t}\right)_{layer} = \left(\frac{\Delta z}{z} - 2\overline{\Delta A}\right)_{layer} \tag{1.6}$$

For equation (1.6) to be valid through the formation, and not only in a single layer, the thickness change and intercept change as to be summed through the overburden, as expressed in the equation below

$$\sum \frac{\Delta t}{t} = \sum \left(\frac{\Delta z}{z} - 2\overline{\Delta A}\right) \tag{1.7}$$

Related work

Many attempts have been made in order to find an accurate approximation for how to determine the reservoir compaction and corresponding seabed subsidence, both with and without the use of a numerical geomechanical model.

Guilbot and Smith [17] estimated the reservoir compaction by combining an empirical relationship between porosity and velocity with 4D traveltime changes from post-stack data.

Landrø and Røste [10] estimated the compaction without using a geomechanical model. Two approaches were presented, one using impedance and traveltime changes from poststack data, and the other by using traveltime shifts on near- and far-offset prestack data.

Røste and Dypvik [15] attempted to determine the change in velocity and layer thickness by analyzing 4D prestack data.

In general, approaches that do not include use of a numerical and geomechanical model do not generate satisfying results, while approaches where a geomechanical model have been defined generate quite satisfying results.

Main Objectives

1. Seismic interpretation of main horizons on the full-stack seismic data from 2001 and 2006, which forms the basis of the further analysis

2. Calculate timeshifts, relative timeshifts and relative velocity change at all interpreted horizons using two different methods

3. Calculate the vertical strain along the three exploration wells 6608/10-2, 6608/10-3 and 6608/10-4, and compare to the relative timeshifts and relative velocity change

1.2 Approach

By performing a well-tie, tying all formation tops to the seismic data from the Norne field, and interpreting all formation tops as well as other good reflectors, it is possible to determine the change in traveltime between to interpreted reflectors from the baseline to the monitoring survey. The traveltime change, called the timeshift, can then be used to determine the relative timeshift between the two seismic surveys, as given by equation (1.8).

$$\frac{\Delta(\Delta t)}{\Delta t_{base}} = \frac{\Delta t_{mon} - \Delta t_{base}}{\Delta t_{base}} \tag{1.8}$$

Then, the seismic cubes corresponding to 2001 and 2006 are converted to intercept cubes, cubes representing traces with normal incidence angle, which are used to make a seismic cube based on the intercept change between the two datasets. The sum of the intercept change between each interpreted horizon can thus be extracted, making it possible to determine the average intercept change through each interval, as given by equation (1.9).

$$\overline{\Delta A} = \frac{\sum \overline{\Delta A}}{k} \tag{1.9}$$

where k denotes the number of samples in the analyzed interval.

By combining the fractional traveltime change and the intercept change from baseline to monitoring seismic survey as described in equation (1.5), the fractional thickness change can be detected and is given by equation (1.10).

$$\sum \frac{\Delta z}{z} = \sum \left(\frac{\Delta t}{t} + 2\overline{\Delta A} \right) \tag{1.10}$$

The report is structured as follows

- Abstract
- Sammendrag
- Acknowledgements
- Chapter 1. Introduction
- Chapter 2. Theory and Background
- Chapter 3. Methodology
- Chapter 4. Results
- Chapter 5. Discussion
- Chapter 6. Conclusion
- Chapter 6. Further Work
- Bibliography
- Appendix A
- Appendix B
- Appendix C
- Appendix D

Chapter 2

Theory and Background

In this chapter the following is provided; an introduction to the Norne data set, the theory applied in the seismic interpretation of the data, and the numerical modelling that forms the basis for the analysis which is described in the following chapters in this report.

Parts of this chapter is based on the specialization project report ¨Estimation of Vertical Strain in Overburden Using Synthetic 4D Seismic Data¨ by Erichsen, (2017) [18].

2.1 Norne field

The Norne field is an oil and gas field located in blocks 6508/1 and 6608/1 in the Nordland II area of the Norwegian Sea, as illustrated in figure 2.1. The field was discovered by Equinor in December 1991, in exploration well 6608/10-2. The field was put in production in 1997 and is still ongoing.

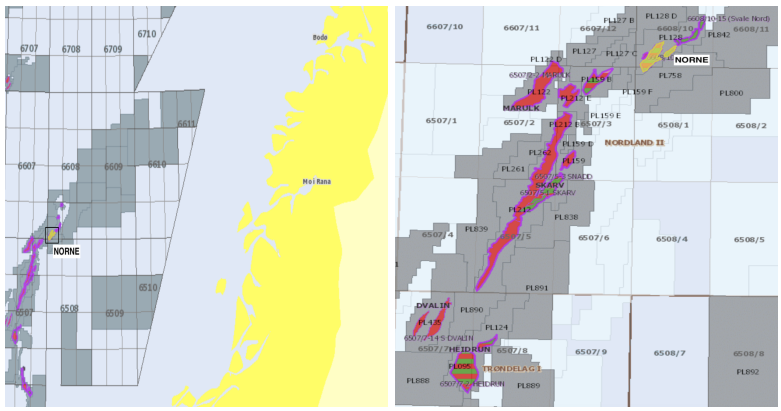

Figure 2.1: Location of the Norne field [1].

The Norne field is located in a relatively flat horst structure, approximately 9x3 km^2 in size [1, 19]. The field is located around 200 km due west of Mosjøen in Nordland, and approximately 80 km north of the Heidrun field.

The field consist of two separate compartments, the Norne Main Structure and the North-East Segment. Initially, the Norne Main Structure contained 97% of the oil and gas reserves, while the North-East Segment contained the remaining 3%. The sandstone reservoir is of Middle and Late Jurassic age, while the source rock in the Åre formation is from the Early Jurassic. The cap rock holding the hydrocarbons in place is the sealing Melke formation from early Jurassic [20].

Hydrocarbon volumes are provided in table 2.1 below [1]

	Oil	**Gas**
Recoverable reserves	93.09 mill Sm^3	12.65 bill Sm^3
Produced	90.1 mill Sm^3	7.27 bill Sm^3
Remaining	2.99 mill Sm^3	5.38 bill Sm^3
Original inplace	157.00 mill Sm^3	1.8 mill Sm^3

Table 2.1: Hydrocarbon volumes in the Norne field [1].

The reservoir consist of five formations, listed in order of increasing depth; Garn, Ile, Ror, Tofte and Tilje. Garn and Ile formations are separated by the shaly Not formation which is not a part of the reservoir. The Not formation is continuous throughout the field, preventing communication between the Garn and Ile formations. Further details can be found in table 2.2.

The reservoir fluids consist of gas and light oil with an oilzone overlain by a gas cap. Most of the gas, approximately 95%, is found in the Garn formation, while most of the oil, approximately 80%, is found in the Ile and Tofte formations. In the Garn formation, a 25 m gas column is overlying an approximately 6 m oil column above the sealing Not formation. The rest of the oil is located in the formations underlying Not, and the gross pay thickness of the oil column is 110 m. The gross pay thickness of the reservoir is 135 m in total [1].

Due to the flat horst structure, the gas cap is present throughout most of the reservoir. The reservoir as a whole is a heterolithic tidal sandstone reservoir consisting of fine-grained and well to very well sorted sub-arkosic arenites affected by diagenesis, as most of the reservoirs in the Norwegian sea. The reservoir is classified as shallow, with a burial depth ranging between 2500 and 2700 km [21], with a thickness that varies from 260 m in the south to 120 m in the north. The reservoir thickness varies because the Ile and Tilje formations in the northern part of the field have been exposed to erosion and are thinner in this area. The reservoir quality is good, with a porosity ranging from 25% to 30% and a permeability ranging between 20 mD and 2500 mD. The gas-oil-contact and oil-water-contact found in

well 6608/10-2 was 2583 m MSL and 2691 m MSL, respectively [19].

Group	Formation	Description	TVD	TWT
Nordland	Naust	Interbedded claystone, siltstone and sandstone with limestone stringers. Glauconite, pyrite and shell fragments are common.	397 m	830 ms
	Kai	Alternating claystone, siltstone and sandstone with limestone stringers. Pyrite, glauconite and shell fragments are common.	1352 m	1354 ms
Hordaland	Brygge	Claystone with stringers of sandstone, siltstone, limestone and marl. Pyrite, glauconite and shell fragments are seen in the sandstone.	1565 m	1541 ms
Rogaland	Tare	Viscous clay consisting of volcanic ash beneath a layer of sediments deposited after volcanic activity.	1857 m	1818 ms
	Tang	Dark grey to brown claystone with minor sandstone and limestone.	1913 m	1870 ms
Shetland	Springar	Marine mudstone with limestone, dolomite and sandstone stringers.	1951 m	1907 ms
	Nise	Mudstone with subordinate siltstone, sandstone and carbonate stringers.	2151 m	2081 ms
Cromer Knoll	Lyr	Light/medium grey to light greyish-green marls with interbedded carbonates.	2253 m	2162 ms

Group	Formation	Description	TVD	TWT
Viking	Spekk	Dark shale rich in organic cmatter.	2347 m	2229 ms
	Melke	Claystones with thin siltstone lamina in between.	2365 m	2246 ms
Fangst	Garn	Medium to coarse-grained sandstone deposited as prograding braided delta lobes.	2578 m	2406 ms
	Not	Mudstone dominated sequence coarsening upwards.	2611 m	2429 ms
	Ile	Fine to medium coarse-grained sandstone interbedded with thinly laminated siltsones and shales.	2619 m	2434 ms
Båt	Ror	Very fine grained to shaly unit consisting of sand. Parts of the formation is heavily bioturbated with traces of glauconite, phosphate nodules and calcareous shells.	2659 m	2460 ms
	Tofte	Depositions ranging from shales in the east to sand in the west.	2668 m	2466 ms
	Tilje	Top of a mudstone interval, sandy sediments with some clay and conglomerate. An unconformity is identified at the top of the formation.	2720 m	2498 ms
	Åre	Alternating layers of sandstones and claystones interbedded with coal and coaly claystones.	2819 m	2555 ms

Table 2.2: Overview over formations present in the Norne field [1].

Table 2.2 provides an overview over the formations present in the field, a brief description of the rock type in each formation, as well as the depth of each formation top, both in meters and traveltime.

Figure 2.2 below describes the lithostratigraphy in the Norwegian Sea.

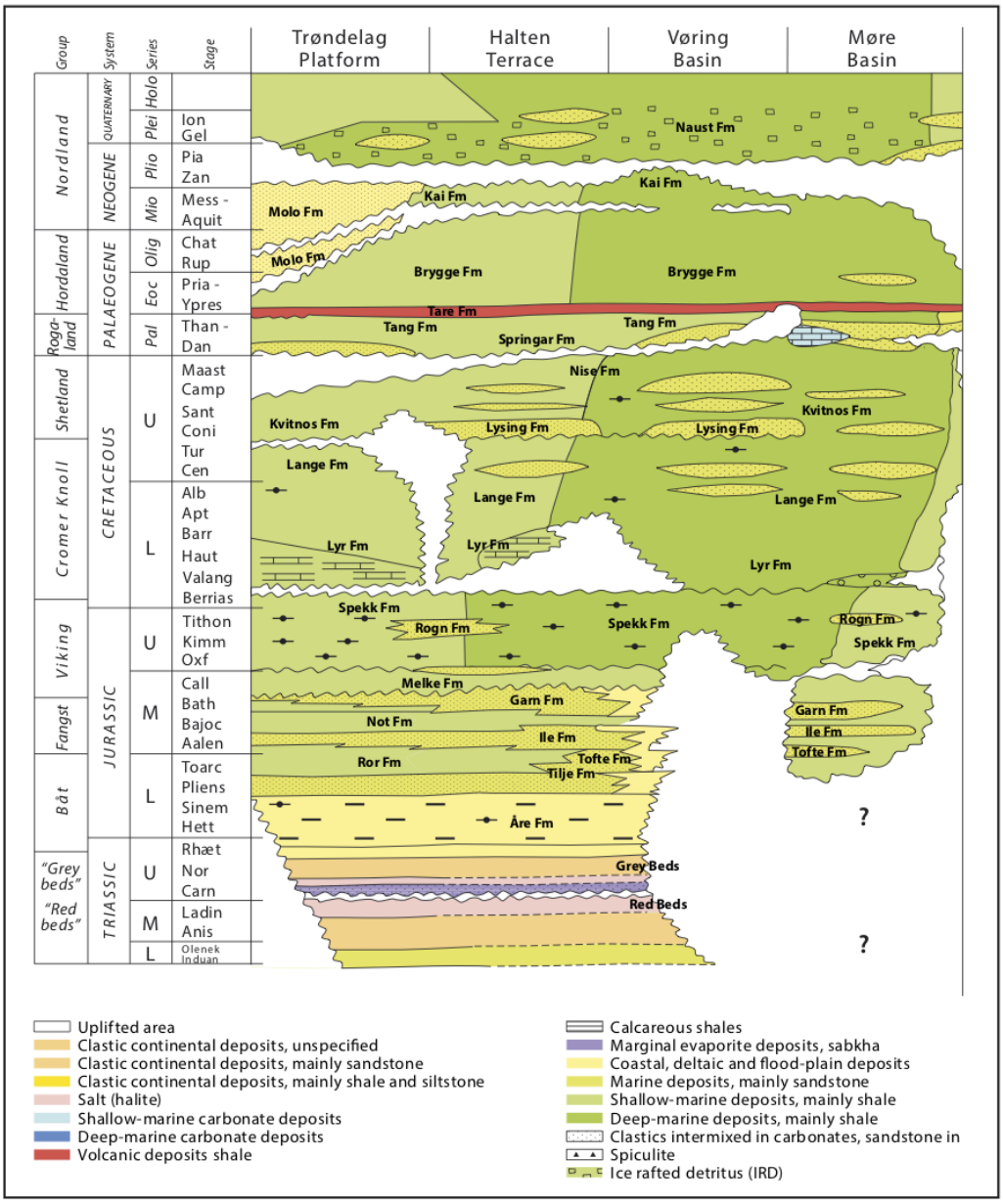

Figure 2.2: Lithostratigraphic chart of the Norwegian Sea [1].

2.1.1 Wells and Production Strategy

The Norne field was discovered by the exploration well 6608/10-2 and confirmed by exploration well 6608/10-3. Exploration well 6608/10-4 found oil in the north-east segment, Segment G, as seen in figure 2.3 below.

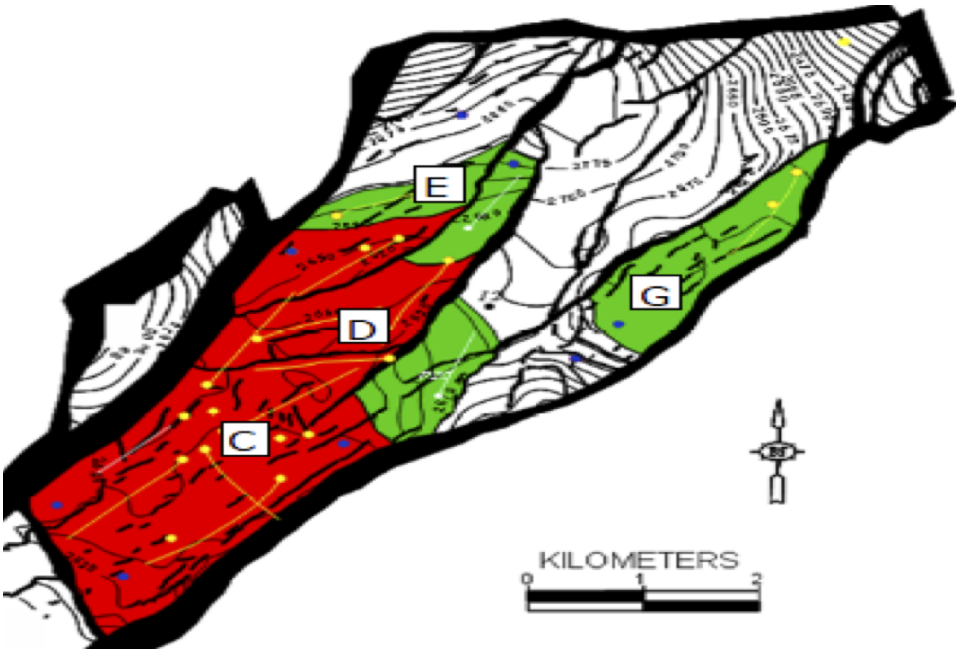

Figure 2.3: Illustration of the shape of the reservoir with the four segments marked. The red area represent the gas cap overlaying the oil, while the green represents oil [2].

The field has been developed with a floating production and storage vessel connected to six subsea wellheads connected to segment B, C, D, E and K. Note that segments B and K, which are located in the North-East Segment, are not a part of this thesis because they are separated from segment C, D, E and G, which are located in the Norne Main Structure.

A total of 58 wells have been drilled in the field to date [1],

- 4 exploration wells
- 37 production wells
- 10 gas and water injection wells
- 7 observation wells

The Norne field has been produced with a combination of pressure depletion,

pressure support from gas and water injection and a combined gas and water injection until 2001. Since 2001, the gas have been produced.

2.1.2 4D Seismic from the Norne field

The first seismic survey carried out across the Norne field was acquired in 1992 as a conventional base survey.

The next survey was shot in 2001, followed up by surveys in 2003, 2004 and 2006. In this thesis, the datasets from 2001 and 2006 have been analyzed in order to detect time-lapse (4D) changes in and around the reservoir, thus the 2001 dataset is the baseline survey while the 2006 dataset is the monitoring survey.

A large seismic survey covering 310 km^2 was shot in 2001, followed by a single source survey covering a smaller area of 45 km^2 over the Norne field itself. This dataset was intended as a time-lapse survey and can be compared with the data set from 1992. The seismic shot in 2003 covered an 85 km^2 large area as identical as possible to the time-lapse survey from 2001. The survey from 2004 was acquired as identically as possible to the 2001 and 2003 surveys, but covered a larger area of 146 km^2. In 2006, the last seismic survey over the Norne field was carried out, as identically as possible to the 2004 survey [22]. The seismic parameters are presented in table 2.3.

Parameter	**Value**			
Survey type	3D			
Filter settings	High cut	200 Hz	Slope	18 dB/oct
	Low cut	3 Hz	Slope	477 dB/oct
Record length Sample rate	6144 ms 2 ms			
Source array	1x5085 ch.in. airgun array, operating at 2000 psi			
Source depth	6 m			
Receiver array	6x3200 m streamer, 240 groups per streamer			
Inline offset	122 m			
Configuration	254 trace 64 fold 6 lines per boat pass 25 m inline spacing			
Polarity convention	Positive pressure at hydrophone recorded as negative number			

Table 2.3: Seismic parameters corresponding to the seismic surveys [8].

These four seismic datasets covering approximately the same area with a couple of years apart make it possible to detect and analyze time-lapse changes in and around the reservoir, and detect how the production changes the rock properties and how the fluid composition in the reservoir changes and the fluid contacts move.

On the seismic dataset from the Norne field, the seabed is represented by a red reflector, as seen by figure 2.4, stating that an increase in acoustic impedance is represented by a trough (red reflector) while a decrease in acoustic impedance is represented by a peak (blue reflector). Due to this information, one can identify the data to be of European Polarity, also known as negative standard polarity.

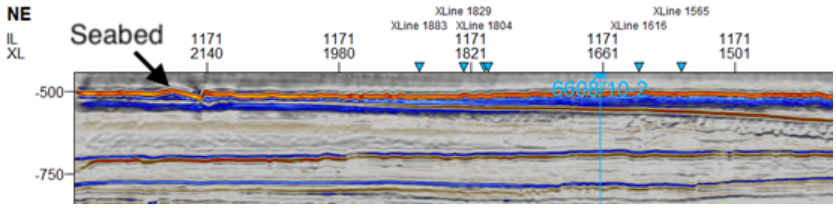

Figure 2.4: Seismic data from the Norne field. The red reflector marked with an arrow represents the seafloor.

2.2 Seismic

Seismic data is generated and acquired by acoustic sources and receivers, on land or in the sea. Processing and interpretation of the acquired data provides an image of the subsurface based on the differences in the seismic properties, such as stiffness and density, between different rock and fluid types.

Different types of sources and receivers can be used, but the most common sources are airguns in water and vibrators on land, while the most common receivers are hydrophones which register pressure waves in water and geophones which register vibrations in the ground on land [23].

On land, the source and receivers are placed on the surface, whilst in the sea two types of seismic can be acquired, traditional marine seismic with towed source and receivers, and seabed seismic, with the receivers placed on the seabed. A traditional marine seismic survey is illustrated by figure 2.5.

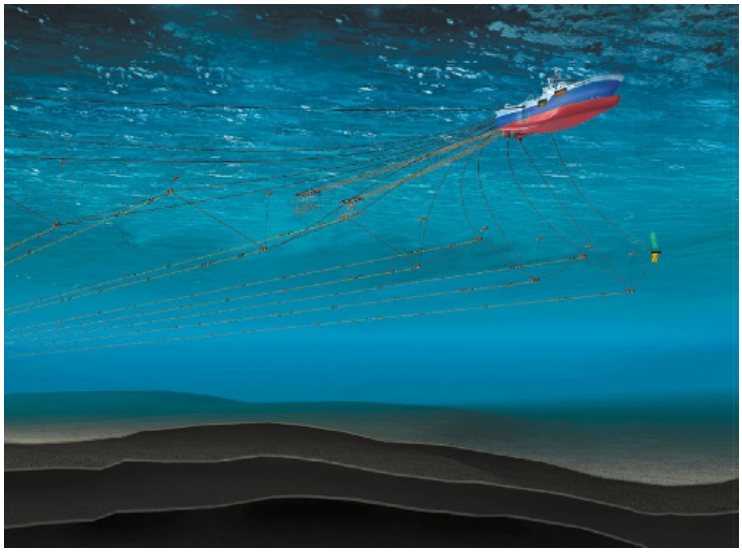

Figure 2.5: Illustration showing a traditional marine seismic survey [3].

In traditional marine seismic, a seismic source, usually an airgun, is fired, resulting in an acoustic wave propagating through the water and down to the sea bed. When the acoustic wave reaches the seabed, a portion of the wave energy is reflected and the rest transmitted at the interface and through the rock. The reflected wave propagates upward, reaching the sea surface where the wave energy is registered by the receivers. The transmitted wave propagates down through the subsurface. When it reaches a new interface, a portion of the seismic energy is reflected and travels back up to the subsurface and water, to the receiver. The remaining acoustic wave travels further down to the next interface where the reflection and transmission repeats it self. See figure 2.6 which illustrates a P-wave with incidence angle θ hitting a plane interface.

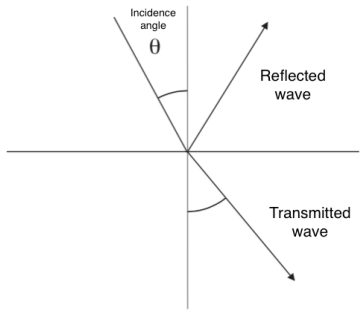

Figure 2.6: Reflected and transmitted wave with incidence angle (θ) smaller than 90° [4].

The magnitude of the reflected wave energy, the reflection coefficient, is given by the following equation,

$$R = \frac{AI_2 - AI_1}{AI_2 + AI_1} = \frac{\rho_2 V_{p,2} - \rho_1 V_{p,1}}{\rho_2 V_{p,2} + \rho_1 V_{p,1}}, \tag{2.1}$$

where AI denotes the Acoustic Impedance, ρ denotes the density, and V_p denotes the P-wave velocity for layers 1 and 2, respectively.

The reflection coefficient is a number ranging between +1 and -1, and is positive when the acoustic impedance increase over the interface. That is, when the underlying medium has higher density and P-wave velocity than the overlying medium. The opposite is the case for when the reflection coefficient is negative, e.g. the underlying medium has lower density and P-wave velocity than the overlying medium.

When an increase in acoustic impedance is represented as a peak while a decrease in acoustic impedance is represented as a trough, the seismic data set has a positive standard polarity, also called American Polarity. The opposite case, when an increase in acoustic impedance is represented as a trough and a decrease in acoustic impedance is represented as a peak, negative standard polarity, is called European Polarity, as seen by figure 2.7 [4].

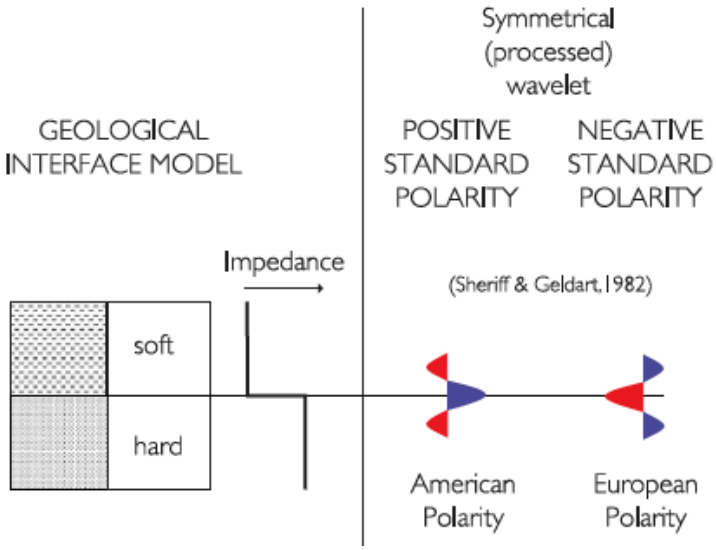

Figure 2.7: Description of the two versions of seismic polarity [4].

On seismic data, a peak is always a blue reflector while a trough is always a red reflector. Thus, it is possible to identify the polarity of the seismic data by looking at the reflector representing the seabed. Because water has lower density and P-wave velocity than any rock type, the acoustic impedance will always increase

over this interface. Thus, if the seabed is a red reflector the seismic data follows European Polarity, while if the seabed is a blue reflector the seismic data follows American Polarity.

There are two types of waves that are relevant in seismic acquisition, pressure waves (P-waves) and shear waves (S-waves). Only P-waves can propagate through water, as fluids cannot have shear forces acting on them. However, when the wave energy is transmitted at the sea bottom, shear waves that propagate through the subsurface are generated. As such, traditional marine seismic will only record P-waves, and only ocean bottom surveys with receivers on the seabed in contact with the subsurface will be able to record S-waves.

There are five different types of seismic surveys, and all surveys have different purposes. These are [3, 4]

- Wellbore seismic - a sesimic survey performed in a well bore, and which can be anything from basic vertical seismic profiles (VSP) with one source and one receiver to more advanced 2D and 3D surveys. A VSP survey records one way travel times and provide important depth and velocity parameters to link seismic with downhole log and well data
- 2D seismic - In marine 2D acquisitions, the survey is acquired with one streamer with receivers and one acoustic source
- 3D seismic - Marine 3D seismic is recorded with a vessel towing a number of streamers with receivers, often more than 10, and with one or more acoustic sources. Marine 3D surveys can also be acquired with more than one vessel to improve azimuth and offset coverage
- 4D seismic - 4D seismic is applied to monitor changes in the fluid composition of oil and gas reservoirs as well as changes to rock parameters, as further described in this report
- 4C seismic - 4C seismic introduces a fourth component in the data set, S-waves, which can significantly improve the understanding of the subsurface, for instance in cases with complicated subsurface parameters caused by for instance gas leakage from reservoirs (gas chimneys)

2.2.1 4D Seismic

4D seismic, often called repeated seismic, where the fourth dimension refers to time, is a seismic survey repeated several times over the same geographical area with identical acquisition parameters, in order to detect changes in the overburden and the reservoir during production [12].

Repeated seismic is commonly used in the following areas [24, 25]:

- monitoring changes in a reservoir under production whereby monitoring movement of fluid contacts as well as identifying trapped gas or oil in segments

of the reservoir
- monitoring storage of CO_2 in the underground
- monitoring geohazards such as landslides, earthquakes, volcanoes
- monitoring elastic properties, saturation and pore pressure
- detect oil/water contact movements in the different faulted segments
- monitoring of the overburden to detect changes due to compaction and subsidence

As this report focuses on changes in overburden and whether it can be detected by applying 4D seismic, some further details are provided.

As the reservoir compacts during production as a result of depletion, the stress and strain in the overburden changes. The degree of change in the overburden is a function of the reservoir depletion and consequently the compaction, and the stiffness of the rock formations in the overburden. As the reservoir compacts and the strain and stress in the overburden changes, the seismic velocity will change, resulting in time shifts visible on the seismic time-lapse data. The velocity and thickness changes accumulate into time shifts that are detectable in the overburden.

The type of reservoir rock determines the compaction, the magnitude of the timeshift in the overburden and consequently the ability to detect the timeshift, and can best be seen in chalk and high-pressure high-temperature reservoirs where the potential for compaction is significant [12].

Even if the baseline seismic survey is of an old vintage, it can still be used to detect useful and important information in a 4D survey case, and it is indicated from previous 4D seismic studies that the results are robust with respect to noise even though the baseline survey is significantly older than the monitoring survey, [26].

The amplitude data in 4D surveys is important as it will be an indicator for fluid movement and migration in the reservoir rock. During production and as a result of either depletion or water/gas flooding for pressure support, fluid fronts/contacts will migrate through the reservoir rock. As the fluid fronts move through the reservoir, amplitudes will consequently change as a result of changing fluid composition at a given point in the reservoir. This can be visualized from the seismic data with the reflectors determining the fluid contacts moving through the reservoir over time.

To be able to detect changes in the overburden from 4D seismic surveys, traveltime data is important. Traveltime is defined as the time it takes for a seismic wave to propagate from the source, down to an interface and up to the receiver, [12].

$$t = \frac{2z}{v} \tag{2.2}$$

where t denotes the two-way traveltime, z denotes the vertical depth down to

the interface and v denotes the P-wave velocity.

Time shifts (Δt) represent a change in the two-way traveltime between two seismic surveys, and is a result of thickness and velocity changes within a layer in the reservoir or the overburden, and can be generated by thickness and velocity change within a layer,

$$\Delta(\Delta t) = \Delta t_{monitor} - \Delta t_{baseline} \tag{2.3}$$

The baseline survey is the survey performed at timestep zero, while the monitoring survey is the seismic survey performed at the next time step. If the traveltime have increased from the first to the second seismic survey, the timeshift will be positive and if the traveltime have decreased, the timeshift will be negative. Equation (2.3) can also be expressed with opposite signs, and thus the timeshift will be negative if the traveltime increase from baseline to monitoring survey.

The fractional change in traveltime, also known as the relative timeshifts, is an interval property that can be more directly interpreted than the timeshifts. The relative timeshifts in a single layer is equal to the difference between the fractional thickness and P-wave velocity change in that specific layer,

$$\left(\frac{\Delta(\Delta t)}{\Delta t} \approx \frac{\Delta z}{z} - \frac{\Delta(\Delta V_p)}{V_p} \right)_{layer} \tag{2.4}$$

The timeshifts accumulate with depth in the subsurface, and at a specific point is given as the sum of the change in traveltime in all the layers above this point [14].

2.3 Time-lapse timeshifts

Time-lapse timeshifts are differences in two-way traveltime observed in the analysis of time-lapse, also known as 4D, seismic. The timeshifts are a result of physical changes in the reservoir and overburden that impact the wave velocities. Inside the reservoir, pore-fluid properties change as a result of production and this will impact the P-wave velocity of the reservoir rock. In addition, thickness change of the reservoir and overburden, as well as stress-strain redistribution may cause changes in seismic velocities impacting the traveltime and thus induce timeshifts.

Timeshifts induced by pore-fluid changes inside the reservoir will only occur inside the reservoir, and be zero above the top reservoir reflection and constant below the reservoir base reflection. The type of fluid displacement in the reservoir will determine whether timeshift is negative or positive. If oil or gas is displaced by

water, the timeshift in the reservoir will be negative. If oil is displaced by gas, the timeshift will be positive.

The timeshifts that are induced by reservoir compaction will have opposite gradients inside and outside of the reservoir. If a reservoir compacts, the overburden is expected to stretch a small amount, causing the traveltime to decrease through the overburden which will lead to positive timeshifts and a slow-down. Areas of the subsurface that will be exposed to compaction and possibly a stress increase will result in negative timeshifts and a speed-up as a result of the decreased traveltime and increased velocity [27].

In this project, timeshifts between specific horizons in the overburden will be analyzed in order to better understand how the overburden behaves during production, and to investigate whether the various traveltimes in the overburden behave similarly or if the formations react differently during production.

2.4 Seismic Amplitude

The amplitude is the magnitude of a wave from zero crossing, either in positive (peak) or negative (trough) direction [28]. The magnitude of the amplitude is the same as the value of the seismic trace at that specific depth, where the seismic trace is defined as a parameter that represents the contrast of acoustic impedance on a rock boundary, on a geophone [29].

At each interface in the subsurface, a portion of the incident energy is reflected back to the seismic source and receivers. The reflected energy is registered by the receivers as a series of pulses separated by the distance in traveltime between each interface.

The seismic trace is then regarded as a convolution between the series registered by the receivers, namely a reflectivity function, and an input pulse, a zero-phase wavelet, as seen in figure 2.8. Each spike in the reflectivity function has an amplitude that is related to the reflection coefficient of a boundary at the depth corresponding to the traveltime that specific spike occurs at.

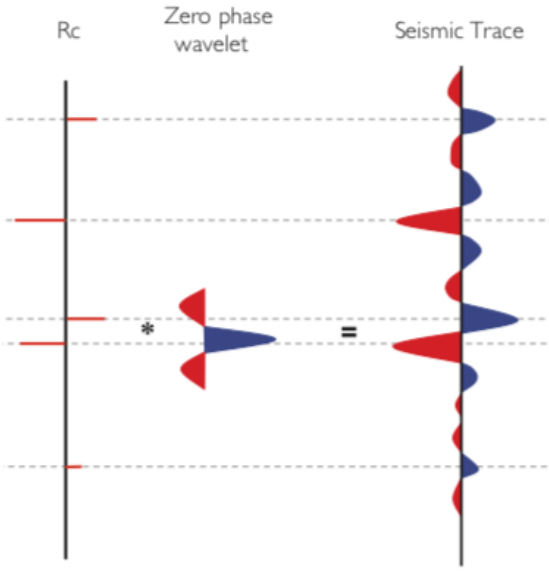

Figure 2.8: Convolution of a reflectivity function and a zero-phase wavelet, resulting in a seismic trace [5].

Many things can affect the seismic amplitude, such as:

- lithology
- porosity
- pore fluid
- fluid saturation
- random noise
- attenuation
- multiple reflections

The amplitude can either be negative or positive, depending on the value of the reflection coefficient in that specific interface. A negative amplitude results from a decrease in the acoustic impedance at the interface due to the underlying medium having a lower density and P-wave velocity than the overlying medium. A positive amplitude results from the opposite of the negative amplitude, an increase in acoustic impedance at the interface due to the underlying medium have higher density and P-wave velocity than the overlying medium. The magnitude of the acoustic impedance also determines the magnitude of the amplitude, if the contrast over an interface is large in magnitude (e.g. large acoustic impedance) causing the amplitude to be large in magnitude as well. The same is the case with weak contrasts.

The interpretation of amplitudes is performed in order to understand the changes

in seismic signatures, and can further be used to distinguish between fluid and rock type induced changes. If the aim of the seismic interpretation is to detect hydrocarbons, the interpreter will look for so-called direct hydrocarbon indicators (DHIs), also known as bright spots. Bright-spots are areas with a large change in amplitude due to a large change in acoustic impedance, such as when a gas saturated sand is underlying a shale, and is most common in relatively shallow areas with unconsolidated or partially consolidates sand or shale. The bright spots are less common in deep areas because the compressibility of the fluid will have little impact on the rock compressibility at deep depths due to the increasing formation pressure with depth [4].

2.5 Amplitude versus Offset Analysis

Amplitude versus offset analysis is a type of analysis where the variation in the reflection coefficient of a seismic wave, in particular the P-wave, is studied for varying offset. In this process, seismic properties and analysis of seismic data are used to determine rock properties such as density, porosity, lithology, as well as to detect hydrocarbons.

2.5.1 The Zoeppritz Equation

The Zoeppritz equations describe the partitioning of seismic wave energy at an interface between two different rock types, as described by figure 2.9. The equations presents an elastic and isotropic behaviour of an incident P-wave on a plane interface with varying angle below the critical angle for that specific wave, to reflected and transmitted P- and S-waves, as given by equation (2.5) [6].

$$\begin{bmatrix} R_p \\ R_S \\ T_p \\ T_s \end{bmatrix} = \begin{bmatrix} -sin\phi_1 & -cos\phi_1 & sin\theta_2 & cos\phi_2 \\ cos\theta_1 & -sin\phi_1 & cos\theta_2 & -sin\phi_2 \\ sin2\theta_1 & \frac{V_{p1}}{V_{p2}}cos2\phi_1 & \frac{\rho_2 V_{s2}^2 V_{p1}}{\rho_1 V_{s1}^2 V_{p2}}cos2\phi_1 & \frac{\rho_2 V_{s2} V_{p1}}{\rho_1 V_{s1}^2} \\ -cos2\phi_1 & \frac{V_{s1}}{V_{p1}}sin2\phi_1 & \frac{\rho_2 V_{p2}}{\rho_1 V_{p1}}cos2\phi_2 & \frac{\rho_2 V_{s2}}{\rho_1 V_{p1}}sin2\phi_2 \end{bmatrix}^{-1} \begin{bmatrix} sin\theta_1 \\ sin\theta_1 \\ sin2\theta_1 \\ sin2\phi_1 \end{bmatrix} \tag{2.5}$$

where R_p denotes the P-wave reflection coefficient, R_s denotes the S-wave reflection coefficient, T_p denotes the transmitted P-wave, T_s denotes the transmitted S-wave, θ_1 denotes the angle of incidence, θ_2 denotes the angle of transmitted P-wave, ϕ_1 denotes the angle of the reflected S-wave and ϕ_2 denotes the angle of the transmitted S-wave.

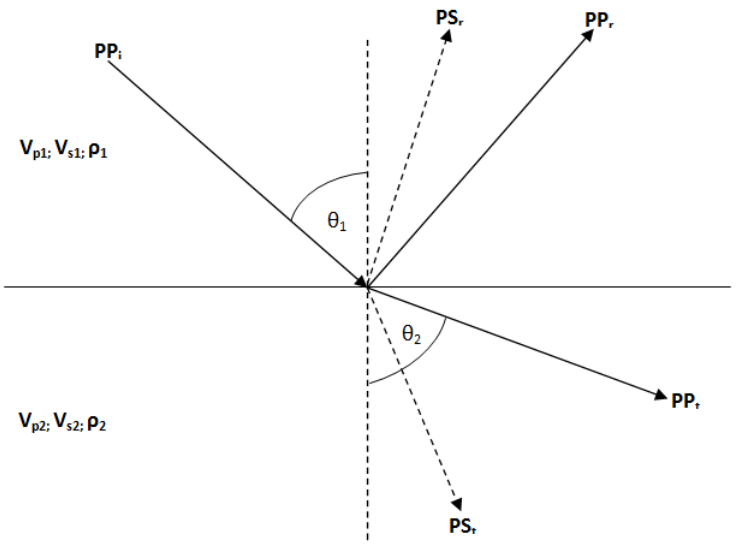

Figure 2.9: Reflection of a P-wave on a plane interface [6].

Due to the complexity of the Zoeppritz equations, several approximation have been derived which also provide a good understanding of how the reflected amplitude vary with density and velocity. A common approximation was derived by Aki and Richards in 1980 and gives the incidence angle dependent reflection coefficient, given by equation (2.6), [4].

$$R_{pp}(\theta) = \frac{1}{2}\left(\frac{\Delta\rho}{\bar{\rho}} + \frac{\Delta V_p}{\bar{V}_p}\right) + \left(\frac{1}{2}\frac{\Delta V_p}{\bar{V}_p} - 2\left(\frac{\bar{V}_s}{\bar{V}_p}\right)^2\left(2\frac{\Delta V_s}{\bar{V}_s} + \frac{\Delta\rho}{\bar{\rho}}\right)\right)sin^2\theta + \frac{1}{2}\frac{\Delta V_p}{\bar{V}_p}sin^2\theta tan^2\theta \tag{2.6}$$

where ρ denotes the density, V_p denotes the P-wave velocity, V_s denotes the S-wave velocity and θ denotes the incidence angle.

Aki and Richard's equation have later been rewritten by Smith and Gidlow into the following equation [30]:

$$R_{pp}(\theta) = \frac{1}{2}\left(\frac{\Delta V_p}{\bar{V}_p} + \frac{\Delta\rho}{\bar{\rho}}\right) - 2\left(\frac{\bar{V}_s}{\bar{V}_p}\right)^2\left(2\frac{\Delta V_s}{\bar{V}_s} + \frac{\Delta\rho}{\bar{\rho}}\right)sin^2\theta + \frac{1}{2}\frac{\Delta V_p}{\bar{V}_p}tan^2\theta \tag{2.7}$$

which can be further simplified to

$$R_{pp}(\theta) = A + Bsin^2\theta + Ctan^2\theta \tag{2.8}$$

where A is the normal-incidence reflection coefficient (e.g. the reflection coefficient when θ is zero) [4], called the intercept, B is the gradient, C is the curvature of the function, defined as:

$$A = \frac{1}{2}\left(\frac{\Delta V_p}{V_p} + \frac{\Delta\rho}{\rho}\right) \tag{2.9}$$

$$B = 2\left(\frac{\bar{V_s}}{\bar{V_p}}\right)^2\left(2\frac{\Delta V_s}{\bar{V_s}} + \frac{\Delta\rho}{\bar{\rho}}\right) \tag{2.10}$$

$$C = \frac{1}{2}\frac{\Delta V_p}{V_p} \tag{2.11}$$

At a specific angle, namely the critical angle, the amplitude of the transmitted P-wave decreases to zero and refracted waves are generated, and the reflection coefficient, R, is equal to 1 at this angle. The critical angle in cases where wave velocity increases with depth, is given by equation (2.12).

$$\theta_c = sin^{-1}\left(\frac{V_{p1}}{V_{p2}}\right) \tag{2.12}$$

A Isotropic and Elastic Media

As previously mentioned, the Zoeppritz equations present an elastic and isotropic behaviour of a P-wave on a plane interface.

An isotropic media is a media with equal properties in all directions, and an isotropic model is useful in cases with simple geology. To understand whether a rock mass is isotropic, is important in order to determine which rock physics tools are available in regards to the seismic modelling [5].

An elastic media is a media that will strain when a force is applied to it, but will return to its original shape when the force is removed, thus it will not change shape.

2.5.2 4D Reflectivity Changes due to Pressure Changes

When hydrocarbons are produced from a reservoir, both the pressure and fluid saturation may change. In this thesis, change in fluid saturation is disregarded and only the pressure change is taken into account.

The reflectivity of the baseline survey ($R_{pp,b}(\theta)$) is equal to Smith and Gidlow's approximation of the Zoeppritz equations (2.7), while the reflectivity of the monitoring survey ($R_{pp,m}$) is defined as follows.

$$R_{pp,m}(\theta) = \frac{1}{2}\left(\frac{\Delta\rho'}{\bar{\rho'}} + \frac{\Delta V_p'}{\bar{V_p'}}\right) - 2\left(\frac{\bar{V_s'}}{\bar{V_p'}}\right)^2\left(\frac{\Delta\rho'}{\bar{\rho'}} + \frac{2\Delta V_s'}{\bar{V_s'}}\right)sin^2\theta + \frac{\Delta V_p'}{2\bar{V_p'}}tan^2\theta \quad (2.13)$$

The fractional change in P-wave velocity for the baseline survey is defined as

$$\left(\frac{\Delta V_p}{\bar{V_p}}\right)_b = \frac{V_{p,2} - V_{p,1}}{\frac{V_{p,2}+V_{p,1}}{2}} \quad (2.14)$$

while the fractional change in P-wave velocity for the monitoring survey is defined as follows

$$\left(\frac{\Delta V_p'}{\bar{V_p'}}\right)_m = \frac{(V_{p,2} + \Delta V_p^P) - V_{p,1}}{\frac{(V_{p,2}+\Delta V_p^P+V_{p,1})}{2}} \quad (2.15)$$

where ΔV_p^P denotes the pressure related velocity change, while $V_{p,1}$ denotes the baseline velocity and $V_{p,2}$ denotes the monitoring velocity.

The change in velocity from the baseline to the monitoring survey is defined as

$$\Delta V_p' = V_{p,2}' - V_{p,1} = (V_{p,2} + \Delta V_p^P) - V_{p,1} = \Delta V_p + \Delta V_p^P \quad (2.16)$$

while the fractional change in P-wave velocity from baseline to monitoring survey is defined as

$$\bar{V_p'} = \frac{(V_{p,2} + \Delta V_p^P + V_{p,1})}{2} = \bar{V_p}\left(1 + \frac{\Delta V_p^P}{2\bar{V_p}}\right) \quad (2.17)$$

By introducing equation (2.16) and (2.17) into equation (2.18) one gets

$$\left(\frac{\Delta V_p'}{\bar{V_p'}}\right)_m = \frac{\Delta V_p + \Delta V_p^P}{\bar{V_p}\left(1 + \frac{\Delta V_p^P}{2\bar{V_p}}\right)} = \frac{\Delta V_p}{\bar{V_p}\left(1 + \frac{\Delta V_p^P}{2\bar{V_p}}\right)} + \frac{\Delta V_p^P}{\bar{V_p}\left(1 + \frac{\Delta V_p^P}{2\bar{V_p}}\right)} \quad (2.18)$$

Because the pressure related velocity change is so small, $\bar{V_p}\left(1 + \frac{\Delta V_p^P}{2\bar{V_p}}\right) = \bar{V_p} + \frac{1}{2}\Delta V_p^P \approx \bar{V_p}$, making it possible to rewrite equation (2.18) to

$$\left(\frac{\Delta V_p'}{\bar{V_p'}}\right)_m \approx \frac{\Delta V_p}{\bar{V_p}} + \frac{\Delta V_p^P}{\bar{V_p}} \quad (2.19)$$

The same is the case for the fractional change in S-wave velocity, which is defined as

$$\left(\frac{\Delta V_s'}{\bar{V}_s'}\right)_m = \frac{\Delta V_s + \Delta V_s^P}{\bar{V}_s\left(1+\frac{\Delta V_s^P}{2\bar{V}_s}\right)} \approx \frac{\Delta V_s}{\bar{V}_s} + \frac{\Delta V_s^P}{\bar{V}_s} \tag{2.20}$$

The density is assumed to remain constant from the baseline to the monitoring survey, resulting in the following

$$\left(\frac{\Delta \rho'}{\bar{\rho'}}\right)_m = 0 \tag{2.21}$$

The relationship between the monitoring S- and P-wave velocities is

$$\left(\frac{\bar{V}_s'}{\bar{V}_p'}\right)_m = \frac{\bar{V}_s\left(1+\frac{\Delta V_s^P}{2\bar{V}_s}\right)}{\bar{V}_p\left(1+\frac{\Delta V_p^P}{2\bar{V}_p}\right)} \approx \frac{\bar{V}_s}{\bar{V}_p} \tag{2.22}$$

Thus, by introducing equations (2.19)-(2.22) into the equation for the P-wave reflectivity for the monitoring survey (equation (2.13)), one gets

$$\begin{aligned} R_{pp,m}(\theta) \approx \frac{1}{2}\left(\frac{\Delta\rho}{\bar{\rho}} + \frac{\Delta V_p}{\bar{V}_p} + \frac{\Delta V_p^P}{\bar{V}_p}\right) - 2\left(\frac{\bar{V}_s}{\bar{V}_p}\right)^2 \left(\frac{\Delta\rho}{\bar{\rho}} + 2\left[\frac{\Delta V_s}{\bar{V}_s} + \frac{\Delta V_s^P}{\bar{V}_s}\right]\right) sin^2\theta \\ + \frac{1}{2}\left(\frac{\Delta V_p}{\bar{V}_p} + \frac{\Delta V_p^P}{\bar{V}_p}\right) tan^2\theta \end{aligned} \tag{2.23}$$

which can be rewritten to

$$\begin{aligned} R_{pp,m}(\theta) \approx & \frac{1}{2}\left(\frac{\Delta\rho}{\bar{\rho}} + \frac{\Delta V_p}{\bar{V}_p}\right) - 2\left(\frac{\bar{V}_s}{\bar{V}_p}\right)^2 \left(\frac{\Delta\rho}{\bar{\rho}} + \frac{2\Delta V_s}{\bar{V}_s}\right) sin^2\theta + \frac{\Delta V_p}{2\bar{V}_p} tan^2\theta \\ & + \frac{1}{2}\left(\frac{\Delta V_p^P}{\bar{V}_p}\right) - 4\left(\frac{\bar{V}_s}{\bar{V}_p}\right)^2 \left(\frac{\Delta V_s^P}{\bar{V}_s}\right) sin^2\theta + \frac{1}{2}\left(\frac{\Delta V_p^P}{\bar{V}_p}\right) tan^2\theta \end{aligned} \tag{2.24}$$

and further simplified into

$$\begin{aligned} R_{pp,m}(\theta) \approx R_{pp,b}(\theta) + \frac{1}{2}\left(\frac{\Delta V_p^P}{\bar{V}_p}\right) - 4\left(\frac{\bar{V}_s}{\bar{V}_p}\right)^2 \left(\frac{\Delta V_s^P}{\bar{V}_s}\right) sin^2\theta \\ + \frac{1}{2}\left(\frac{\Delta V_p^P}{\bar{V}_p}\right) tan^2\theta \end{aligned} \tag{2.25}$$

For small angles ($\theta < 35°$), $tan^2\theta \approx sin^2\theta$, making it possible to rewrite equation (2.25) into

$$\begin{aligned}\Delta R_{pp}^{P} &= R_{pp,m}(\theta) - R_{pp,b}(\theta) \\ &\approx \frac{1}{2}\left(\frac{\Delta V_p^P}{\bar{V_p}}\right) + \left[\frac{1}{2}\left(\frac{\Delta V_p^P}{\bar{V_p}}\right) - \left(\frac{\bar{V_s}}{\bar{V_p}}\right)^2\left(\frac{\Delta V_s^P}{\bar{V_s}}\right)\right] sin^2\theta\end{aligned} \tag{2.26}$$

to obtain an equation for the zero-offset reflection coefficient ($R_{pp,0}$), where the incidence angle (θ) is equal to zero, eliminating the angle-dependent part of the equation, resulting in the following [30]

$$\Delta R_{pp,0} = \Delta A \approx \frac{1}{2}\frac{\Delta V_p^P}{\bar{V_p}} \tag{2.27}$$

2.5.3 Alternative Version of the Traveltime Function

Since velocity change in the overburden is related to pressure changes in the reservoir from the baseline to the monitoring survey, the traveltime function for a single layer can be written as

$$\left(\frac{\Delta(\Delta t)}{\Delta t}\right)_{layer} = \left(\frac{\Delta z}{z} - \frac{\Delta(\Delta V_p^P)}{\bar{V_p}}\right)_{layer} = \left(\epsilon_{zz} - \frac{\Delta(\Delta V_p^P)}{\bar{V_p}}\right)_{layer} \tag{2.28}$$

where ΔV_p^P denotes the pressure related P-wave velocity change, $\bar{V_p}$ denotes the average P-wave velocity from the baseline survey, $\frac{\Delta t}{t}$ denotes the timeshifts and $\frac{\Delta z}{z}$ denotes the vertical strain.

By rewriting and introducing equation (2.27) into equation (2.28) above, one ends up with the following

$$\left(\frac{\Delta(\Delta t)}{\Delta t}\right)_{layer} = \left(\frac{\Delta z}{z} - 2\overline{\Delta A}\right)_{layer} = \left(\frac{\Delta z}{z} - 2\overline{\Delta A}\right)_{layer} \tag{2.29}$$

In order for the traveltime function to be valid for the entire overburden, the relative timeshifts, vertical strain and normal incidence reflectivity have to be summed throughout the overburden down to the specific depth being analyzed, resulting in

$$\sum\left(\frac{\Delta(\Delta t)}{\Delta t}\right) = \sum\left(\epsilon_{zz} - 2\overline{\Delta A}\right) \tag{2.30}$$

where $\Delta(\Delta t)$ is the timeshift between two specific horizons, Δt is the time thickness of the same interval on the baseline survey, ϵ_{zz} is the vertical strain and $\overline{\Delta A}$ is the average plane wave reflection coefficient between the two specific horizons.

2.6 Intercept Stack

In order to analyze the normal incidence reflectivity of the seismic data, an intercept stack, meaning a stack containing only shots with zero offset, has to be generated. In order to do this, the scaled intercept matrix of the near-, mid- and far-stacked data has to be calculated. This is done by calculating a scaling matrix with a scaling factor corresponding to each stack, based on the angle-interval the stack includes and the corresponding reflection coefficient, as well as a matrix including the unscaled intercept and gradient.

The angle dependent reflectivity can be expressed as

$$R_{pp}(t_0, \theta_p) \approx R(t_0) + Gsin^2(t_0, \theta_p) = \begin{bmatrix} 1 & sin^2(t_0, \theta_p) \end{bmatrix} \begin{bmatrix} R(t_0) \\ G(t_0) \end{bmatrix} \tag{2.31}$$

Where $R(t_0)$ denotes the intercept, G denotes the gradient, θ_p denotes the incidence angle and t_0 denotes the zero-offset time.

In order to calculate the generalized intercept and gradient for each stack, a scaling-matrix, $d(t_{0i}, \bar{\theta})$, is needed, which is defined as

$$d(t_{0i}, \bar{\theta}) = \begin{bmatrix} R_{pp}(t_{0i}, \theta_{p1}) \\ \vdots \\ R_{pp}(t_{0i}, \theta_{pn}) \end{bmatrix} = \begin{bmatrix} 1 & sin^2(t_{0i}, \theta_{p1} \\ & \vdots \\ 1 & sin^2(t_{0i}, \theta_{pn})) \end{bmatrix} \begin{bmatrix} R(t_{0i}) \\ G(t_{0i}) \end{bmatrix} \tag{2.32}$$

Thus, the scaled intercept and gradient stack can be expressed as

$$\begin{bmatrix} \bar{R}(t_{0i}) \\ \bar{G}(t_{0i}) \end{bmatrix} = \left(Z^T Z \right)^{-1} Z^T \begin{bmatrix} d(t_{0i}, \theta_{p1}) \\ \vdots \\ d(t_{0i}, \theta_{pn}) \end{bmatrix} \tag{2.33}$$

Z is a design matrix defined by the near-, mid- and far-stacks and angle range. Each stack has a row with one intercept element and one gradient element. The terms corresponding to each stack are generated as shown below.

The near-stack is defined as the expression below,

$$
\begin{aligned}
N_{stack}(\bar{\theta}) &= \frac{1}{\theta_2 - \theta_1} \int_{\theta_1}^{\theta_2} R_{pp}(\theta) d\theta = \frac{1}{\theta_2 - \theta_1} \int_{\theta_1}^{\theta_2} \Big(R + G sin^2\theta \Big) d\theta \\
&= \frac{1}{\theta_2 - \theta_1} \Big[(R\theta + \frac{G}{4} \Big(2\theta - sin(2\theta) \Big) \Big]_{\theta_1}^{\theta_2}
\end{aligned}
\tag{2.34}
$$

$$
\vdots
$$

$$
= \frac{1}{\theta_2 - \theta_1} \Big[R(\theta_2 - \theta_1) + \frac{G}{4} \Big(\Big(sin(2\theta_2) - 2\theta_2 \Big) - \Big(sin(\theta_1) - 2\theta_1 \Big) \Big) \Big]
$$

$$
N_{stack}(\bar{\theta}) = R - \frac{G}{4(\theta_2 - \theta_1)} \Big[\Big(sin(2\theta_2) - 2\theta_2 \Big) \Big(sin(2\theta_1) - 2\theta_1 \Big) \Big]
$$

The same goes for the mid- and far-stack, which are defined as the equations (2.35) and (2.36) presented below

$$
\begin{aligned}
M_{stack}(\bar{\theta}) &= \frac{1}{\theta_4 - \theta_3} \int_{\theta_3}^{\theta_4} \Big(R + G sin^2\theta \Big) d\theta \\
&= \frac{1}{\theta_4 - \theta_3} \Big[R\theta + \frac{G}{4} \Big(2\theta - sin(2\theta) \Big) \Big]_{\theta_3}^{\theta_4}
\end{aligned}
\tag{2.35}
$$

$$
\begin{aligned}
F_{stack}(\bar{\theta}) &= \frac{1}{\theta_6 - \theta_5} \int_{\theta_5}^{\theta_6} \Big(R + G sin^2\theta \Big) d\theta \\
&= \frac{1}{\theta_6 - \theta_5} \Big[R\theta + \frac{G}{4} \Big(2\theta - sin(2\theta) \Big) \Big]_{\theta_5}^{\theta_6}
\end{aligned}
\tag{2.36}
$$

In this case, where the near-, mid- and far-stacks are included in the generation of the intercept stack, the design-matrix, Z, is a *3-by-2* matrix, while the scaling matrix, d, is a *3-by-1* matrix. Each of the rows in the two matrices correspond to one of the stacks.

2.7 Seismic Well-tie

As seismic is measured in time and well-logs are measured in depth, a relationship between time and depth is needed in order to link the formation tops identified in the well to the seismic data.

To create this relationship, a well-to-seismic tie is performed. This process is done by tying a synthetic seismogram to the seismic dataset. The synthetic seismogram is a one-dimensional model of the seismic generated from acoustic and density logs as well as a wavelet that is either extracted from the data or generated synthetic.

Some of the purposes of a seismic well-tie are listed below [4]:

- check if the seismic data is zero phase
- relating stratigraphic markers in the well to loops on the seismic (section)
- wavelet extraction for seismic inversion

After the well-tie is performed it is possible to identify the reflectors representing each formation top on the seismic.

2.8 Geomechanics

2.8.1 Subsidence and Compaction

When hydrocarbons are produced from a reservoir the pressure generally decreases as a result of the fluid extraction. The pressure depletion leads to a compaction of the reservoir rock which turns in to a subsidence at the seafloor. The degree of compaction, and thus the degree of subsidence is closely connected to the rock type in both the overburden and the reservoir, as the mechanical properties determine the stiffness and thus how easily the rock compacts or stretches.

In order for the subsidence to be visible at the seafloor it needs to be of considerable degree, and at least one of the following conditions must be fulfilled [9]:

- significant reservoir pressure decrease
- a highly compressible reservoir rock, such as unconsolidated sand or chalk
- the reservoir must be thick enough so that the compaction is noticeable, as it is often only a few percent of the total reservoir thickness

When a reservoir compacts the subsidence will not appear immediately, but it will propagate through the overburden rock mass lying above the compacted reservoir and become visible at the seabed after time. The time it takes for the subsidence to appear depends on several mechanisms, such as mechanical properties and geology.

According to Røste et al (2015) [12], compaction is easier observed in chalk fields and high-pressure, high-temperature fields, such as the Valhall and Ekofisk fields in the Norwegian North Sea, than in sandstone and normal pressure and temperature

fields, because the time shifts are smaller for the latter reservoir types. Chalk is also a softer rock type than sandstone, which makes it more sensitive to change in mechanical properties.

If the reservoir compaction is larger than the seabed subsidence, the overburden rock will stretch as much as the difference between the compaction and subsidence, thus the total thickness change of the overburden (Δz_{total}) rock mass is the product of the sea floor subsidence (S) minus the reservoir compaction (C) [9];

$$\Delta z_{total} = -(C - S) \tag{2.37}$$

As stated by Bathija et al (2006) [31], the thickness change is defined as positive for elongation and negative for compaction.

2.8.2 Stress Arching

As described by Mulders (2003) [32], pressure depletion in a reservoir leads to changes in both total and effective stress in the surrounding rock.

The change in total stress relative to the pore pressure is called arching, and can be expressed by an arching coefficient, γ,

$$\gamma_v = \Delta\sigma_v / \Delta P_p \tag{2.38}$$

$$\gamma_h = \Delta\sigma_h / \Delta P_p \tag{2.39}$$

where ΔP_p denotes the change in reservoir pressure due to production, and $\Delta\sigma$ denotes the change in total stress, which is defined as

$$\Delta\sigma = \sigma'_{afterproduction} - \sigma'_{beforeproduction} \tag{2.40}$$

Thus, γ express the total stress change per unit depletion at certain locations in the overburden, in either the horizontal (h) or vertical (v) direction.

For reservoirs where the lateral extension is larger than the thickness, the horizontal arching (γ_h) will be larger than the vertical arching (γ_v).

Stress arch forms as a result of pressure change in the overburden during production, and the deformation characteristics are different in the reservoir, the overburden and the sideburden [33], and is likely to form when the reservoir is small and soft in comparison with the surrounding rock [32].

A Overburden Pressure

The hydrostatic pressure, defined as the normal pressure for a given depth, i.e. the stress, is given by

$$P_d = P_o - P_p \tag{2.41}$$

where P_d denotes the overburden pressure, also known as the lithostatic pressure, i.e. the vertical stress, defined as the pressure induced on a rock by the weight of the overlying rock mass, and is given as $P_o = \rho g z$, where ρ_b, g and z denotes the bulk density of the rock, the gravitational force and the vertical depth, respectively. P_p denotes the formation pore pressure, defined as the pressure induced by the pore fluid in the reservoir rock.

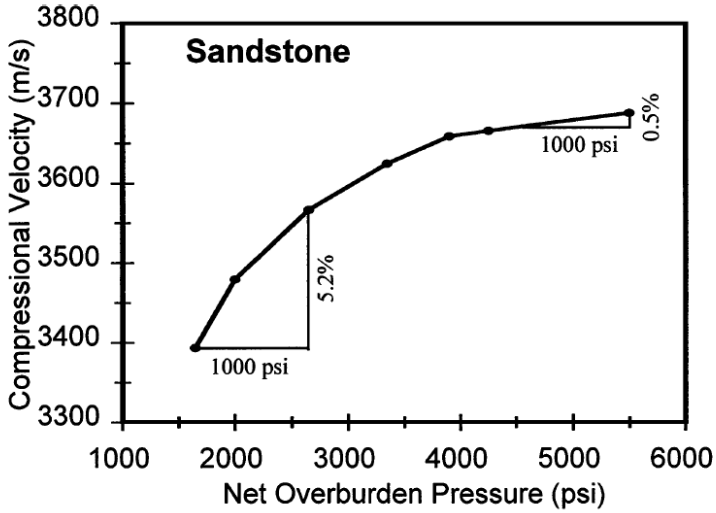

Figure 2.10: Plot of Compressional Velocity (V_p) versus Net Overburden Pressure in a sandstone [7].

The seismic properties are influenced by the hydrostatic pressure, because the formation pore pressure supports a part of the overburden pressure.

Both the hydrostatic and lithostatic pressures are depth dependent, and the seismic velocities will increase as the hydrostatic pressure increases. However, this relationship is nonlinear, meaning that the seismic properties increase faster in regions with low net overburden pressure and shallow depths [7].

2.8.3 Sandstone

The degree of reservoir compaction is highly related to the reservoir rock type and the elastic properties of the rock. Chalk reservoirs are expected to compact more than a sandstone reservoir due to the way chalk react to changes in stress and strain.

In sandstone reservoirs with normal temperature and pressure, the overburden timeshifts are typically very small and thus difficult to interpret. This is due to the stiffness of the rock causing a low degree of compaction when the reservoir pressure deplete as a result of production [12].

Mann and Fatt [34] investigated the effect of pore fluid on the elastic properties of sandstones, and found that the compressibility of a sandstone increases with increasing pore pressure, causing the compressibility of a water saturated sandstone to be greater than for an oil saturated sandstone, which again is greater than for a gas saturated sandstone. They also found that Young's modulus of a saturated sandstone is less than for a dry sandstone, while Poisson's ratio is approximately the same for both wet and dry sandstones. They also stated that the elastic moduli of sandstones with high clay content will be severely affected by water.

The P-wave velocity of a sandstone is ranging between 1500-2000 m/s, and a water saturated sandstone has higher velocity than an oil saturated sandstone which again has higher velocity of gas saturated sandstone.

Because the effective pressure in the subsurface increase with depth, the same is the case for the P-wave velocity as seen in figure 2.10.

Chapter 3

Methodology

The following chapter present the methodology followed in order to obtain the results presented in Chapter 4.

The analysis performed is using two different methods which both are presented in section 3.3.

The seismic interpretation, traveltime extraction and intercept change summation have been performed using Petrel, a software that combines several petroleum related disciplines together, such as geology, geophysics and reservoir engineering, and is provided by Schlumberger. The computation of timeshifts as well as the analysis of timeshifts, relative timeshifts, relative velocity change and computation of vertical strain is done in Matlab, a numerical computing environment.

The order of the thesis follows the following flowchart.

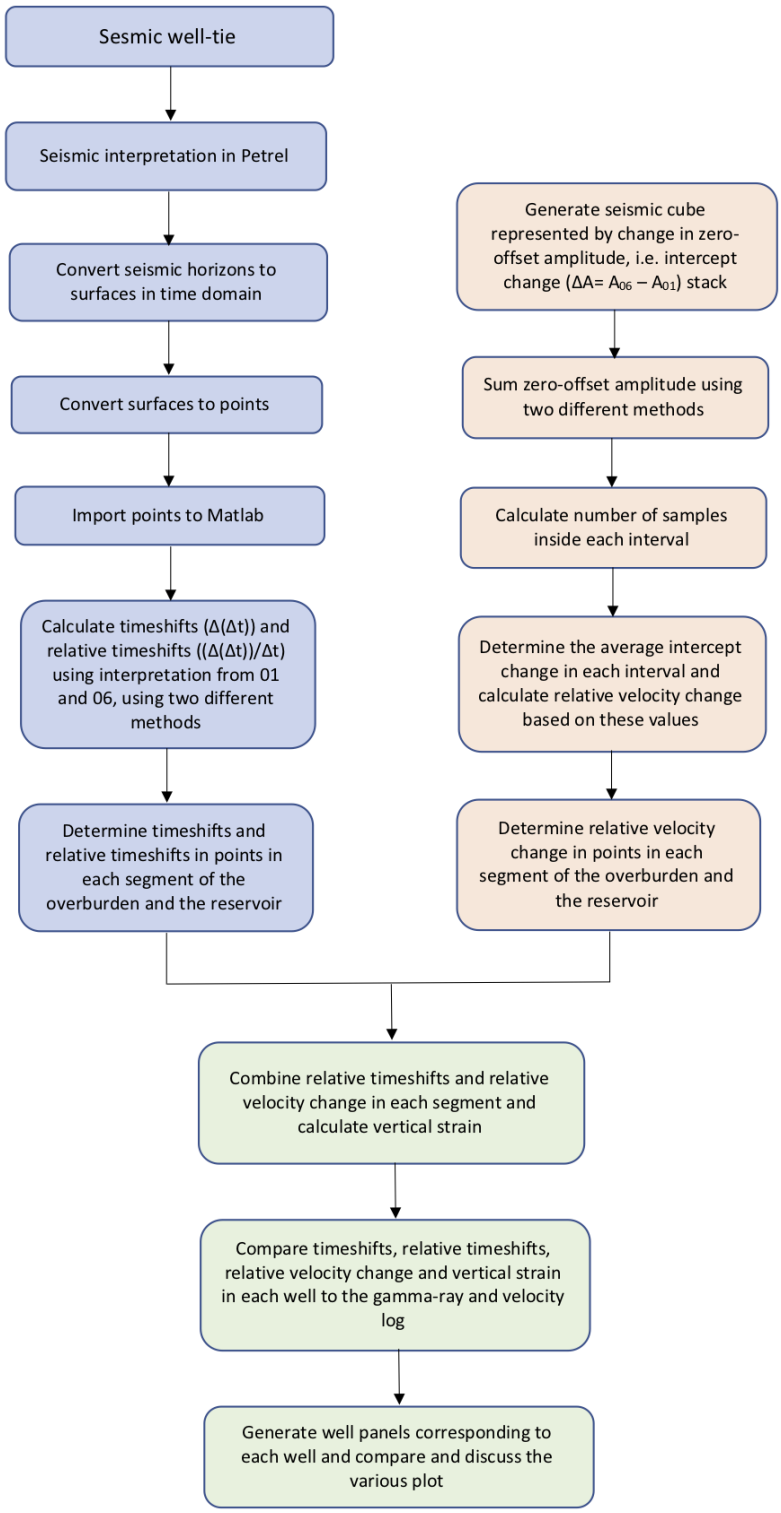

Figure 3.1: Flowchart showing the order of the thesis.

3.1 Seismic Well-Tie

The steps followed in the well-tie process are presented in the workflow below.

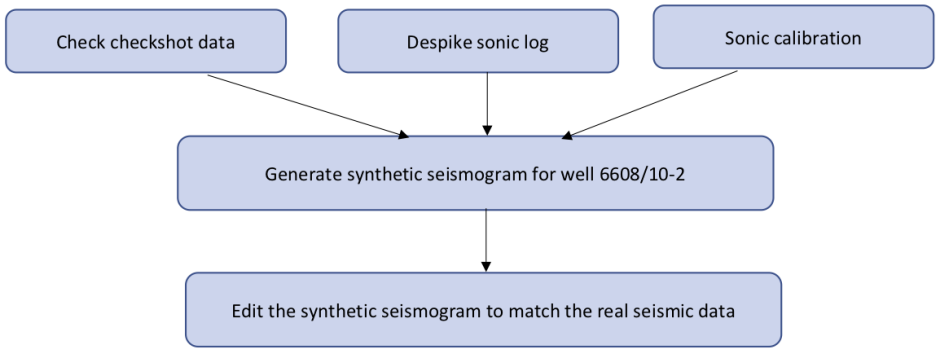

Figure 3.2: Workflow showing the order of the processes performed to complete a seismic well-tie.

The seismic well-tie was performed in order to create a relationship between the 3D seismic cube and the well logs from exploration well 6608/10-2.

First, the sonic log, a log that measure a formation's capacity to transmit seismic waves, is despiked in order to eliminate variations in the log that are equipment induced artifacts. When performing the despiking, the sonic, gamma ray and lithology logs are displayed together. If a spike on the sonic log can be verified by a spike on gamma ray or change in lithology, it is kept. If the spike cannot be verified by the two other logs, it is removed.

Second, the checkshot data from the well is controlled. If the data looks good without any obvious outliers, it is used as is. If obvious outliers are visible, these are removed.

Third, the sonic log calibration is performed with the despiked sonic log and checkshot data as inputs. The sonic log calibration is then calibrated with the checkshot data as a reference, creating a relationship between time and depth, time-depth relationship (TDR).

At last, the synthetic seismogran is generated with the TDR, a wavelet (either extracted from the data or generated synthetic) and the 3D seismic data cube as inputs. One can then display the seismic data together with the synthetic seismogram. By also displaying the formation tops, one can edit the synthetic seismogram so that it matches the real seismic, see figure 3.3 below. The formation tops from the well on the synthetic seismogram align with the same reflectors on

the real seismic.

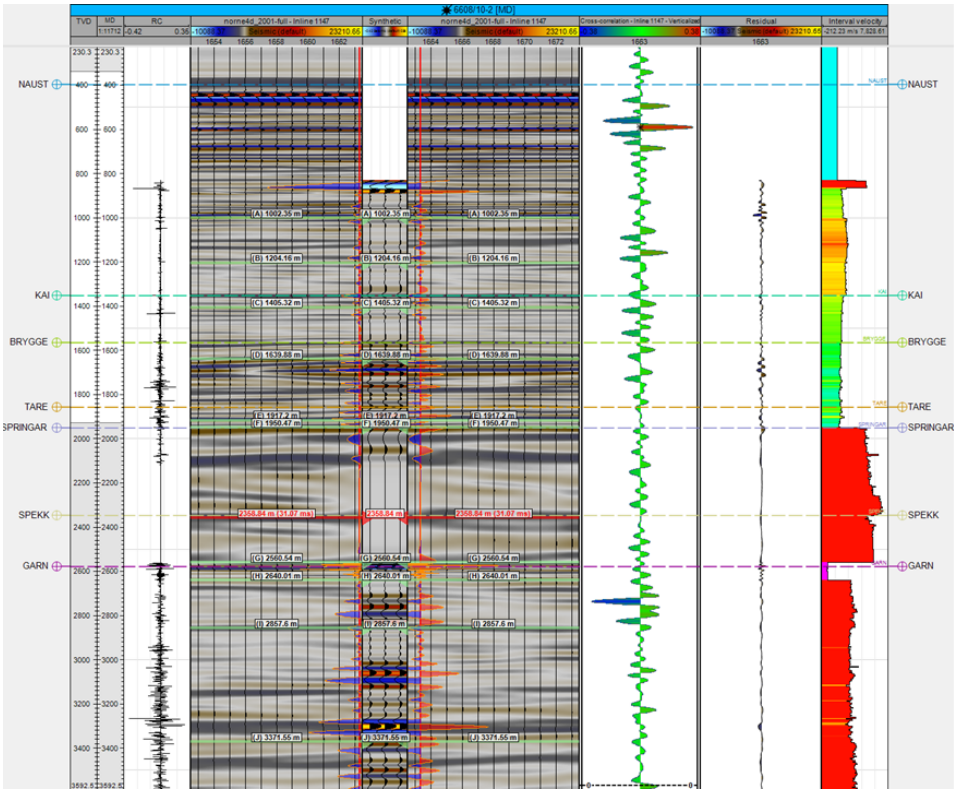

Figure 3.3: The seismic well-tie for well 6608/10-2 performed in this project. Horizontal lines represents the interpreted formation tops from the well.

In well 6608/10-2 there is an inconsistency in the well log data between a point in the Springar formation and down to the top of the Garn formation. The sonic and density logs start at around 830 m depth, as such the synthetic seismogram generated does not cover the entire well bore. Thus, the well-tie is not usable to verify each formation top on the seismic data and some of the formation tops are therefore identified by using the bare eye.

When the well-tie is complete, the formation tops are easy to interpret on the seismic, because they are visible along the wellbore and will align with the reflector representing the formation top on the seismic data. In this case, only some of the formation tops will align with the right reflector due to the inconsistency mentioned earlier in this section. This is clearly visible at the seafloor, where the formation top corresponding to the seafloor is located above the reflector representing the seafloor, which is the first strong red reflector, as seen in figure 3.4.

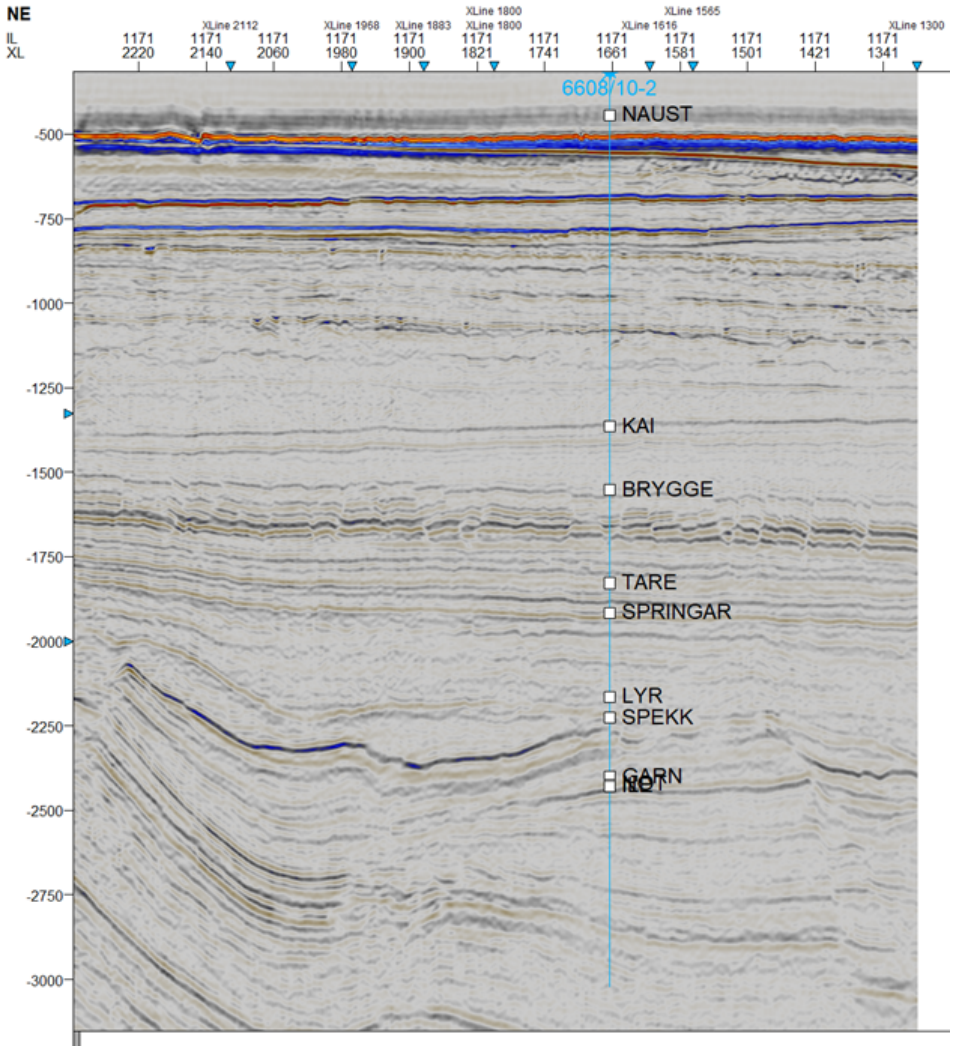

Figure 3.4: An inline from the baseline seismic survey form 2001.

3.2 Seismic Interpretation

After performing the well-tie the following formation tops were identified and interpreted on both the baseline and monitoring seismic data:

- Seafloor / Top Naust

- Top Kai
- Top Brygge
- Top Tare
- Top Springar
- Top Lyr
- Top Spekk
- Top Garn
- Top Not

When performing seismic interpretation, a reflector representing either a peak or trough is interpreted. By interpreting with auto tracking, the computer follows and interprets the path of the strongest amplitude in the chosen reflector.

Because the traveltime of an acoustic wave is registered when acquiring seismic, the depth of the seismic cube is represented in negative time.

Initially, in this project, almost every formation top down to the top of the Not formation were interpreted. Some formations are very thick, such as Naust and Brygge, and other good reflectors inside these formations were therefore interpreted as well, in order to analyze intervals that do not vary too much in thickness.

The formation tops representing the Tare, Tang, Nise and Melke formations are not very good reflectors and were therefore not included in the analysis following the seismic interpretation. In order for the analysis to be as good as possible, the seismic interpretation need to be as accurate as possible to prevent unreliable differences from the 2001 dataset to the 2006 dataset. Thus, by skipping reflectors that were difficult to interpret the analysis following the seismic interpretation will be more reliable. The interpreted horizons used in further analysis are presented in table 3.1 below.

After the interpretation, all seismic horizons were converted to points represented by X, Y and time, making it possible to perform an analysis of the timeshifts from the baseline to the monitoring survey.

Formation	TWT [ms]	TVD [m]
Seafloor / Top Naust	505	374
Intra1 Naust	689	589
Intra2 Naust	780	681
Top Kai	1354	1329
Top Brygge	1541	1542
Intra Brygge	1779	1826
Intra Tare	1860	1917
Top Springar	1906	1928
Top Lyr	2163	2230
Top Spekk	2233	2324
Top Garn	2406	2555
Top Not	2429	2588

Table 3.1: Depth of each interpreted horizon in both seconds and meters, in well 6608/10-2.

3.3 Traveltime Analysis

When analyzing the traveltimes in the formation, both the timeshifts and relative timeshifts were included in the analysis.

The timeshifts are defined as the change in traveltime from the baseline to the monitoring survey in a specific chosen interval

$$\Delta(\Delta t) = \Delta t_{monitoring} - \Delta t_{baseline} = \Delta t_{2006} - \Delta t_{2001} \tag{3.1}$$

while the relative timeshifts are defined as the fractional change in traveltime from the baseline to the monitoring survey,

$$\frac{\Delta(\Delta t)}{\Delta t_{baseline}} = \frac{\Delta t_{monitoring} - \Delta t_{baseline}}{\Delta t_{baseline}} = \frac{\Delta t_{2006} - \Delta t_{2001}}{\Delta t_{2001}} \tag{3.2}$$

The timeshifts and relative timeshifts were calculated using two different approaches where the time intervals were defined differently. The two methods are presented later in sections 3.3.1 and 3.3.2.

3.3.1 Method 1

Method 1 involves calculating the traveltime change from the seafloor and down to the top of each interpreted horizon and calculates the accumulated timeshifts from the seafloor down to a specific point in depth. Thus, by keeping the seafloor

constant the intervals will increase in thickness throughout the analysis as the depth down to each formation top will increase, as illustrated by the equations below.

$$\begin{aligned}\Delta(\Delta t)_{i+1} =& \Delta t_{i+1,mon} - \Delta t_{i+1,base} \\ =& (t_{i+1,2006} - t_{Seafloor,2006}) - (t_{i+1,2001} - t_{Seafloor,2001})\end{aligned} \tag{3.3}$$

$$\begin{aligned}\Delta(\Delta t)_{i+2} =& \Delta t_{i+2,mon} - \Delta t_{i+2,base} \\ =& (t_{i+2,2006} - t_{Seafloor,2006}) - (t_{i+2,2001} - t_{Seafloor,2001})\end{aligned} \tag{3.4}$$

$$\vdots$$

$$\begin{aligned}\Delta(\Delta t)_{N} =& \Delta t_{N,mon} - \Delta t_{N,base} \\ =& (t_{N,2006} - t_{Seafloor,2006}) - (t_{N,2001} - t_{Seafloor,2001})\end{aligned} \tag{3.5}$$

where i = *1, 2,..., N* and $\Delta(\Delta t)_{i+1}$ denotes the timeshift at point *i+1* in depth, Δt_{i+1} denotes the change in traveltime from point i to point *i+1*, both in 2001 and 2006.

By subtracting the traveltime at the seafloor from the traveltime at the point in depth being analyzed, the traveltime from the seafloor and down to the specific point in depth, defined as Δt, is determined, which is why the timeshift is defined as $\Delta(\Delta t)$, as it is the difference in traveltime between the two surveys, from the seafloor and down to the analyzed point.

Figure 3.5 gives a description of the computation of traveltime change using Method 1.

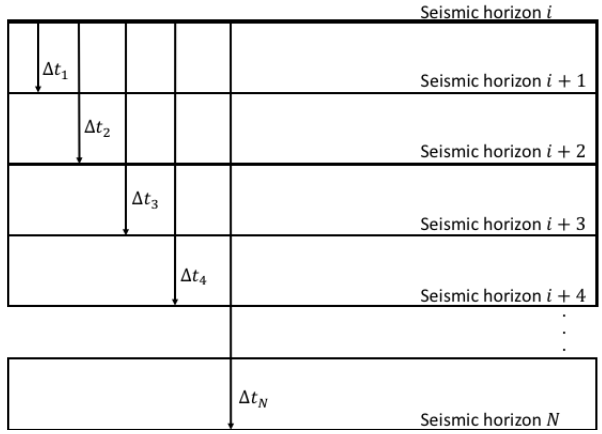

Figure 3.5: Describing the computation of traveltime change using Method 1.

Similarly, the relative timeshifts are calculated as illustrated by the equations below

$$\left(\frac{\Delta(\Delta t)}{\Delta t}\right)_{i+1} = \frac{\Delta t_{i+1,mon} - \Delta t_{i+1,base}}{\Delta t_{i+1,base}} = \frac{(t_{i+1,2006} - t_{Seafloor,2006}) - (t_{i+1,2001} - t_{Seafloor,2001})}{(t_{i+1,2001} - t_{Seafloor,2001})} \tag{3.6}$$

$$\left(\frac{\Delta(\Delta t)}{\Delta t}\right)_{i+2} = \frac{\Delta t_{i+2,mon} - \Delta t_{i+2,base}}{\Delta t_{i+2,base}} = \frac{(t_{i+2,2006} - t_{Seafloor,2006}) - (t_{i+2,2001} - t_{Seafloor,2001})}{(t_{i+2,2001} - t_{Seafloor,2001})} \tag{3.7}$$

$$\vdots$$

$$\left(\frac{\Delta(\Delta t)}{\Delta t}\right)_{N} = \frac{\Delta t_{N,mon} - \Delta t_{N,base}}{\Delta t_{N,base}} = \frac{(t_{N,2006} - t_{Seafloor,2006}) - (t_{N,2001} - t_{Seafloor,2001})}{(t_{N,2001} - t_{Seafloor,2001})} \tag{3.8}$$

where i = *Seafloor, 1, 2,..., N* and $\Delta(\Delta t)_{i+1}$ denotes the timeshift at point *i+1* in depth, Δt_{i+1} denotes the change in traveltime from point i to point *i+1*, both in 2001 and 2006.

3.3.2 Method 2

Method 2 involves calculating the traveltime change in the interval between each interpreted horizon, and calculates the timeshift through the interval defined by the the upper and lower horizons. In cases where the interpreted horizons are formation tops, the calculated traveltime change is the change through that specific horizon, as illustrated by the equation below.

$$\Delta(\Delta t)_{i+1} = \Delta t_{i+1,mon} - \Delta t_{i+1,base} = (t_{i+1,2006} - t_{i,2006}) - (t_{i+1,2001} - t_{i,2001}) \tag{3.9}$$

$$\Delta(\Delta t)_{i+2} = \Delta t_{i+2,mon} - \Delta t_{i+2,base} = (t_{i+2,2006} - t_{i+1,2001}) - (t_{i+2,2001} - t_{i+1,2001}) \tag{3.10}$$

$$\vdots$$

$$\Delta(\Delta t)_{N} = \Delta t_{N,mon} - \Delta t_{N,base} = (t_{N,2006} - t_{N-1,2006}) - (t_{N,2001} - t_{N-1,2001}) \tag{3.11}$$

where *i=1,2,3,..,N* and $\Delta(\Delta t)_{i+1}$ denotes the timeshift at point *i+1* in depth, Δt_{i+1} denotes the change in traveltime from point i to point *i+1*, both in 2001 and 2006.

By always moving the top and bottom horizon downwards when calculating the timeshifts, the timeshifts through that specific interval is calculated.

Figure 3.6 gives a visualization of the computation of traveltime change using Method 2.

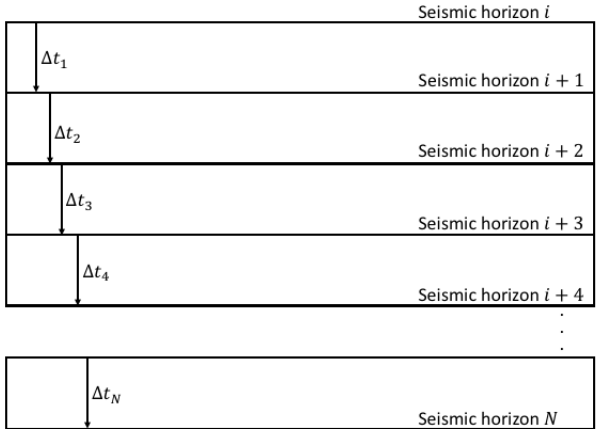

Figure 3.6: Describing computation of traveltime change using Method 2.

Similarly, the relative traveltimes are calculated as illustrated by the following equations

$$\begin{aligned}\left(\frac{\Delta(\Delta t)}{\Delta t}\right)_{i+1} &= \frac{\Delta t_{i+1,mon} - \Delta t_{i+1,base}}{\Delta t_{i+1,base}} \\ &= \frac{(t_{i+1,2006} - t_{i,2006}) - (t_{i+1,2001} - t_{i,2001})}{(t_{i+1,2001} - t_{i,2001})}\end{aligned} \tag{3.12}$$

$$\begin{aligned}\left(\frac{\Delta(\Delta t)}{\Delta t}\right)_{i+2} &= \frac{\Delta t_{i+2,mon} - \Delta t_{i+2,base}}{\Delta t_{i+2,base}} \\ &= \frac{(t_{i+2,2006} - t_{i+1,2001}) - (t_{i+2,2001} - t_{i+1,2001})}{(t_{i+2,2001} - t_{i+1,2001})}\end{aligned} \tag{3.13}$$

$$\vdots$$

$$\begin{aligned}\left(\frac{\Delta(\Delta t)}{\Delta t}\right)_{N} &= \frac{\Delta t_{N,mon} - \Delta t_{N,base}}{\Delta t_{N,base}} \\ &= \frac{(t_{N,2006} - t_{N-1,2006}) - (t_{N,2001} - t_{N-1,2001})}{(t_{N,2001} - t_{N-1,2001})}\end{aligned} \tag{3.14}$$

3.4 Amplitude Analysis

The amplitudes at zero offset have to be analyzed the same way as the timeshifts.

First, the seismic need to be presented in terms of normal-incidence reflection coefficients, i.e. the amplitudes obtained when the source and receiver is located at the exact same position. From that, an intercept stack is generated.

3.4.1 Intercept Stack

The seismic interpretation is performed on full stack data, but near-, mid- and far-stack data is also available. The incidence angle interval corresponding to each dataset is presented in table 3.2 below. These angles make the basis for the intercept stack.

Stack	θ_{min}	θ_{max}	Average θ
Near	$\theta_1 = 0°$	$\theta_2 = 15°$	7.5°
Mid	$\theta_3 = 15°$	$\theta_4 = 30°$	22.5°
Far	$\theta_5 = 30°$	$\theta_6 = 45°$	37.5°

Table 3.2: Incidence angles corresponding to each stack.

By inserting the angles presented in table 3.2 into equations (2.34)-(2.36) presented in section 2.6, one gets the design matrix used when generating the scaled intercept and gradient stacks.

$$Z = \begin{bmatrix} 1 & 0.0225 \\ 1 & 0.1505 \\ 1 & 0.3721 \end{bmatrix} \tag{3.15}$$

The scaling matrix is given as

$$d(t_{0i}, \bar{\theta}) = \begin{bmatrix} 0.07 \\ 0.05 \\ 0.03 \end{bmatrix} \tag{3.16}$$

By combining matrices (3.15) and (3.16) as presented in equation (2.33) in section 2.6, one end up with the following intercept and gradient stack

$$\begin{bmatrix} \bar{R}(t_{0i}) \\ \bar{G}(t_{0i}) \end{bmatrix} = \begin{bmatrix} 0.7957 & 0.4240 & -0.2197 \\ -2.5446 & -0.4991 & 3.0437 \end{bmatrix} \begin{bmatrix} 0.07 \\ 0.05 \\ 0.03 \end{bmatrix} \tag{3.17}$$

$$\begin{bmatrix} \bar{R}(t_{0i}) \\ \bar{G}(t_{0i}) \end{bmatrix} = \begin{bmatrix} 0.0703 \\ -0.1118 \end{bmatrix} \tag{3.18}$$

The seismic cube represented by intercept change will be a lot blurrier than the full stack seismic, as seen by figure 3.7. This is due to the decreased signal-to-noise ratio in the intercept stack, and as only one offset is represented, the seismic will loose a lot of the details that are visible on a seismic section which includes shots with varying offsets. I.e. seismic including different offset ranges will provide different types of data, often with better seismic resolution and lower signal-to-noise ratio.

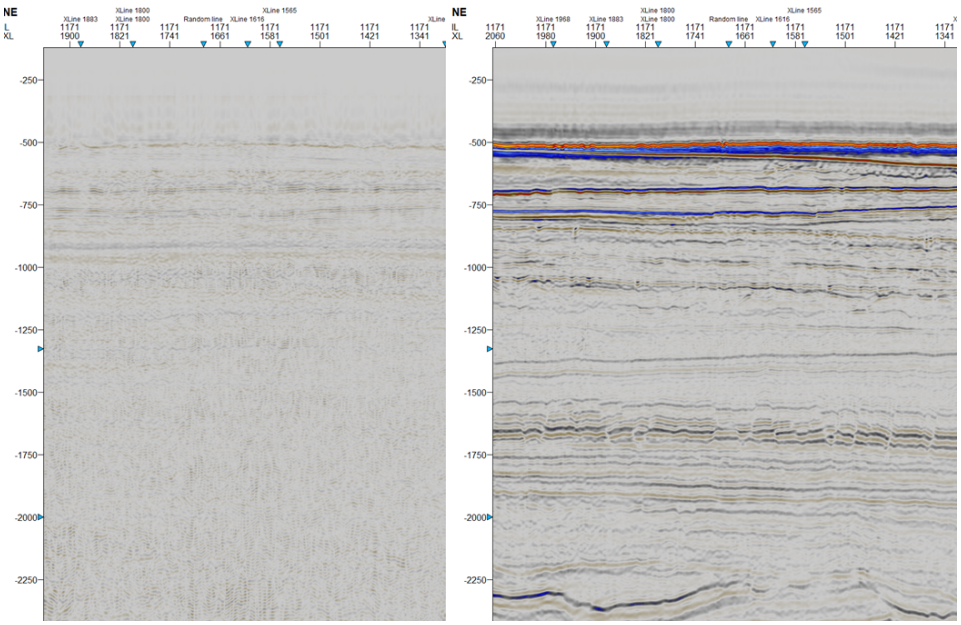

Figure 3.7: The difference between the intercept change (ΔA)-stack and full-stack seismic. ΔA-seismic is shown to left and full-stack seismic to the right.

3.4.2 Intercept Analysis

In order for the intercept to be analyzed, it has to be extracted from the seismic dataset. This is also performed using two different approaches, Method 1 and 2.

First, the seismic cubes corresponding to the baseline (2001) and monitoring (2006) surveys, are converted into intercept cubes as described in section 3.4.1. Then a seismic cube representing the change in intercept (ΔA) from the baseline to the monitoring survey is created, by subtracting the 2001-intercept from the 2006-intercept.

After the change in intercept is calculated at every point in the seismic cube, the sum of the averaged change is extracted from the seismic cube by summing each ΔA-value within the chosen interval multiplied by the number of samples in the same interval, as presented by the general equation below

$$\sum \overline{\Delta A_i} * k \tag{3.19}$$

where k denotes the number of samples within the interval and ΔA_i denotes the intercept change in interval i.

In this thesis, only the averaged intercept change through each interval is needed, which is given as

$$\overline{\Delta A} = \frac{1}{k} \sum \overline{\Delta A_i} * k \tag{3.20}$$

$\Delta\ A$ denotes the intercept change and $\sum \overline{\Delta A_i} * k$ denotes the sum of the averaged intercept change through interval i.

As the sum of the intercept change is being analyzed in this project, the number of samples in each interval have to be calculated. The seismic was sampled with a sampling rate of 4 ms, thus the number of samples is calculated by dividing the time thickness of an interval by the sampling rate, as given by the equation below,

$$k = \frac{\Delta t}{4ms} \tag{3.21}$$

The time thickness of the intervals are different in Method 1 and 2, and the number of samples have to be calculated differently when using the two methods.

When using Method 1, the sample number is defined as

$$k_{M1} = \frac{\Delta t_{Method1}}{4ms} \tag{3.22}$$

and when using Method 2, the sample number is defined as

$$k_{M2} = \frac{\Delta t_{Method2}}{4ms} \tag{3.23}$$

A Amplitude Change - Method 1

When using Method 1, the seafloor will constantly be the reference horizon, which means that no matter what i is equal to, the reference horizon will always be the

seafloor. Thus, the interval will always be summed from the seafloor and down to a horizon that will increase with depth with every iteration.

$$\overline{\Delta A}_i = \frac{1}{k_i}\Big(\sum_{Seafloor}^{i} \overline{\Delta A}_i\Big) \tag{3.24}$$

$$\overline{\Delta A}_{i+1} = \frac{1}{k_{i+1}}\Big(\sum_{Seafloor}^{i+1} \overline{\Delta A}_{i+1}\Big) \tag{3.25}$$

$$\vdots$$

$$\overline{\Delta A}_N = \frac{1}{k_N}\Big(\sum_{Seafloor}^{N} \overline{\Delta A}_N\Big) \tag{3.26}$$

where *i= Seafloor, 1, 2,...,N* .

B Amplitude Change - Method 2

When using Method 2, the reference horizon will always move down one step after each iteration. This means that when *i=1* the reference horizons is the seafloor, while when *i=2* the reference horizon is horizon 1. Thus, the thickness of the interval will always change based on the distance between the analyzed horizons.

$$\overline{\Delta A}_i = \frac{1}{k_i}\Big(\sum_{Seafloor}^{i} \overline{\Delta A}_i\Big) \tag{3.27}$$

$$\overline{\Delta A}_{i+1} = \frac{1}{k_{i+1}}\Big(\sum_{i}^{i+1} \overline{\Delta A}_{i+1}\Big) \tag{3.28}$$

$$\vdots$$

$$\overline{\Delta A}_N = \frac{1}{k_N}\Big(\sum_{N-1}^{N} \overline{\Delta A}_N\Big) \tag{3.29}$$

where *i= Seafloor, 1, 2,.., N.*

3.5 Timeshift and Intercept Analysis in Specific Points

In order to better understand how the timeshifts and amplitude changes varies through the overburden, specific points were analyzed. Because the reservoir is divided into four segments as illustrated by figure 3.8 below, one point inside each segment was chosen. Three of these points were the exploration wells 6608/10-2, 6608/10-3 and 6608/10-4 which are located in Segments C, E and G, respectively. Another arbitrary point was chosen in Segment D.

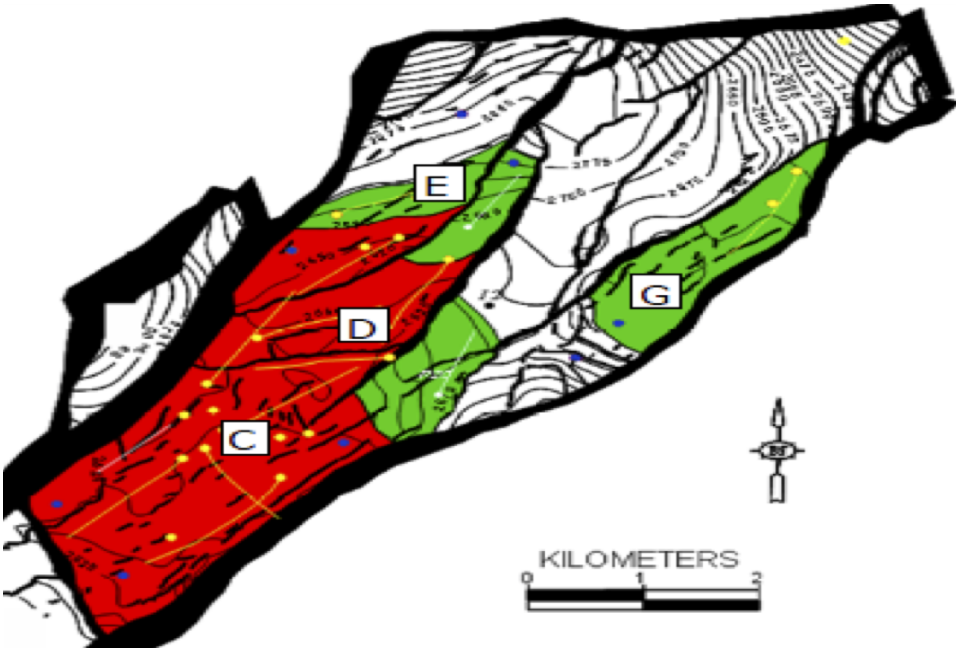

Figure 3.8: Illustration of the shape of the reservoir with the four segments marked. The red area represent the gas cap overlaying the oil while the green represents oil [2].

In these points, the timeshifts and relative timeshifts corresponding to Method 1 and 2 were plotted for each interval between the interpreted horizons. The same was done for the amplitude changes. This provides a good overview over which formations that experience changes in the mentioned parameters from 2001 to 2006, and which do not.

As well-logs are available in all of these exploration wells, the timeshifts, relative timeshifts and intercept change was plotted versus depth in order to compare the

behaviour of these parameters with the behaviour of velocity and gamma-ray log.

3.6 Analysis of Vertical Strain

After both relative timeshifts and intercept change in the overburden have been calculated, these two parameters were inserted into equation (2.30) in order to estimate the vertical strain in the overburden.

Because both the relative timeshifts and the intercept change have been calculated using two different methods, the thickness strain had to be estimated using the results provided by the two methods.

When using Method 1, the vertical strain is estimated by using the following equation,

$$\epsilon_{zz,i} = \Big(\frac{\Delta(\Delta t)}{\Delta t}\Big)_i + 2\overline{\Delta A}_i \tag{3.30}$$

where *i=1,2,.., N* and the equation calculates the total vertical strain down to point i in depth.

When using Method 2, the vertical strain is estimated by using the following equation,

$$\epsilon_{zz,i} = \sum \Big(\frac{\Delta(\Delta t)}{\Delta t} + 2\overline{\Delta A}\Big)_i \tag{3.31}$$

Because Method 2 calculates timeshifts and intercept change in certain intervals, and not the accumulated strain, the values have to be summed in order to result in the total vertical strain from the seafloor down to the specific point in depth, and not only in the analyzed interval.

Chapter 4

Results

4.1 Introduction

The analysis and results in this thesis has been based on the two methods described in Chapter 3.

With Method 1 the accumulated values vs. depth are calculated, and with Method 2 the values for each individual formation are calculated, i.e. the incremental change from one horizon to the next. In any interpretation of geophysical data, there is uncertainty in the interpretation that can impact the final result. Comparing Method 1 to Method 2, it is evident that possible errors in the interpretation will have more impact on Method 2 than Method 1 since in the latter, the values are calculated from the seabed down to the different horizons, whereas in Method 2 the values are calculated from one horizon to the next. As such, Method 1 is considered to be more robust than Method 2, and in this chapter only results from Method 1 is provided, while results from Method 2 are provided in Appendix A.

As described in Chapter 3, the base line seismic (2001 vintage) and the monitoring (2006 vintage) seismic have been interpreted in Petrel, and the calculations in Method 1 and 2 have been performed in a dedicated script generated for this thesis in Matlab.

For preparation purposes, the spread in results for timeshifts and relative velocity change has been challenging to present in figures. In this thesis, the approach has been taken to ensure that also high values are presented in the plots in this chapter and the appendices rather than omitting the higher values.

4.2 Traveltime and Amplitude Analysis at Four Specific Locations

The timeshifts, relative timeshifts and relative velocity changes have been analyzed in four specific locations in the Norne field, one in each segment. The locations in Segments C, E and G are the exploration wells 6608/10-2, 6608/10-3 and 6608/10-4, whilst the location in Segment D was selected based on detection of timeshifts at the location. Figure 4.1 shows the four locations in map view, with timeshifts from the seafloor down to the top of the Not formation. The horst structure and other major faults are marked by red lines.

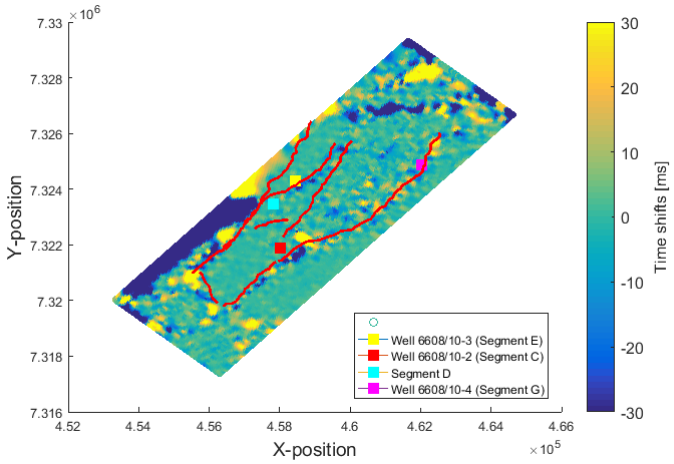

Figure 4.1: Timeshifts from the seafloor down to the top of the Not formation. The four locations that have been analyzed are marked with colored squares and the major faults with red lines.

Figure 4.2 shows the relative velocity change in map view from the seafloor down to the top of the Not formation.

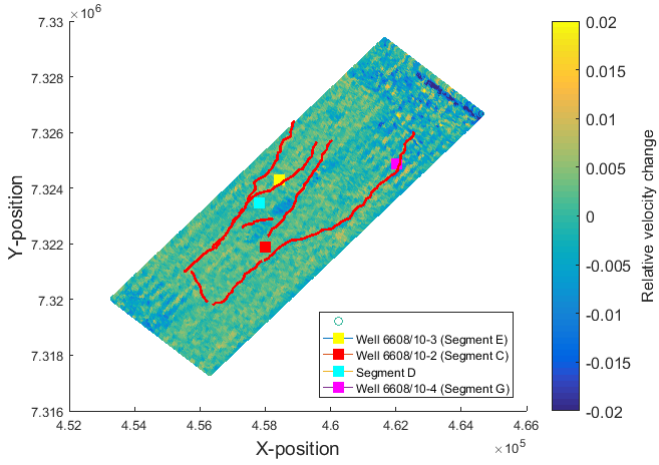

Figure 4.2: Relative velocity change from the seafloor down to the top of the Not formation.

The results from the timeshift, relative timeshifts and relative velocity change calculations applying Method 1 follows.

4.2.1 Well 6608/10-2

Figures 4.3-4.5 shows the results from the calculation of timeshifts, relative timeshifts and relative velocity change through exploration well 6608/10-2 located in Segment C using Method 1.

The calculated accumulated timeshifts from the seabed to the top of the Brygge formation decreases with depth as seen in figure 4.3 indicating an increase in velocity to the top of the Brygge formation. The timeshifts from the top of the Brygge formation down to the top of the Springar formation increases and becomes slightly positive, indicating a velocity slowdown in this part of the overburden.

From the top of the Springar formation down to the top of the Spekk formation, the timeshifts are negative with a significant increase in magnitude from the top Lyr to top Spekk horizons, which again indicates an increase in velocity, in particular in the Lyr formation.

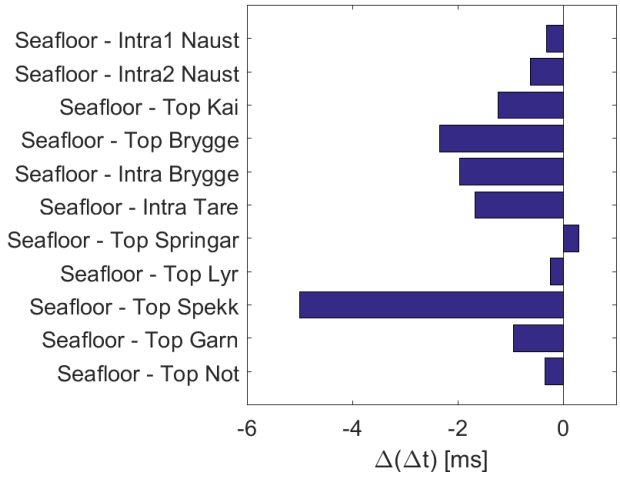

Figure 4.3: Accumulated timeshifts from the seafloor down to each horizon in well 6608/10-2, using Method 1.

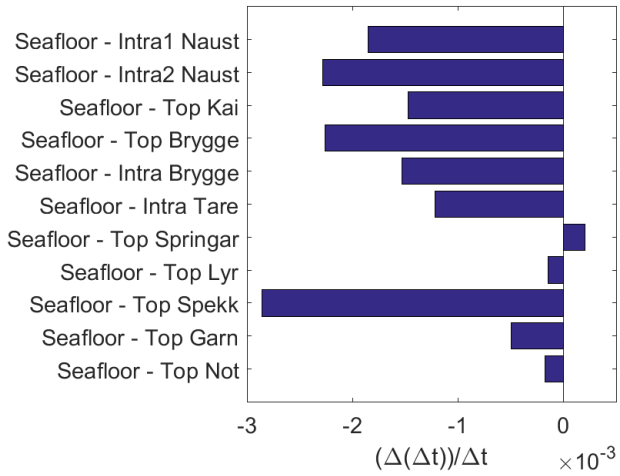

Figure 4.4: Accumulated relative timeshifts from seafloor down to each horizon in well 6608/10-2, using Method 1.

The timeshifts in figure 4.3 and the relative timeshifts in figure 4.4 indicate speed-up and slow-down in the same intervals. The relative timeshift is the fractional change in traveltime from the baseline to the monitoring survey through a specific interval.

The relative timeshift from the seafloor down to the top of the Spekk formation has the largest magnitude of all intervals in well 6608/10-2, indicating that the traveltime change is largest compared to the timethickness of the interval through the Lyr formation.

The relative velocity change calculations as presented figure 4.5 show a positive change down to the top of the Kai formation, with the most significant change in the interval from the seafloor to Intra1 Naust. There is a positive relative velocity change decreasing in magnitude with depth down to the top of the Kai formation.

The relative velocity change from the seafloor down to the top of the Brygge formation is positive and larger in magnitude compared to the previous interval, indicating a speed-up through the Kai formation.

The relative velocity change from the seafloor down to Intra Brygge is negative, indicating a slow-down through the upper part of the Brygge formation. This slow-down is followed by a speed-up from Intra Brygge to Intra Tare.

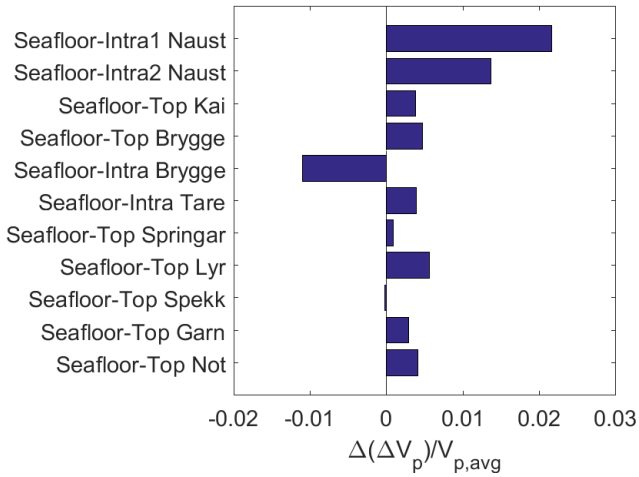

Figure 4.5: Accumulated relative velocity change from the seafloor down to each horizon in well 6608/10-2, using Method 1.

The relative velocity change from the seafloor down to the top of the Springar formation has decreased in magnitude, indicating a slow-down from Intra Tare to the top of the Springar formation. The next interval, from the seafloor down to the top of the Lyr formation have increased in magnitude, indicating a speed-up through the Springar formation, followed by a slow-down through the Lyr formation. The relative velocity change from the seafloor down to the top of the Garn and Not formations are positive and increasing in magnitude, indicating a speed-up that is increasing with depth through the Spekk and Garn formations.

4.2.2 Well 6608/10-3

Figures 4.6-4.8 show the results from the calculations of timeshifts, relative timeshifts and relative velocity change through exploration well 6608/10-3 located in Segment E using Method 1.

In figure 4.6 calculated timeshifts along well 6608/10-3 are presented and it can be observed that the timeshifts along this well are relatively small compared to what has been observed in well 6608/10-2 and varying in magnitude and also ranging between positive and negative values. The only intervals that appear to have timeshifts of any magnitude are Intra Brygge to Intra Tare, Top Lyr to Top Spekk and to Top Garn to Top Not. This is further discussed in Chapter 5.

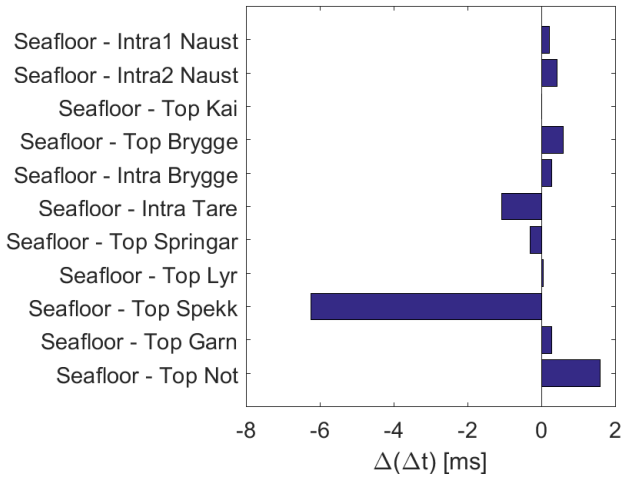

Figure 4.6: Timeshifts from the seafloor down to each horizon in well 6608/10-3, using Method 1.

The timeshifts are positive and increasing in magnitude from the seafloor and down to Intra1 Naust and Intra2 Naust, respectively, which indicates a slow-down through the upper parts of the Naust formation. The timeshift from the seafloor down to the top of the Kai formation have decreased in magnitude approaching zero, indicating a speed-up through the lower part of the Naust formation. From the seafloor and down to the top of the Brygge formation the timeshift have increased in magnitude, indicating a slow-down through the Kai formation, followed by a speed-up through the upper part of the Brygge formation and down to Intra Tare, indicated by the decreasing magnitude of the timeshifts.

The interval from the seafloor and down to the top of the Springar formation and the top of the Lyr formation, respectively, indicate a slow-down through the the

lower part of the Tare formation, the Tang formation and the Springar formation due to the decreasing magnitude of the timeshift approaching zero in the first interval and the slightly positive timeshift in the second interval. The timeshift through the Lyr formation is strongly negative, indicating a significant speed-up, followed by a significant slow-down through the Spekk and Garn formations.

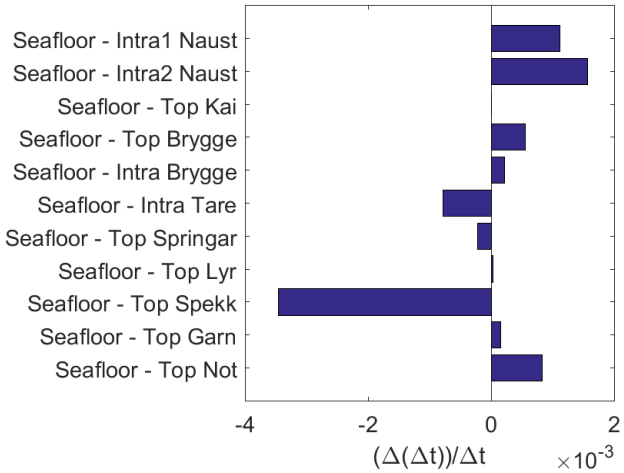

Figure 4.7: Relative timeshifts from the seafloor down to each horizon in well 6608/10-3, using Method 1.

The relative timeshifts, shown in figure 4.7 follow the same trend as the timeshifts, but they vary in magnitude due to the varying thickness of the intervals. The large negative relative timeshift from the seafloor down to the top of the Lyr formation indicates that the timeshift is large compared to the timethickness of the interval, i.e. that the speed-up is significant through the formation. As the magnitude of the relative timeshift in the previous interval is small, it is reasonable to believe that it is the timeshift throught the Lyr formation that lead to the large relative timeshift through that interval.

In figure 4.8 one can see that the velocity change is negative and significant in magnitude through the uppermost part of the Naust formation, indicating that the velocity change through the interval is large compared to the average velocity in the same interval. The relative velocity change through the other intervals have almost the same magnitude, indicating that the formations contribute to the velocity change in equal amount.

The velocity change from the seafloor down to top of the Lyr formation is approximately zero, indicating that the velocity decreases through the Springar formation. Thus, the velocity change is positive indicating a speed-up through the

Lyr and Spekk formations, followed by a slow-down through the Garn formation.

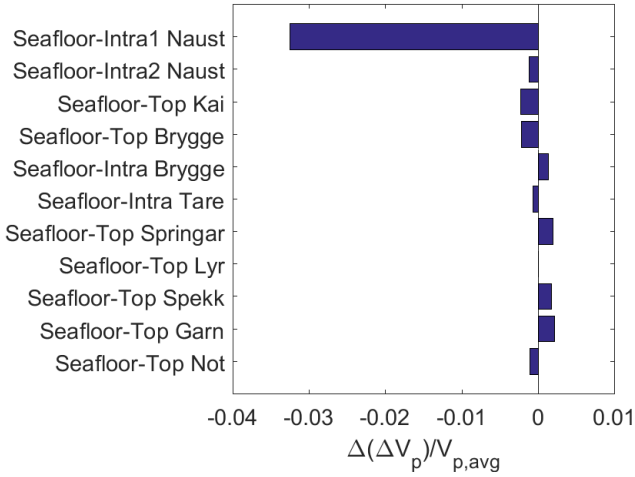

Figure 4.8: Relative velocity change from the seafloor down to each horizon in well 6608/10-3, using Method 1.

4.2.3 Well 6608/10-4

Figures 4.9-4.11 show the results from the calculation of timeshifts, relative timeshifts and relative velocity changes through exploration well 6608/10-4 located in Segment G using Method 1.

The timeshifts are presented in figure 4.9. According to the figure, there is a speed-up in the upper part of Naust formation followed by a slow-down through the rest of the formation which is increasing in magnitude approaching the top of the Kai formation.

Through the Kai formation, the timeshift indicate a speed-up followed by a slow-down through the upper part of the Brygge formation. The timeshift from the seafloor down to Intra Tare is still positive, but because the magnitude of the timeshift has decreased this indicates a slight speed-up from Intra Brygge to Intra Tare.

The timeshift from the seafloor down to the top of the Springar formation is positive and larger in magnitude than the timeshift in the previous interval, indicating a slow-down from the reflector inside the Tare formation and down to the top of the Springar formation.

The timeshift through the Springar formation is negative due to a speed-up,

followed by a slow-down through the Lyr formation. There is a large timeshift from the seafloor down to the top of the Garn formation, indicating a significant speed-up through the Spekk formation, followed by a slow-down through the Garn formation.

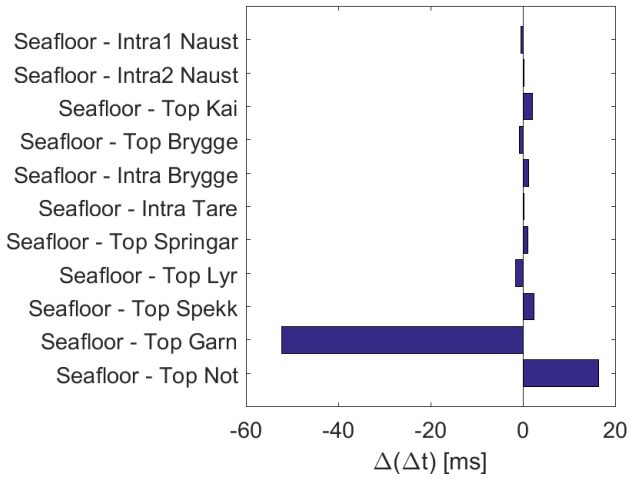

Figure 4.9: Timeshifts from the seafloor down to each horizon in well 6608/10-4, using Method 1.

The relative timeshifts, shown in figure 4.10 follow the same trend as the timeshifts, but vary in magnitude due to the thickness variation of each interval.The relative timeshift from the seafloor down to top of the Garn formation is the timeshift with the largest magnitude through the well, indicating that the timeshift through this interval is large compared to the timethickness of the same interval. Due to the small relative timeshift in the previous interval from the seafloor down to the top of the Spekk formation, it is reasonable to believe that the large shift in relative timeshift us caused by the timeshift through the Spekk formation.

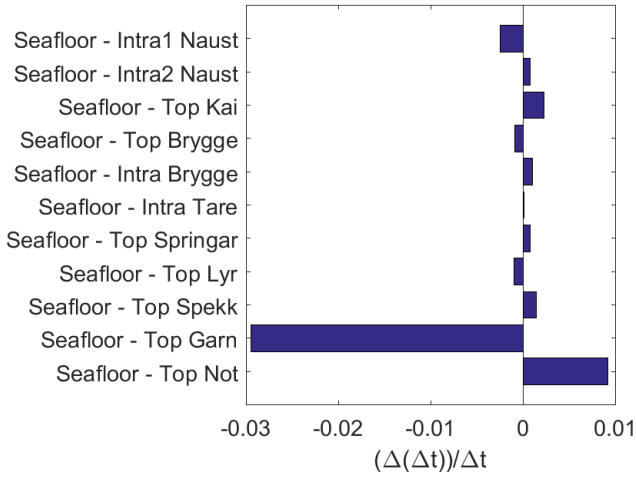

Figure 4.10: Relative timeshifts from the seafloor down to each horizon in well 6608/10-4, using Method 1.

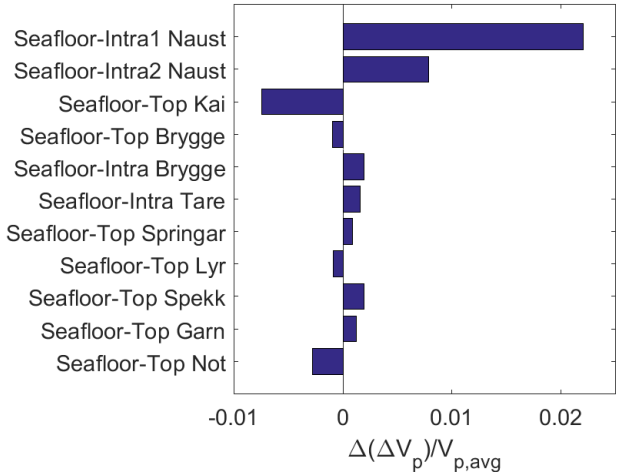

Figure 4.11: Relative velocity change from the seafloor down to each horizon in well 6608/10-4, using Method 1.

The velocity change shown in figure 4.11 indicates that there is a speed-up in the upper part followed by a slow-down in the lower part of the Naust formation.

The relative velocity change from the seafloor down to the top of the Kai formation is negative but smaller in magnitude than for the previous interval,

indicating that the velocity has increased through the Kai formation.

The velocity continue to increase through the upper part of the Brygge formation before it decreases from Intra Brygge down to Intra Tare. The velocity decreases down to top of the Springar formation and continues to decrease through the Springar formation down to top of the Lyr formation.

The velocity again increases through the Lyr formation, before it decrease through the Spekk and Garn formations.

4.2.4 Location in Segment D

Figures 4.12-4.14 shows the results from the calculation of the timeshifts, relative timeshifts and relative velocity change at the selected location in Segment D using Method 1.

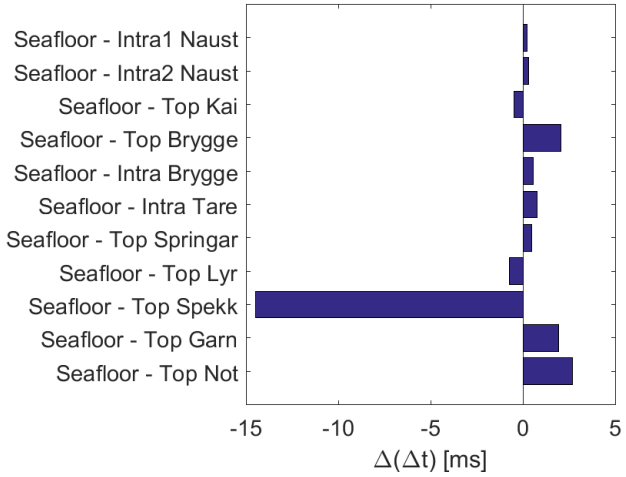

Figure 4.12: Timeshifts from the seafloor down to each horizon along a specific point in Segment D using Method 1.

The timeshifts at shallow depths at the selected location are slightly positive indicating a slow-down through the upper parts of the Naust formation, followed by a speed-up through the lower most part of the Naust formation.

From the seafloor and down to the top of the Brygge formation the timeshift is positive, indicating a slow-down through the Kai formation.

The timeshift through the upper part of the Brygge formation is positive but

smaller in magnitude than the timeshift through the previous interval, indicating that there is a speed-up through this interval. The timeshift through the next interval, from the seafloor down to Intra Tare, is larger in magnitude implying a slow-down.

The timeshift from the seafloor down to top of the Springar formation is smaller in magnitude than the timeshift through the previous interval, indicating a slight speed-up. This speed-up continues and increases in magnitude through the Springar formation and increases to the largets negative magnitude through the Lyr formation.

From the seafloor down to the top of the Garn formation, the timeshift is positive indicating a slow-down which also continues through the Garn formation down to the top of the Not formation.

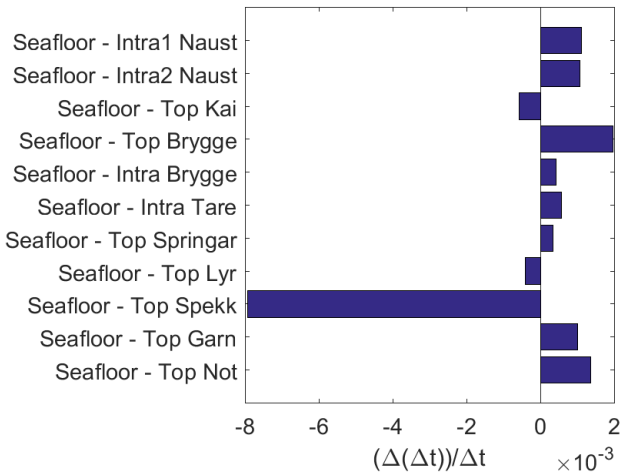

Figure 4.13: Relative timeshifts from the seafloor down to each horizon along a specific point in Segment D, using Method 1.

The relative timeshifts in figure 4.13 show the same trend as the timeshifts in figure 4.12. The relative timeshift from the seafloor down to the top of the Brygge and Spekk formations are larger in magnitude than the other intervals, indicating that the timeshift through these intervals are large compared to the timethickness through the same intervals. Due to the small relative timeshifts in the intervals previously mentioned, it is reasonable to conclude that the timeshifts through the Kai and Lyr formations are significant.

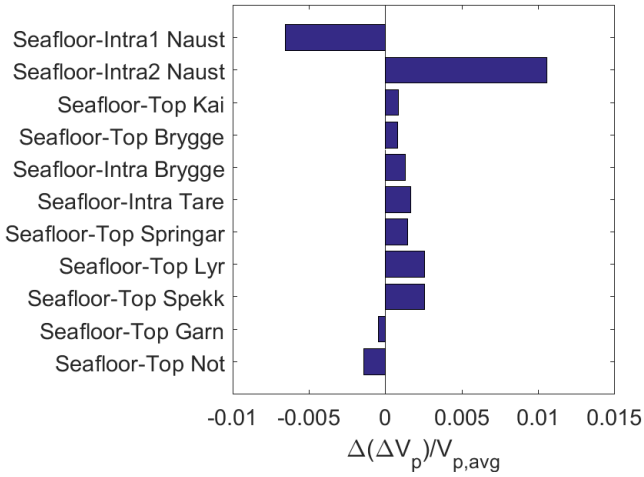

Figure 4.14: Relative velocity change from the seafloor down to each horizon in Segment D, using Method 1.

The relative velocity change in figure 4.14 shows a slow-down from the seafloor down to Intra1 Naust. The relative velocity change from the seafloor down to Intra2 Naust is positive, indicating a speed-up in the middle part of the Naust formation. The velocity change from the seafloor down to the top of the Kai formation is still positive, but as the magnitude of the velocity change is smaller in this interval than the previous, the lower most part of the Naust formation experience a slow-down.

As can be seen in the figure, the relative velocity change is positive in the following four intervals, from the seafloor down to the top of the Kai formation to Intra Tare, as well as increasing in magnitude, indicating a speed-up. This is followed by a slow-down from Intra Tare down to the top of the Springar formation.

In the two following intervals, from the seafloor down to the top of the Lyr and Spekk formations, respectively, the relative velocity change is larger than for the previous interval indicating a speed-up.

From the seafloor down to the top of the Garn formation, i.e. through the Spekk formation, the relative velocity change is negative, indicating a slow-down through the Spekk formation which continue to increase through the Garn formation.

4.3 Map view

The timeshifts, relative timeshifts and relative velocity changes have been analyzed in map views at every interpreted horizon. The six following figures (4.15-4.20) show the aforementioned parameters at the top of the Garn and Not formations, i.e. the last formation top before the reservoir and the first formation top inside the reservoir. These formation tops were chosen because the change on top and inside the reservoir is expected to be opposite of each other. When there is a speed-up in the reservoir due to for instance compaction, the velocity right above the reservoir is expected to slow down.

4.3.1 Timeshift Analysis

As seen in figures B.1-B.7 in Appendix B, which are displaying the timeshifts from the seafloor down to the horizons from Intra1 Naust to Top Lyr respectively, the timeshifts at shallow depths in the formation are very small and thus not visible with the chosen scale. In figure B.8, which show the timeshifts from the seafloor down to the top of the Lyr formation, timeshifts are starting to be visible. The timeshifts are mostly negative (blue) illustrating a speed-up, but some areas with positive timeshifts (yellow) illustrating a slow-down, are also present. In figure B.9 and 4.15, which are showing the timeshifts down to the top of the Spekk and Garn formations, respectively, the timeshifts are more visible than for the shallower horizons, which is reasonable because timeshifts are believed to increase with depth. Positive timeshifts, indicating a slow-down, are visible in Segment E and some places in Segment C, while a mixture of positive and negative timeshifts are visible in the area around Segment D.

Figure 4.16 shows the timeshifts from the seafloor down to top of the Not formation. Not lies below the Garn formation which is the first hydrocarbon bearing formation in the reservoir, as mentioned in section 2.1. Timeshifts are clearly visible, both in the area outside and inside the reservoir, as well as along the faults and inside Segment C and G.

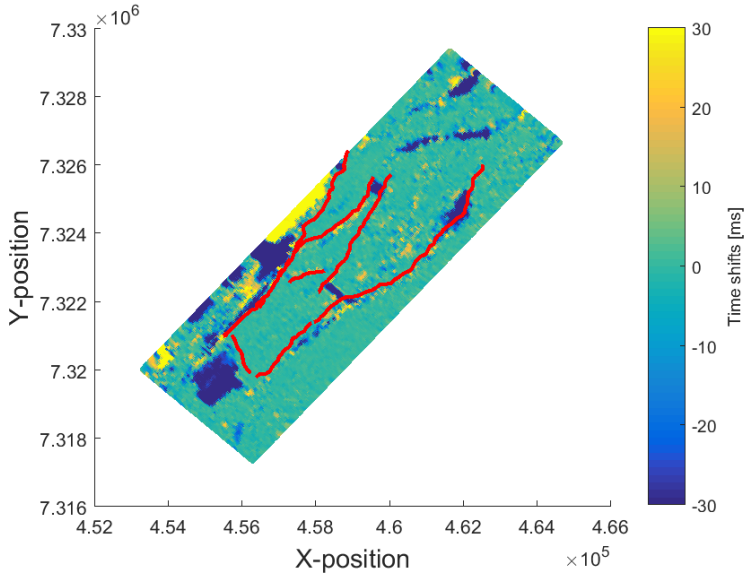

Figure 4.15: Timeshifts from the seafloor down to top of the Garn formation, using Method 1.

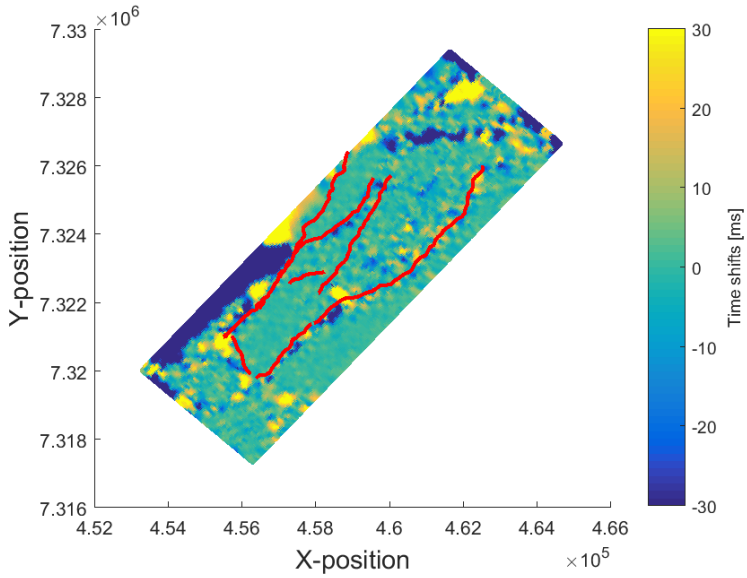

Figure 4.16: Timeshifts from the seafloor down to top of the Not formation, using Method 1.

4.3.2 Relative Timeshift Analysis

The relative timeshifts are presented in figures B.10-B.18 in Appendix B and figures 4.17 and 4.18. The relative timeshifts are mainly very small in the shallow parts of the formation, but at Top Brygge (figure B.13) some relative timeshifts are visible, before they disappear in the following three figures, from Intra Brygge to Top Springar.

In figure B.17, relative timeshifts are visible following the same pattern as the timeshifts in figure B.8. The relative timeshifts increase in magnitude in figure B.18 and 4.17 at the top of the Spekk and Garn formations, respectively. Figure 4.18 shows the relative timeshifts from the seafloor down to the top of the Not formation. Relative timeshifs are clearly visible, especially in Segments D and G as well as along the faults.

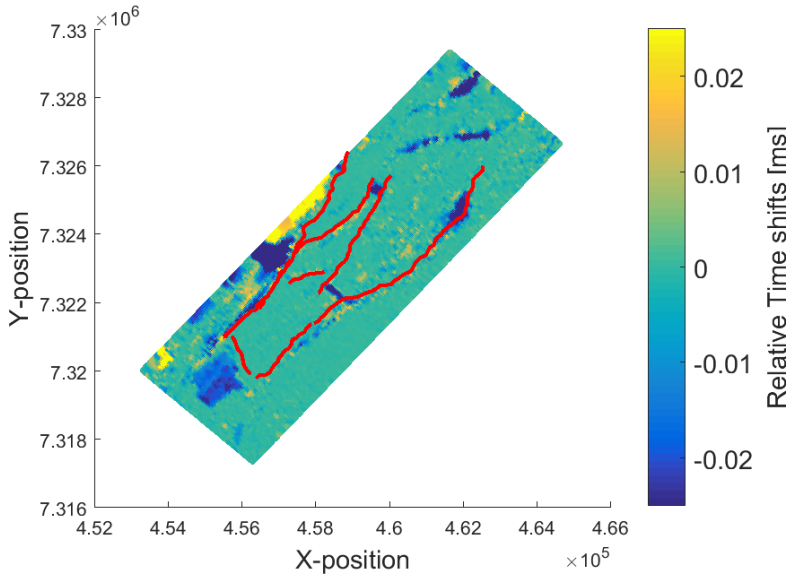

Figure 4.17: Relative timeshifts from the seafloor down to top of the Not formation, using Method 1.

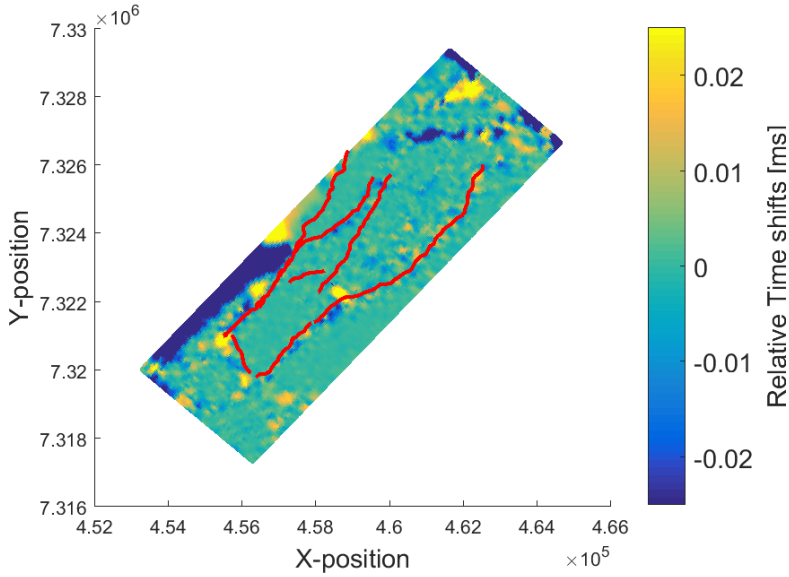

Figure 4.18: Relative timeshifts from the seafloor down to top of the Not formation, using Method 1.

4.3.3 Analysis of Relative Velocity Change

Figures B.19-B.27 in Appendix B and figures 4.19 and 4.20 shows the relative velocity change, $(\frac{\Delta(\Delta V_p)}{V_p} = 2 * \sum \Delta A)$, from the seafloor down to each horizon from Intra1 Naust to the top of the Garn formation. The first two figures, B.19 and B.20, show the amplitude change down to Intra1 Naust and Intra2 Naust, two good reflectors in the Naust formation, respectively. The relative velocity changes at these reflectors are quite large, especially compared to the following plots where the differences in velocity is only slightly visible.

The same is the case for figures 4.19 and 4.20, which show the relative velocity change from the seafloor down to top of the Garn and Not formations, respectively.

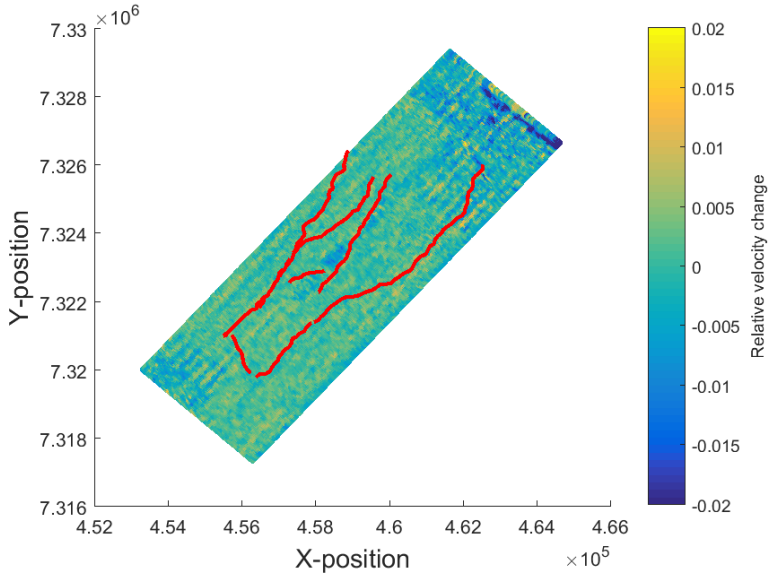

Figure 4.19: Relative velocity changes from the seafloor down to top of the Not formation, using Method 1.

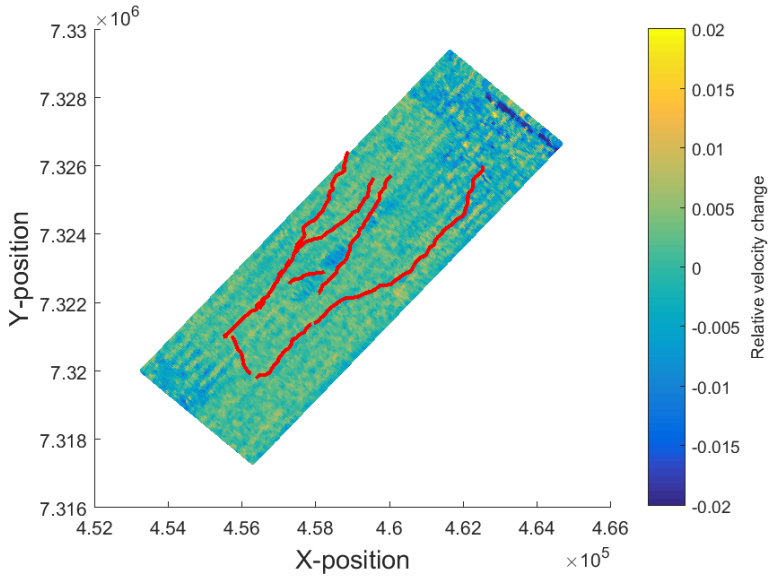

Figure 4.20: Relative velocity changes from the seafloor down to top of the Not formation, using Method 1.

4.4 Well Panels

As previously mentioned, the selected points to be analysed in Segments C, D and G represent the locations of three exploration wells in the Norne field. The gamma-ray log and P-wave velocity logs are available for these three wells, thus the timeshifts, relative timeshifts, relative velocity change and vertical strain have been plotted together with the logs for comparison purposes.

This has not been done for the location in Segment D because there is no time-depth-relationship in this location.

4.4.1 Well 6608/10-2

The velocity log, timeshift-plot, relative timeshfit-plot, relative velocity change-plot and calculated vertical strain-plot have been analyzed in order to investigate whether the speed-ups and slow-downs in the locations coincide, and are listed in table 4.1.

It appears that in none of the intervals, all five parameters can provide a unison conclusion, e.g. in cases where a slow-down has been determined by the velocity log, the timeshift, the relative timeshifts and the relative velocity change, the calculated strain should according to the theory be positive. However, the opposite is determined from the calculations. This problem is discussed further in Chapter 5.

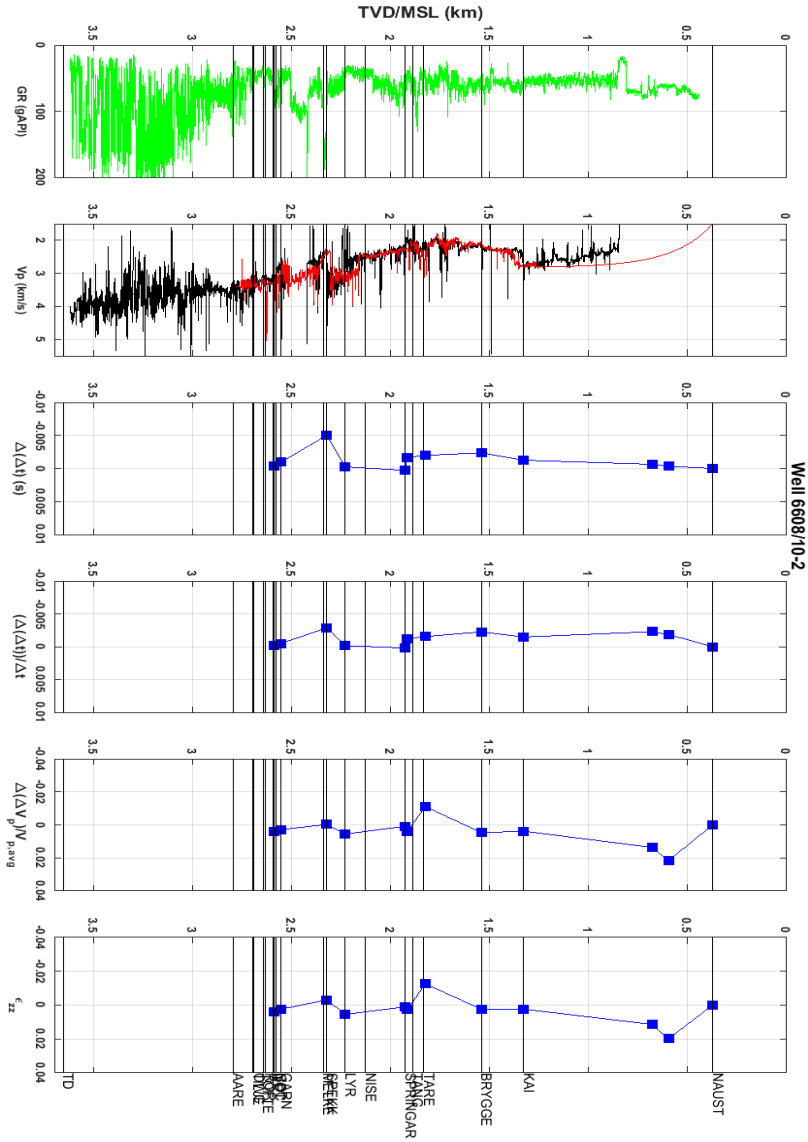

Figure 4.21: Well panel showing gamma-ray log, P-wave velocity log, timeshifts, relative timeshifts, relative velocity change and strain in well 6608/10-2, using Method 1.

Interval	$V_p - log$	$\Delta(\Delta t)$	$\frac{\Delta(\Delta t)}{\Delta t}$	$\frac{\Delta(\Delta V_p)}{V_p}$	ϵ_{zz}
Intra1 Naust	-	Speed-up	Speed-up	Speed-up	Positive
Intra2 Naust	-	Speed-up	Speed-up	Slow-down	Negative
Kai	Speed-up	Speed-up	Slow-down	Slow-down	Negative
Brygge	Slow-down	Speed-up	Speed-up	Speed-up	0
Intra Brygge	Slow-down	Slow-down	Slow-down	Slow-down	Negative
Intra Tare	Slow-down	Slow-down	Slow-down	Speed-up	Positive
Springar	Slow-down	Slow-down	Slow-down	Slow-down	Negative
Lyr	Speed-up	Speed-up	Speed-up	Speed-up	Positive
Spekk	Speed-up	Speed-up	Speed-up	Slow-down	Negative
Garn	Speed-up	Slow-down	Slow-down	Speed-up	Positive
Not	Slow-down	Slow-down	Slow-down	Speed-up	Positive

Table 4.1: The velocity behaviour indicated by the timeshifts, relative timeshifts, relative velocity change and vertical strain in well 6608/10-2, using Method 2.

The trend of the relative timeshift and relative velocity change plots can be further verified by figure 4.22 where the mean of each relative timeshift and relative velocity change interval are plotted together with the actual values for both parameters.

When the mean of the relative timeshift is negative it indicates a speed-up, while when the mean is positive it indicates a slow-down. When the mean of the relative velocity change is positive it indicates a speed-up, while when the mean is negative it indicates a slow-down.

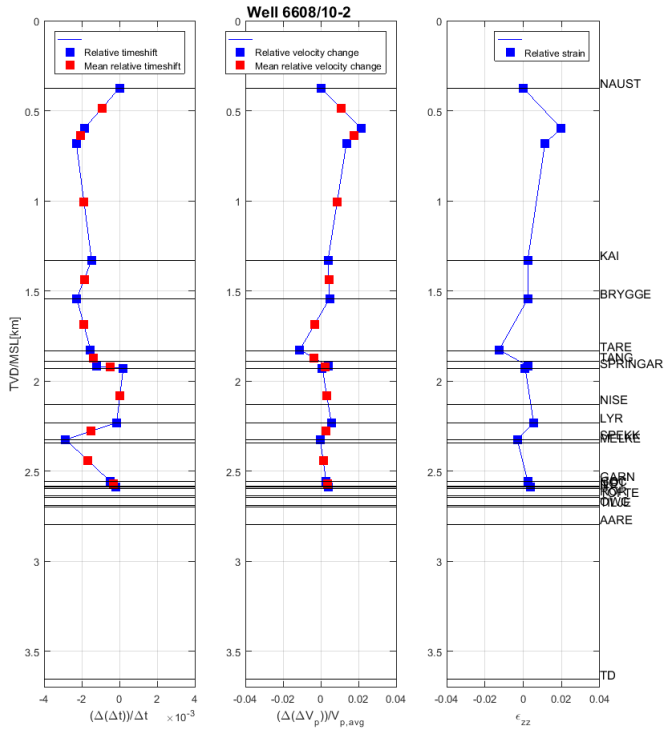

Figure 4.22: Relative timeshifts and relative velocity change plotted together with the mean of the start- and end-point of each interval marked with red squares, vertical strain and R-factor for well 6608/10-2, using Method 1.

Table 4.2 shows the calculated relative timeshifts, relative velocity changes and vertical strain in well 6608/10-2 using both Method 1 and Method 2.

When using Method 1, the magnitude of the calculated strains are realistic in the deeper intervals, i.e. from the seafloor down to the top of the Springar formation and down.

When using Method 2, the magnitude of the calculated strains are realistic in the shallow intervals, down to Intra Brygge. After that the magnitude of the calculated strain becomes unrealistically large.

Interval	**Method 1**			**Method 2**		
	$\frac{\Delta(\Delta t)}{\Delta t}$	$\frac{\Delta(\Delta V_p)}{\bar{V}_p}$	ϵ_{zz}	$\frac{\Delta(\Delta t)}{\Delta t}$	$\frac{\Delta(\Delta V_p)}{\bar{V}_p}$	ϵ_{zz}
Seafloor	0	0	0	0	0	0
Intra1 Naust	-0.185%	2.17%	1.98%	-0.185%	2.17%	1.98%
Intra2 Naust	-0.229%	1.37%	1.14%	- 0.308%	-0.21%	-0.52%
Kai	-0.148%	0.383%	0.236%	-0.108%	-0.091%	-0.2%
Brygge	-0.226%	0.473%	0.246%	-0.565%	0.86%	0.29%
Intra Brygge	-0.154%	-1.11%	-1.26%	0.155%	-0.98%	-0.83%
Intra Tare	-0.122%	0.388%	0.266%	0.35%	3.88%	4.23%
Springar	2.05E-02%	8.32E-02%	0.104%	4.65%	-9.2%	-4.56%
Lyr	-1.5E-02%	0.558%	0.543%	-0.201%	2.55%	2.35%
Spekk	-0.286%	-2.6E-02%	-0.312%	-7.14%	-51.19%	-58.33%
Garn	-5.0E-02%	0.288%	0.238%	2.54%	3.87%	6.41%
Not	-1.8E-02%	0.408%	0.390%	3.54%	13.48%	17.01%

Table 4.2: Comparison of relative timeshifts, relative velocity change and calculated strain using Method 1 and Method 2 in well 6608/10-2.

4.4.2 Well 6608/10-3

Figure 4.23 shows the well panel corresponding to well 6608/10-3 where Method 1 have been used to calculate the timeshifts, relative timeshfits, relative velocity changes and calculated vertical strain.

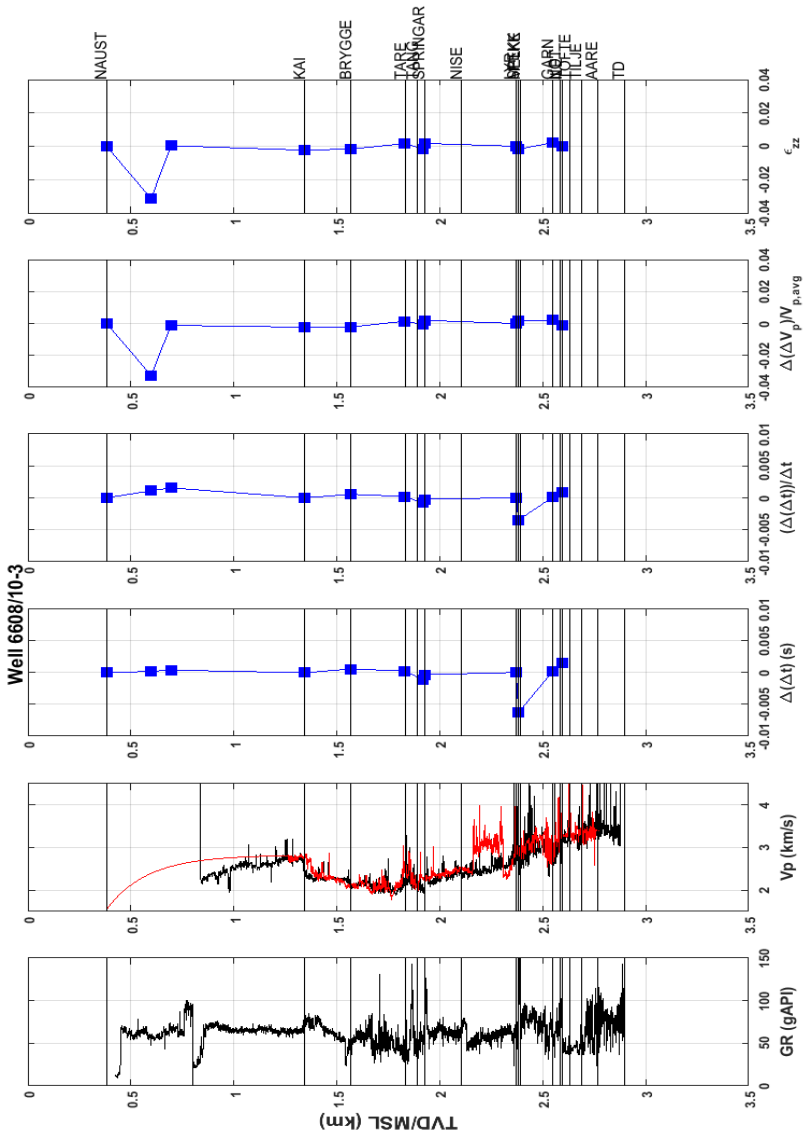

Figure 4.23: Well panel showing gamma-ray log, P-wave velocity log, timeshifts, relative timeshifts, relative velocity change and strain in well 6608/10-3, using Method 1.

The behaviour of the velocity log, timeshift-plot, relative timeshfit-plot, relative velocity change-plot and vertical strain-plot have been analyzed in order to see whether the speed-ups and slow-downs coincide, and are listed in table 4.3. It appears that in only the interval down to the Top Spekk horizon, all five parameters provide a unison conclusion, i.e. a speed-up determined by the velocity log, the timeshift and the relative velocity change and a negative strain. This subject is discussed further in Chapter 5.

Interval	$V_p - log$	$\Delta(\Delta t)$	$\frac{\Delta(\Delta t)}{\Delta t}$	$\frac{\Delta(\Delta V_p)}{V_p}$	ϵ_{zz}
Intra1 Naust	-	-	Slow-down	Slow-down	Negative
Intra2 Naust	-	-	Slow-down	Speed-up	Positive
Kai	Speed-up	Speed-up	Speed-up	Slow-down	Negative
Brygge	Slow-down	Slow-down	Slow-down	-	Negative
Intra Brygge	Speed-up	Speed-up	Speed-up	Speed-up	Positive
Intra Tare	Speed-up	Speed-up	Speed-up	Slow-down	Negative
Springar	Speed-up	Slow-down	Slow-down	Speed-up	Positive
Lyr	Speed-up	Slow-down	-	Slow-down	Negative
Spekk	Speed-up	Speed-up	Speed-up	Speed-up	Negative
Garn	Speed-up	Slow-down	Slow-down	-	Positive
Not	Speed-up	Slow-down	Slow-down	Slow-down	Negative

Table 4.3: The velocity behaviour indicated by the timeshifts, relative timeshifts, relative velocity change and vertical strain in well 6608/10-3, using Method 1.

The trend of the relative timeshift and relative velocity change plots can be further verified by figure 4.24 where the mean of each relative timeshift and relative velocity change interval are plotted together with the actual values for both parameters.

When the mean of the relative timeshift is negative it indicates a speed-up, while when the mean is positive it indicates a slow-down. When the mean of the relative velocity change is positive it indicates a speed-up, while when the mean is negative it indicates a slow-down.

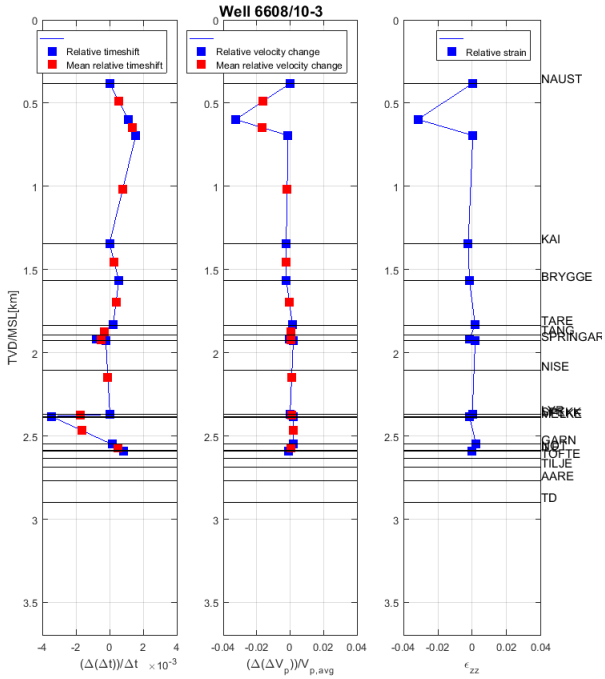

Figure 4.24: Relative timeshifts and relative velocity change plotted together with the mean of the start- and end-point of each interval marked with red squares, vertical strain and R-factor for well 6608/10-3, using Method 1.

4.4.3 Well 6608/10-4

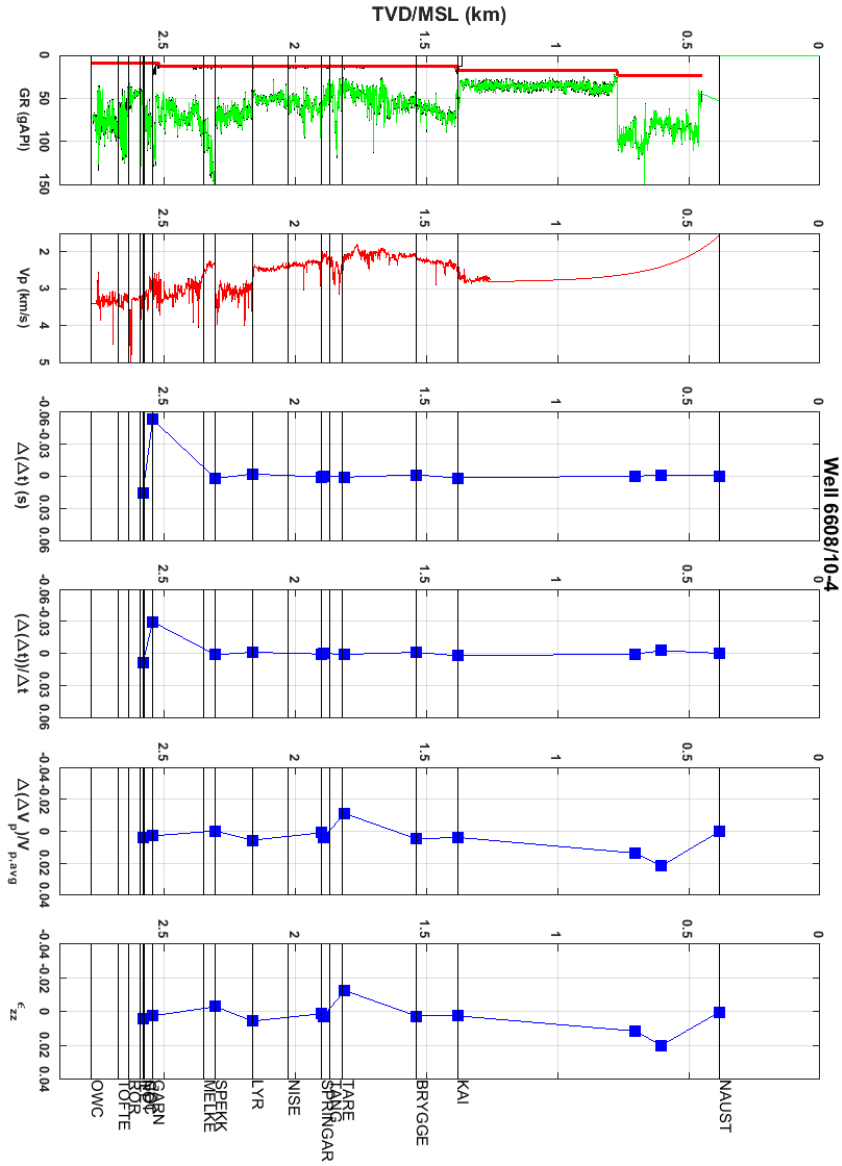

Figure 4.25: Well panel showing gamma-ray log, P-wave velocity log, timeshifts, relative timeshifts, relative velocity change and strain in well 6608/10-4, using Method 1.

The behaviour of the velocity log, timeshift-plot, relative timeshfit-plot, relative velocity change-plot and calculated vertical strain-plot have been analyzed in order to see whether the speed-ups and slow-downs coincide, and are listed in table 4.4.

It appears that in none of the intervals, all five parameters can provide a unison conclusion, e.g. in cases where a slow-down has been determined by the velocity log, the timeshift and the relative velocity change the calculated strain should according to the theory be positive, however, the opposite is determined from the calculations. This problem is discussed further in Chapter 5.

Interval	$V_p - log$	$\Delta(\Delta t)$	$\frac{\Delta(\Delta t)}{\Delta t}$	$\frac{\Delta(\Delta V_p)}{\bar{V_p}}$	ϵ_{zz}
Intra1 Naust	-	Speed-up	Speed-up	Speed-up	Positive
Intra2 Naust	-	Slow-down	Slow-down	Slow-down	Negative
Kai	Speed-up	Speed-up	Speed-up	Slow-down	Negative
Brygge	Slow-down	Speed-up	Slow-down	Speed-up	-
Intra Brygge	Speed-up	-	-	Slow-down	Negative
Intra Tare	Slow-down	-	Speed-up	Speed-up	Positive
Springar	Slow-down	Slow-down	Slow-down	Slow-down	Negative
Lyr	Speed-up	Speed-up	Speed-up	Speed-up	Positive
Spekk	Speed-up	Slow-down	Slow-down	Slow-down	Negative
Garn	Speed-up	Speed-up	Speed-up	Speed-up	Positive
Not	Slow-down	Slow-down	Slow-down	Speed-up	Negative

Table 4.4: The velocity behaviour indicated by the timeshifts, relative timeshifts, relative velocity change and vertical strain in well 6608/10-4, using Method 1.

The trend of the relative timeshift and relative velocity change plots can be further verified by figure 4.26 where the mean of each relative timeshift and relative velocity change interval are plotted together with the actual values for both parameters.

When the mean of the relative timeshift is negative it indicates a speed-up, while when the mean is positive it indicates a slow-down. When the mean of the relative velocity change is positive it indicates a speed-up, while when the mean is negative it indicates a slow-down.

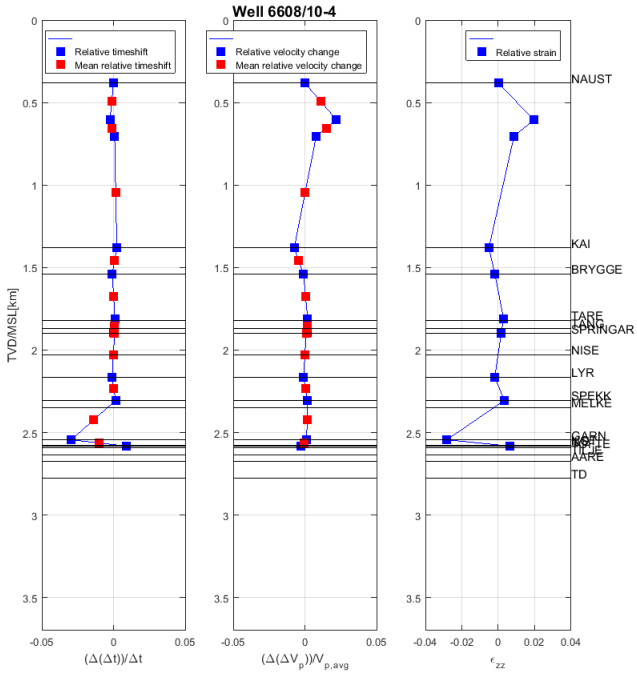

Figure 4.26: Relative timeshifts and relative velocity change plotted together with the mean of the start- and end-point of each interval marked with red squares, vertical strain and R-factor for well 6608/10-4, using Method 1.

Chapter 5

Discussion

5.1 Input Data and General Results

As described in Chapter 2, the data used in this thesis has been sourced from three different seismic cubes. The timeshift data has been sourced from the full-stack seismic cubes from 2001 and 2006, and is considered to be of good quality. The relative change in velocity has been sourced from the cube representing the difference between intercept cubes of 2006 minus 2001 ("ΔA Cube"), which has data of lesser quality than the full-stack cubes. The signal-to-noise ratio in theΔA Cube is low, as such, the noise can mask the signal to a certain degree. In the full-stack cubes, the signal to noise ratio is high, as such, the quality of the data is better with low masking of the signal by noise, which can be clearly seen in figure 3.7.

In addition, the ΔA Cube might have been shifted vertically compared to the original seismic cube. As the interpreted horizons in the full-stack cube were used as reference when calculating the sum of the intercept change in each interval, a shift of the ΔA Cube will result in some errors when calculating the relative velocity change.

When comparing the relative timeshifts with the relative velocity change, the desired outcome is that the parameters indicate speed-up and slow-down in the same intervals, i.e. negative timeshift in combination with positive relative velocity change and vice versa. From this, the desired outcome is that a speed-up corresponds to a compression and a slow-down corresponds to an elongation.

In intervals where the relative timeshift and relative velocity change do not predict the same velocity behaviour, it is reasonable to assume that the timeshift data is more reliable than the velocity change data, as this data is extracted from the ΔA Cube while the timeshift data is extracted from the full-stack cube which is, as previously mentioned, of higher quality than the ΔA Cube hence regarded as more reliable.

The desired outcome of the calculations of vertical strain as described in this

thesis is that the strain corresponds to the timeshift and relative velocity change, i.e. negative strain corresponds to negative timeshifts and positive relative velocity changes and positive strain corresponds to positive timeshifts and negative relative velocity changes. If there is no unison correspondence as described, it is fair to assume that the combination negative strain and negative timeshift or positive strain and positive timeshift is more reliable than the combination strain and relative velocity change based on the above discussion.

5.2 Timeshifts Through the Spekk and Garn Formations

The Garn formation is the shallowest reservoir formation in the Norne field, and the Spekk formation is the formation laying above the Melke formation, which is the cap rock. It is of interest to investigate the behaviour of the timeshifts through the Garn and Spekk formations, and by studying these two formations, it might be possible to detect timehifts and relative velocity change in the Garn formation due to changing fluid composition and pressure as the field is produced and to detect changes in the Spekk formation due to physical changes in the Garn formation. The discussion in this section relates to the four locations determined in this thesis, i.e. the three exploration wells and the location in Segment D.

In the well 6608/10-2 location, the timeshift and strain in the Garn and Spekk formations corresponds, whilst the relative velocity change does not correspond with the two aforementioned parameters, hence, one should rely on the timeshift calculations. The relative timeshifts through the Spekk and Garn formations in well 6608/10-2 are both negative. The well is located in Segment C, further away from the larger faults than the other two well locations studied in this thesis. There is a gas cap overlying the oil in this segment as well. When the oil is produced in this segment, water may have been injected leading to an increase in the density of the reservoir fluid, and in addition there may have been an increase in the reservoir pressure. It is likely that this has led to an increase in the velocity through the Garn formation. Due to the physical changes in the Garn formation, the stress in the Spekk formation may have increased causing a speed-up through this formation as well. Refer to figure 4.22 for further details.

In the well 6608/10-3 location, the timeshift and relative velocity change corresponds in the Garn formation, but not the calculated strain. In the Spekk formation, the timeshift and strain corresponds. Hence, one should rely on the timeshift calculations. The relative timeshifts through the Spekk and Garn formations in well 6608/10-3 are both positive. Segment E, where the well is located, has a gas gap overlaying the oil, with the well located fairly close to the gas-oil-contact. When the oil is produced from the reservoir, the gas may expand. This expansion may lead to a decrease in both the density of the reservoir fluid and pressure, which

again may cause the velocity through the Garn formation to decrease. As a result of the pressure decrease in Garn, the stress in the Spekk formation may decrease as well, causing a slow-down of the velocity through this formation. Refer to figure 4.24 for further details.

In the Garn formation in well 6608/10-4 location, the relative velocity change and calculated strain corresponds, whilst in the Spekk formation the timeshift and and relative velocity changes correspond, whilst the strain does not correspond. The question is which parameters shall be relied upon, and based on the above discussion, it is assumed that the timeshift data is the most reliable. The relative timeshifts through the Spekk and Garn formations in well 6608/10-4 are positive through the Spekk formation and negative through the Garn formation. Segment G only contains oil, thus when this oil is produced and water is injected into the reservoir, the density of the reservoir fluid will increase. The injection may have increased the reservoir pressure in the Garn formation, increasing the stress in the overlying formation, Spekk, resulting in velocity decrease through this formation. Refer to figure 4.26 for further details.

In the D location, due to the lack of a velocity log and a time-depth relationship, the strain has not been calculated. In both the Garn and Spekk formations, the timeshift and relative velocity changes correspond. The relative timeshifts through the Spekk and Garn formations along the point in Segment D are both positive. Since the timeshifts in this location cannot be compared to an actual well-log, the results are more uncertain than for the locations where well-logs are available. The point in Segment D is also located fairly close to a fault, and there is a gas cap overlying the oil in this segment of the reservoir as well. When the oil is produced, the gas may have expanded causing the density of the reservoir fluid and pressure to decrease, which may lead to a decrease in velocity. As a result of a likely decrease in reservoir pressure in the Garn formation, the stress in the Spekk formation may decrease as well, also causing a slow-down through this formation. Refer to figure 4.13 and 4.14 for further details.

Additional intervals are discussed in the sections below relating to the four different locations

Since the relative timeshifts and velocity changes are of a such magnitude that it is possible to analyze the trend of both graphs with the bare eye in well 6608/10-2, this well has been analyzed further.

5.3 Well 6608/10-2

When studying at figure 4.22, with the relative timeshift, velocity change and strain along well 6608/10-2, some of the intervals stand out with values of significant magnitude, as follows

- Seafloor - Intra1 Naust
- Seafloor - Intra Brygge
- Seafloor - Intra Tare
- Seafloor - Top Springar
- Seafloor - Top Spekk

The horizons named "Intra" represent reflectors of good quality that are located within the formations.

The interval from the seafloor to Intra1 Naust is dicussed further. The strain in this interval is positive, indicating an elongation of this part of the Naust formation. The relative timeshift and relative velocity change, on the other hand, indicates a speed-up which corresponds to negative strain, i.e. a compression of the formation. The trend where the calculated strain implies the opposite of what the relative timeshifts and velocity changes indicates continues throughout the entire well. These observations create uncertainty regarding the suitability of the theory behind the strain calculations defined in this thesis, for vertical strain calculations in cases with low relative compaction which is the case for most sandstone reservoirs.

In this case it is assumed that the formation is not expected to strain at all at shallow depths, thus the unlikely high value of calculated strain is discarded, assuming that $\epsilon_{zz} = 0$, the traveltime function (equation 2.2) is rewritten into the following

$$\frac{\Delta(\Delta t)}{\Delta t} = -\frac{\Delta(\Delta V_p)}{\overline{V_p}} \tag{5.1}$$

thus illustrating that the speed-up indicated by the relative timeshifts and relative velocity change is caused by something else than a compression/thickness change in the formation. As mentioned in Chapter 2, the velocity will increase with increasing pressure. Thus, the speed-up in this interval may be a result of just that, i.e. stress changes in the formation due to physical changes in the reservoir.

Through the lower part of the Naust formation, the calculated strain decreases and indicates compression, i.e. the opposite of what the relative timeshift and the relative velocity change indicates, which both imply a velocity slow-down that should correspond to positive strain. It may be the case that the stress in the lower part of the Naust formation has decreased due to different formation rock properties compared to the overlaying interval from the seafloor to Intra1 Naust. An explanation can be that the seafloor to Intra1 Naust interval is stiffer than the lower part of the Naust formation and creates an environment where lower Naust can ¨relax¨ causing a decrease in stress in this formation.

Assuming that the seismic data at shallow depths are unreliable, one can explain why the calculated vertical strain and relative velocity change is unreliable in for

instance the upper part of the Naust formation, from the seafloor down to Intra1 Naust.

In order to analyze and discuss the reliability of the strain calculation base in timeshifts and relative velocity changes, the interval from the seafloor to Intra Brygge has been studied, and the results are provided in table 5.1.

Parameter	**Value**
Measured $\Delta t_{IntraBrygge,01}$	1274 ms
Calculated $\frac{\Delta(\Delta t)}{\Delta t}$	-0.00154 (-0.154%)
Calculated $\Delta(\Delta t)$	-2 ms
Calculated $\Delta t_{IntraBrygge,06}$	1276 ms
Measured $V_{p,IntraBrygge,01}$	2076.38 m/s
Calculatred $\frac{\Delta(\Delta V_p)}{\overline{V_p}}$	-0.01107 (-1.107 %)
Calculated $\Delta(\Delta V_p)$	-22.99 m/s
Calculated $V_{p,IntraBrygge,06}$	2053.393 m/s
Measured $z_{IntraBrygge,01}$	1826 m
Calculated $\epsilon_{zz,IntraBrygge}$	-0.0126 (-1.26 %)
Calculated Δz	-23.01 m
Calculated $z_{IntraBrygge,06}$	1802.992 m

Table 5.1: Computation of traveltime change, velocity change and thickness change based on the results from the calculated relative velocity change and vertical strain when using Method 1, in the interval from the seafloor down to Intra Brygge.

As mentioned in Chapter 2, sandstone reservoirs with normal pressure (i.e. not HPHT) are not expected to compact of any significance, thus the calculated change in thickness of 23 m is unlikely and unrealistic. This is an argument for why it is reasonable to regard this result as unreliable and supports a view that the applied theory in this thesis for calculation of overburden strain in cases such as the Norne field is not suitable.

Because the Norne reservoir consist of sandstone, the reservoir compaction in this case is likely to be so small that it does not affect the thickness of the overburden, i.e. the thickness of the overburden does not change during production. However, the low compaction of the reservoir may have affected the stress distribution in the overburden which may be the reason for the observed timeshifts and the relative velocity changes.

5.4 Data Quality

The timeshifts and relative velocity changes have been sourced from different seismic data cubes that have been generated in two different ways. It is noteworthy that the trend of the two functions in all the well panels provided correspond to each other in most of the intervals. From this it can be observed that the relative velocity change data in the majority of the well has correct notation (positive or negative). However, the strain calculations may indicate that the magnitude of the relative velocity change is inaccurate.

Several uncertainties have to be taken into account regarding the seismic interpretation. The seismic data quality decreases with depth, making it difficult to interpret deep horizons. The difficulty may thus lead to errors in regards to the interpretation of the top of the Spekk, Garn and Not formations, especially in the areas where the formations are heavily faulted. Lyr consist of a very stiff rock type, marl, and the thickness of the formation vary a lot across the area covered by the seismic data cube. This may cause the underlying reflectors to "drown", i.e. decreasing the resolution and data quality.

5.5 4D Seismic versus Geomechanical Model and 4D Seismic

As mentioned in Chapter 1, a common approach used to model the vertical strain in the overburden is to use 4D seismic data in combination with a geomechanical model. The geomechanical models are heavily simplified, and assume that the overburden behave as a homogeneous rock mass which strain in the positive direction, i.e. elongate, as a result of reservoir compaction, and that the strain increases with depth and is at maximum just above the reservoir, as can be seen in figure D.2 in appendix D. This figure shows the modeled vertical strain along the centre line of a disk-shaped reservoir by using Geertsma's Nucleus of Strain model.

The calculated strain in this thesis is considered to be of low accuracy and thus cannot be directly compared to the modeled strain using Geertsma's strain model. The more reliable timeshifts and relative timeshifts indicate that the overburden does not act as a homogeneous rock mass. Instead these parameters indicate that the overburden is a complex, heterogeneous rock mass where every layer and rock type behave individually.

5.6 Strain Calculations using Method 1 and Method 2

As seen in table 4.2, the calculated strain by using Method 2 is far smaller in magnitude in the shallow intervals than when using Method 1. Thus, if the uncertainty of the ΔA Cube and relative velocity changes are disregarded, Method 2 is a better method to use when calculating the strain at depths with good seismic quality where there is low chance of misinterpretation. The reason for this is that a possible miscalculation in a shallow interval does not affect the calculated strain in a deeper interval.

In the deeper intervals, Method 1 yields a more realistic calculated strain than Method 2. This may be due to the sensitivity of Method 2 when it comes to errors regarding the ΔA Cube. In addition the deep formations in the Norne field are heavily faulted which may have led to misinterpretations at deep depths which may be what have induced the unlikely high calculated strain.

When comparing relative velocity changes with calculated strain, Method 2 show the same behaviour as Method 1, where the expected correlation between strain and relative velocity change, i.e. speed-up of velocity and negative strain and vice versa, is not present. As such, it appears that for strain calculations in the overburden above fields with expected low compaction, both Method 1 and Method 2 are unreliable.

Chapter 6

Conclusions

Method 1 is regarded to be more robust than Method 2 due to the methods used to calculate the parameters through the intervals. When the reference horizon is kept constant at the seafloor, which is the case for Method 1, the possible errors related to the seismic interpretation will have less impact on the summation of values, than for Method 2 where the values are calculated from one horizon to the next.

Comparison of the strain calculations from Method 1 and Method 2 with the trends in the timeshifts and relative velocity change shows that the strain calculations are the opposite of what can be expected from the timeshift data. In addition, it has been shown that the strain calculation results in physical results that are unrealistic. There are several reasons for this, it can be caused by data quality, interpretation errors, as well as the theory not being suitable for strain calculations in the overburden above sandstone reservoirs such as in the Norne field with a relative low expected compaction.

As both Method 1 and Method 2 yields the same results when calculating the accumulated timeshifts, these results are regarded as reliable. Thus, it can be concluded that based on the timeshift data the overburden acts as a heterogeneous mass where each layer behave individually when exposed to physical changes in the reservoir. Hence one can also conclude that the stress sensitivity of the overburden is different in each formation, and varies based on the rock type in that specific formation.

Method 1 and 2 does not yield the same results for the accumulated relative velocity change through the formation. This indicates that the intercept change data is unreliable as the relative velocity changes through the formations are different when using the two methods. It is reasonable to conclude that Method 1 is more thrust worthy than Method 2, as Method 1 calculates the accumulated relative velocity change from the seabed and down to each reflector while Method 2 calculates the relative velocity change in each interval, thus making Method 2 more sensitive to misinterpretations and other types of errors than Method 1.

From the observations that the calculated accumulated timeshifts are the same

for methods 1 and 2, and the calculated relative velocity changes are different for methods 1 and 2, one can conclude that in case of the Norne seismic data sets, the timeshift data is more reliable than the relative velocity change data.

The change in timeshifts from the 2001 seismic survey to the 2006 seismic survey may be a result of both thickness and velocity changes in the overburden. Since the Norne field is a sandstone reservoir, the compaction of the reservoir is believed to be so small that the thickness of the overburden remains constant throughout the production period, i.e. strain is zero. Thus, the change in timeshifts and relative velocity change is most likely caused by stress changes in the overburden which are induced by physical changes in the reservoir.

In the case of the Norne field and the 2001 and 2006 seismic data sets, the strain calculations are concluded to be unreliable because the correspondence between the relative timeshifts and the calculated strain is to a large degree non-existing. In addition, the calculated strain values for the overburden are shown to be unrealistic and outside the scale of what can be expected for cases such as Norne.

Many geomechanical models for overburden strain calculations are based on an assumption that the overburden acts as one homogenous layer of rock. The timeshifts data has demonstrated that the overburden, which by nature is heterogeneous, has a far more complex behaviour than what is assumed in simplified and homogeneous geomechanical models. Thus it can be concluded that the geomechanical models used to calculate strain are too simplified and models reflecting the actual heterogeneity of the overburden need to be built for strain calculations.

If the uncertainty of the ΔA Cube and the relative velocity changes are disregarded, Method 2 yields more reliable calculated strain at shallow depths than Method 1 because the strain is not accumulated through the overburden and instead calculated separately in every interval. Thus, a possible miscalculation in a shallow interval does not affect the calculated strain in a deeper interval.

At deeper depths, Method 1 yields more realistic values when it comes to strain. Method 2 is more sensitive to errors, and since the deep formations are heavily faulted this may have caused misinterpretations. Thus, Method 2 may be more robust when the seismic is of good quality.

Chapter 7

Further Work

Based on the work herein, there are several issues that can be investigated further.

As a further investigation of the Norne field, it would be interesting to analyze the Lyr formation. The Lyr formation consist of a very stiff rock type, thus it would be interesting to investigate whether the magnitude of the speed-up/velocity increase through the formation increase with the formation thickness.

If that is the case, the timeshift through Lyr in well 6608/10-4 should be larger in magnitude than the timeshift in well 6608/10-2 which again should be larger in magnitude than the timeshift in well 6608/10-3, as the thickness of the Lyr formation is largest in well 6608/10-2 and thinnest in well 6608/10-3.

As this thesis involved seismic data from a sandstone reservoir it would be interesting to apply the same method to a chalk reservoir, for instance the Ekofisk of Valhall fields, where the subsidence of the seabed is known in order to see if the calculated results are similar to what is observed in real life.

Bibliography

[1] Npd factpages.

[2] Youness El Ouair, Magne Lygren, Bard Osdal, Oddvar Husby, Martin Springer, et al. Integrated reservoir management approach: From time-lapse acquisition to reservoir model update at the norne field. In *International Petroleum Technology Conference*. International Petroleum Technology Conference, 2005.

[3] Martin Landrø and Lasse Amundsen. Introduction to exploration geophysics with recent advances, 2018.

[4] Rob Simm and Mike Bacon. Fundamentals. In *Seismic Amplitude*, pages 3–22. Cambridge University Press, Cambridge, 2014.

[5] R. Simm and M. Bacon. *Fundamentals*, page 3–22. Cambridge University Press, 2014.

[6] Robert E Sheriff. Exploration seismology, 1995.

[7] Z. (Zee) Wang. Y2k tutorial: Fundamentals of seismic rock physics. *Geophysics*, 66:398–412, 03 2001.

[8] WsternGeco. Data processing report for statoil block 6608/10 (norne) st0113, st0103, st0305, st0409, st0603 2006 4d, 2007.

[9] E. Fjær, R.M. Holt, P. Horsrud, R.M. Raaen, and R. Risnes. Reservoir geomechanics. In *Petroleum related rock mechanics*, volume 33 of *Developments in petroleum science*, pages 287–340. Elsevier, 1992.

[10] Martin Landrø and Jan Stammeijer. Quantitative estimation of compaction and velocity changes using 4d impedance and traveltime changes. pages 949–957, 2004.

[11] P. Hatchell and S. Bourne. Rocks under strain: Strain-induced time-lapse time shifts are observed for depleting reservoirs. *Leading Edge (Tulsa, OK)*, 24(12):1222–1225, 2005.

[12] Thomas Røste, Ole Petter Dybvik, and Ole Kristian Søreide. Overburden 4d time shifts induced by reservoir compaction at snorre field. *The Leading Edge*, 34(11):1366–1374, 2015.

[13] A. Tura, T. Barker, P. Cattermole, C. Collins, J. Davis, P. Hatchell, K. Koster, P. Schutjens, and P. Wills. Reservoir performance and monitoring: Monitoring primary-depletion reservoirs with seismic amplitudes and time shifts. *JPT, Journal of Petroleum Technology*, 58(9):96–100, 2006.

[14] N. Hodgson, C. MacBeth, L. Duranti, J. Rickett, and K. Nihei. Inverting for reservoir pressure change using time-lapse time strain: Application to genesis field, gulf of mexico. *The Leading Edge*, 26(5):649–652, 2007.

[15] Thomas Røste, Alexey Stovas, and Martin Landrø. Estimation of layer thickness and velocity changes using 4d prestack seismic data. *GEOPHYSICS*, 71(6):S219–S234, 2005.

[16] J.P. Castagna, H.W. Swan, and D.J. Foster. Framework for avo gradient and intercept interpretation. *Geophysics*, 63(3):948–956, 1998.

[17] Jerome Guilbot and Brackin Smith. 4-d constrained depth conversion for reservoir compaction estimation: Application to ekofisk field. *The Leading Edge*, 21(3):302–308, 2002.

[18] Lene Lykke Erichsen. Estimation of vertical strain in overburden using synthetic 4d seismic data. 2017. Trondheim, Norway, 2017.

[19] Helge M Gjerstad, Jan I Skagen, et al. The norne field-exploration history & reservoir development strategy. In *Offshore Technology Conference*. Offshore Technology Conference, 1995.

[20] S. B. Verlo and M Hetland. Development of a field case with real production and 4d data from the norne field as a benchmark case for future reservoir simulation models testing. 2008. Trondheim, Norway, 2008.

[21] A.W. Martinius, P.S. Ringrose, C. Brostrøm, C. Elfenbein, A. Næss, and J.E. Ringås. Reservior challenges of heterolithic tidal sandstone resevoirs in the halten terrace, mid-norway. *Petroleum Geoscience*, 11(1):3–16, February 2005.

[22] Statoil ASA. Annual reservoir development plan norne and urd field, 2006.

[23] Chapter 3 - understanding seismic exploration. In Enwenode Onajite, editor, *Seismic Data Analysis Techniques in Hydrocarbon Exploration*, pages 33 – 62. Elsevier, Oxford, 2014.

[24] M. Landrø. 4d seismic. In *Petroleum Geoscience: From Sedimentary Environments to Rock Physics, Second Edition*, pages 489–514. Springer Berlin Heidelberg, 2015.

[25] Victor Aarre. Estimating 4d velocity changes and contact movement on the norne field. In *SEG Technical Program Expanded Abstracts 2006*, pages 3115–3119. Society of Exploration Geophysicists, 2006.

[26] Martin Landrø, Odd Arve Solheim, Eilert Hilde, Bjorn Olav Ekren, and Lars Kristian Stronen. The gullfaks 4d seismic study. *Petroleum Geoscience*, pages 213–226, 1999.

[27] P. J. Hatchell and S. J. Bourne. Measuring reservoir compaction using time-lapse timeshifts. volume 24, Tulsa, OK, 2005. Society of Exploration Geophysicists.

[28] Paul A Tipler and G Mosca. *Newton's Laws*, pages 93 – 126. Freeman, New York, 6th ed. edition, 2008.

[29] Philip Kearey. An introduction to geophysical exploration, 2002.

[30] Kenneth Duffaut. Amplitude versus offset or angle. TPG4170, 2018.

[31] A.P. Bathija, M.L. Batzle, and M. Prasad. An experimental study of the dilation factor. *GEOPHYSICS*, 74(4):E181–E191, 2009.

[32] Franciscus Matheus Marie Mulders. Modelling of stress development and fault slip in and around a producing gas reservoir. 2003.

[33] Fanliao Wang, Xiangfang Li, Gary Couples, Juntai Shi, Jinfen Zhang, Yanick Tepinhi, and Ling Wu. Stress arching effect on stress sensitivity of permeability and gas well production in sulige gas field. *Journal of Petroleum Science and Engineering*, 125:234–246, 2015.

[34] Robert Leo Mann and Irving Fatt. Effect of pore fluids on the elastic properties of sandstone. *Geophysics*, 25(2):433–444, 1960.

[35] P. Tempone, E. Fjær, and M. Landrø. Improved solution of displacements due to a compacting reservoir over a rigid basement. *Applied Mathematical Modelling*, 34(11):3352–3362, 2010.

[36] R.M. Holt, E. Fjær, O.M. Nes, J.F. Stenebraten, et al. Strain sensitivity of wave velocities in sediments and sedimentary rocks. In *The 42nd US Rock Mechanics Symposium (USRMS)*, 2008.

Appendix A

Results - Method 2

In this chapter, results from Method 2 are provided, where the analyzed parameters have been summed between each of the interpreted horizons.

A.1 Traveltime and Amplitude Analysis at Four Specific Locations

The timeshfits, relative timeshifts and relative velocity changes have been analyzed in four specific locations in the Norne field, one in each segment. The locations in Segments C, E and G are the exploration wells 6608/10-2, 6608/10-3 and 6608/10-4, whilst the location in Segment D was selected based on detection of timeshifts at the location.

The analysis of the timeshifts, relative timeshifts and relative velocity change calculations applying Method 2 follows.

A.1.1 Well 6608/10-2 - Segment C

Figures A.1-A.3 shows the results from the calculation of timeshifts, relative timeshifts and relative velocity change through exploration well 6608/10-2 located in Segment C, using Method 2.

The calculated timeshifts are negative and increasing in magnitude through the first four intervals from the seafloor down to the top of the Brygge formation, indicating a speed-up as seen in figure A.1. From the top of the Brygge formation down to the top of the Springar formation, the timeshifts are positive, indicating a slow-down. The timeshifts through the Springar and Lyr formations are negative, indicating a speed-up. From the top of the Spekk formation until the top of the Not formation, i.e. through the Spekk, Melke and Garn formations, the timeshifts

are positive, indicating a slow-down.

The accumulation of the timeshifts are shown in figure B.58 in appendix B. This figure is identical to figure 4.3 presented in Chapter 4, acting as a verification that Method 2 actually calculates the timeshifts in each interval and that Method 1 calculates the accumulated timeshifts down to each horizon included in the analysis.

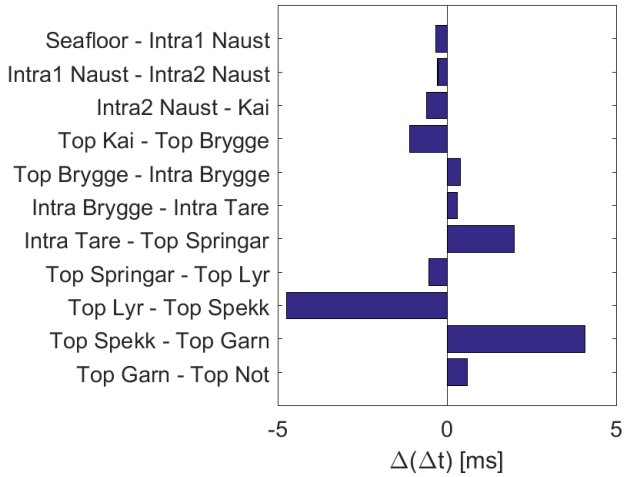

Figure A.1: Timeshifts between each horizon in well 6608/10-2, using Method 2.

Figure A.2 shows the relative timeshifts through each formation in well 6608/10-2. Four intervals clearly stand out, Intra Tare to the top of the Springar formation, the Lyr, Spekk and Garn formations, indicating that the timeshifts in these intervals are large compared to the timethickness in the same interval.

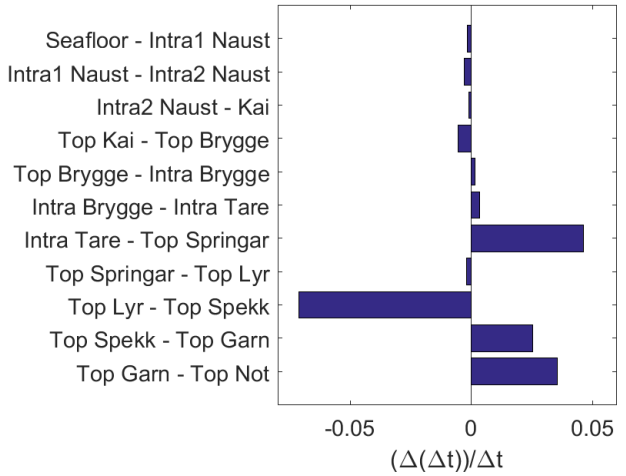

Figure A.2: Relative timeshifts between each horizon in well 6608/10-2, using Method 2.

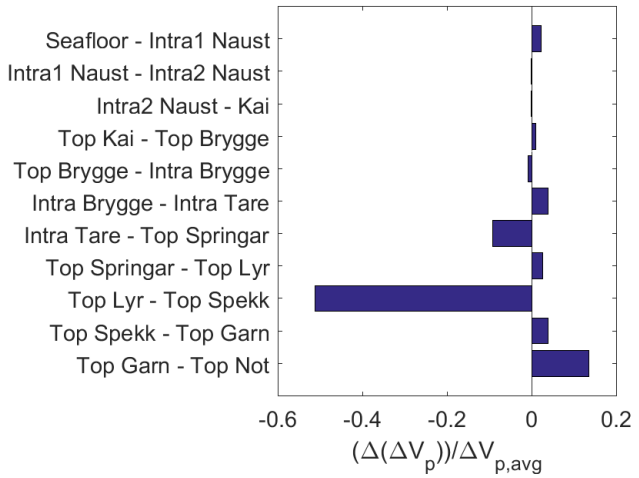

Figure A.3: Relative velocity change between each horizon in well 6608/10-2, using Method 2.

The relative velocity change in figure A.3 indicates a slight speed-up in the upper most part of the Naust formation, followed by a slow-down through the middle and lower part of the Naust formation. The positive relative velocity change through the Kai formation indicates a speed-up. Through the upper part of the Brygge

formation, there is a slight slow-down, followed by a speed-up from Intra Brygge to Intra Tare.

From Intra Tare down to the top of the Springar formation, the velocity change can be interpreted as a slow-down, followed by a speed-up through the Springar formation. The velocity change through the Lyr formation is negative, indicating a slow-down, followed by a speed-up through the Spekk and Garn formations.

A.1.2 Well 6608/10-3 - Segment E

Figures A.4-A.6 shows the analysis of timeshifts, relative timeshifts and relative velocity change through exploration well 6608/10-3 located in Segment E, using Method 2.

The timeshifts through the upper and middle parts of the Naust formation are positive, indicating a slow-down, followed by a speed-up through the lower part of the Naust formation down to the top of the Kai formation. From the top of the Kai formation down to the top of the Brygge formation the timeshift is positive, indicating a slow-down. The timeshift through the Brygge formation down to a reflector inside the Tare formation is negative, indicating a speed-up that increases with depth.

Through the two intervals from Intra Tare down to the top of the Lyr formation the timeshifts are positive and decreasing with depth, indicating a slow-down that decrease with depth when approaching the Lyr formation. Through the Lyr formation there is a significant speed-up, followed by a slow-down through the Spekk and Garn formations.

The accumulated timeshifts from well 6608/10-3 is shown in figure B.59 in appendix B.

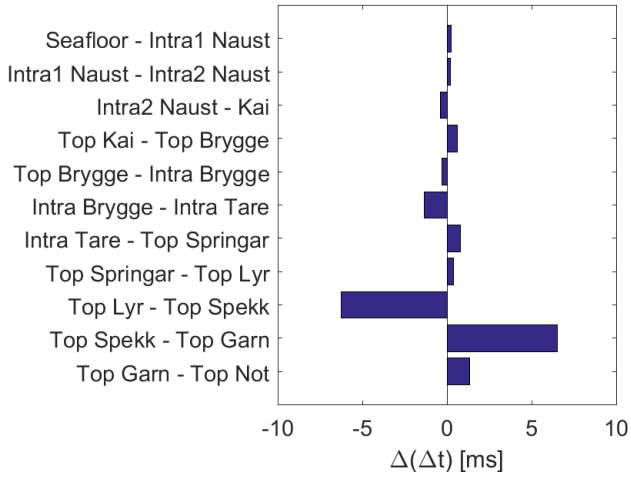

Figure A.4: Timeshifts between each horizon in well 6608/10-3, using Method 2.

The relative timeshifts shown in figure A.5 through the shallow formations are small. The relative timeshift through the Lyr, Spekk and Garn formations are larger in magnitude compared to the other intervals, indicating that the timeshifts through these formations are large compared to the timethickness through the same intervals.

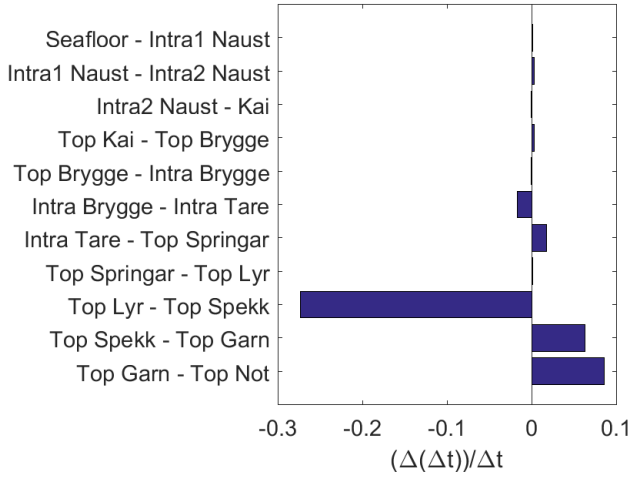

Figure A.5: Relative timeshifts between each horizon in well 6608/10-3, using Method 2.

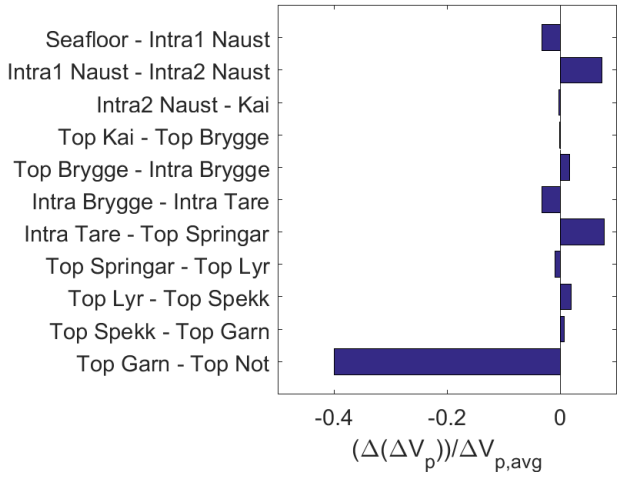

Figure A.6: Relative velocity changes between each horizon in well 6608/10-3, using Method 2.

The relative timeshifts through the Naust formation show a slow-down in the upper most part, followed by a speed-up through the middle part which again is followed by a slight slow-down. This slow-down continues through the Kai formation and is followed by a speed-up through the upper part of the Brygge formation.

The velocity change from Intra Brygge to Intra Tare is negative, indicating a slow-down, followed by a speed-up down to the top of the Springar formation. From the top of the Springar formation down to the top of the Lyr formation the velocity change is negative, indicating a slow-down before the velocity change again is positive through the Lyr formation. The speed-up continue through the Spekk formation before the velocity again decrease through the Garn formation.

A.1.3 Well 6608/10-4 - Segment G

Figures A.7-A.9 shows the analysis of the timeshifts, relative timeshifts and relative velocity change through exploration well 6608/10-4 located in Segment G, using Method 2.

The timeshifts through the Naust formation is negative in the upper most part and positive in the middle and lower most part, indicating a speed-up followed by an increasing slow-down. The timeshift through the Kai formation is negative indicating a speed-up, followed by a slow-down through the upper most part of the Brygge formation.

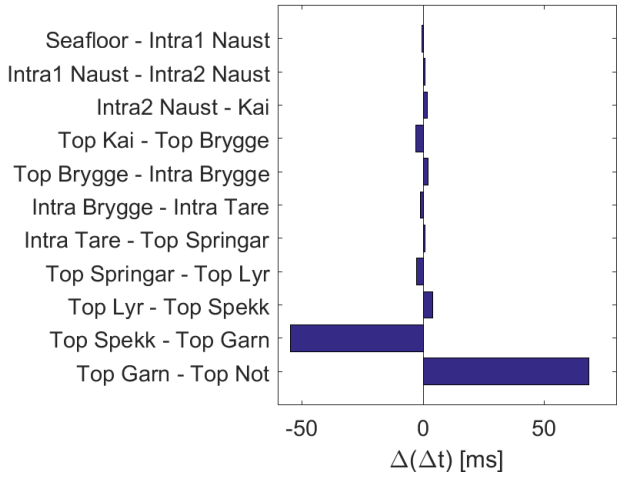

Figure A.7: Timeshifts between each horizon in well 6608/10-4, using Method 2.

From Intra Brygge to Intra Tare the time timeshift is negative, indicating a speed-up, followed by a slow-down from Intra Tare to the top of the Springar formation.

The timeshift through the Springar formation is negative which indicates a speed-up, followed by a slow-down through the Lyr formation. The timeshift through the Spekk formation indicates a speed-up while the timeshift through the Garn formation indicates a slow-down.

The accumulated timeshifts from well 6608/10-4 is shown in figure B.60 in appendix B.

The relative timeshifts shown in figure A.8 are very small for every interval except through the Garn formation which indicates that the timeshift in this formation is large compared to the timethickness.

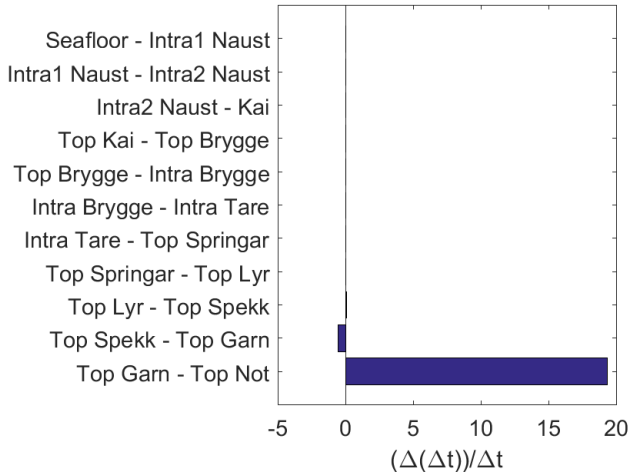

Figure A.8: Relative timeshifts between each horizon in well 6608/10-4, using Method 2.

The relative velocity change in the Naust formation is positive in the upper most part and negative in the middle and lower most part, indicating a speed up followed by a slow-down. Through the Kai formation and upper part of the Brygge formation the relative velocity change is positive, indicating a speed-up.

Through the three intervals from Intra Brygge down to the top of the Lyr formation the velocity change is negative, indicating a slow-sown, followed by a speed-up through the Lyr formation. The velocity change through the Spekk and Garn formations indicate a slow-down which increase with depth.

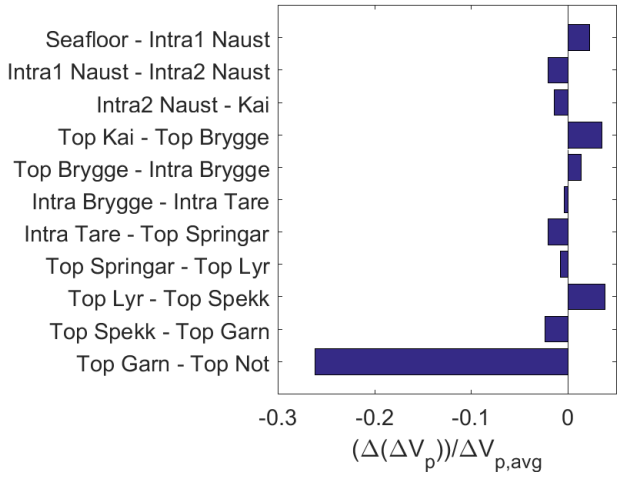

Figure A.9: Relative velocity changes between each horizon in well 6608/10-4, using Method 2.

A.1.4 Location in Segment D

Figures A.10-A.12 shows the analysis of the timeshifts, relative timeshifts and relative velocity change through the location in Segment D, using Method 2.

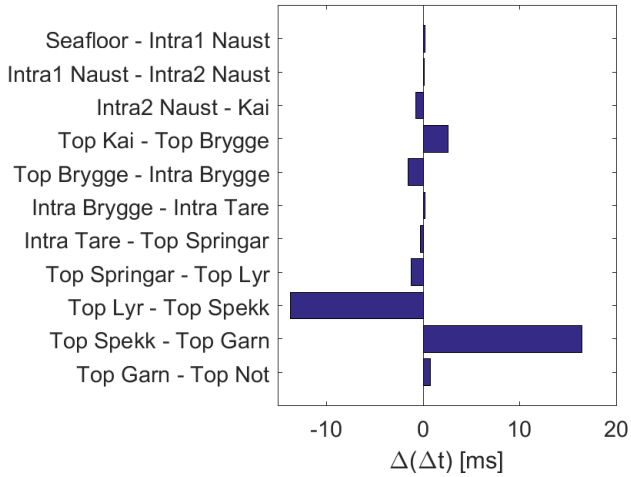

Figure A.10: Timeshifts between each horizon in Segment D, using Method 2.

The timeshifts through the upper parts of the Naust formation are positive, indicating a slow-down, followed by a speed-up through the lower most part of the formation. The positive timeshift through the Kai formation indicate a slow-down.

The timeshift through the upper part of the Brygge formation indicate a speed-up followed by a slight slow-down from Intra Brygge to Intra Tare. The negative timeshift from Intra Tare to the top of the Springar formation indicate a slight speed-up, which continue but decrease in magnitude through the Springar formation.

The timeshift through the Lyr formation is negative and large in magnitude, indicating a significant speed-up, followed by a significant slow-down through the Spekk formation which continue through the Garn formation.

The accumulated timeshifts from Segment D is shown in figure B.61 in appendix B.

The relative timeshifts shown in figure A.11 are very small for all formations down to the top of the Lyr formation. The relative timeshift through the Lyr, Spekk and Garn formations are large in magnitude compared to the other intervals, indicating that the timeshifts through these intervals are large compared to the timethickness through the same intervals.

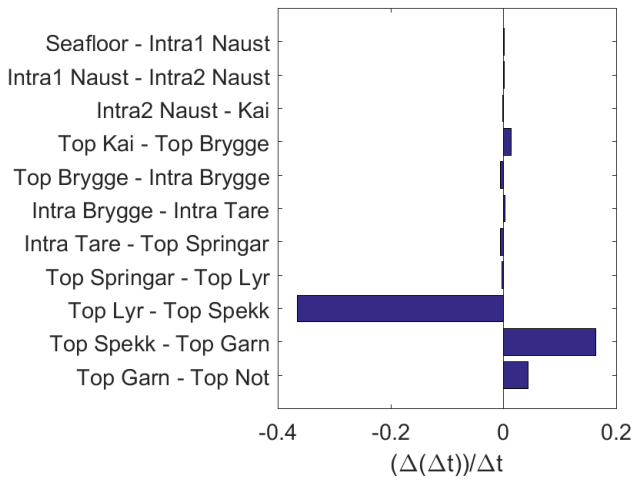

Figure A.11: Relative timeshifts between each horizon in Segment D, using Method 2.

The relative velocity change in the Naust formation is negative in the upper most part of the formation, positive in the middle part and negative in the lower most part, which indicates a slow-down, speed-up and then slow-down.

The relative velocity change is positive and increase in magnitude from the top of the Kai formation down to Intra Tare, indicating a slow-down in this part of the subsurface. The velocity change from Intra Tare to top of the Springar formation is negative which indicates a slow-down, followed by a speed-up through the Springar and Lyr formations. The relative velocity change through the Spekk and Garn formations are negative, incidating a slow-down.

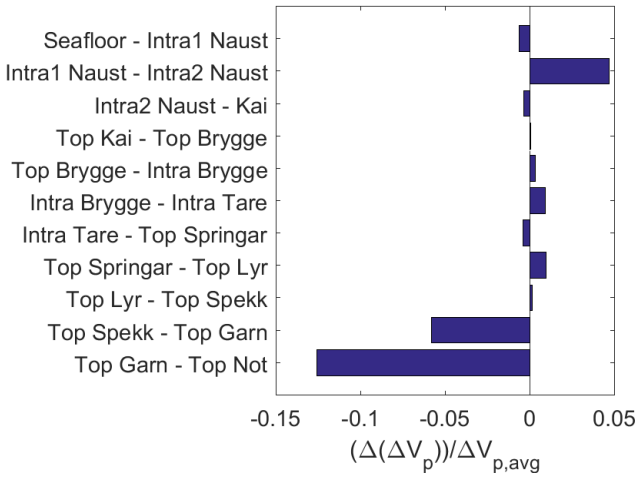

Figure A.12: Relative velocity changes between each horizon in Segment D, using Method 2.

A.2 Map View

The timeshfits, relative timeshifts and relative velocity change have been analyzed in map view at every interpreted horizon. The six following figures (A.13-A.18) shows the aforementioned parameters at the top of the Garn and Not formations, respectively, i.e. the last formation top before the reservoir and the first formation top inside the reservoir.

These formation tops were chosen because the change on top and inside the reservoir is expected to be opposite of each other. When there is a speed-up in the reservoir due to for instance compaction, the velocity right above the reservoir is expected to slow down.

A.2.1 Timeshift Analysis

The timeshifts have been calculated using equation (3.11) presented in section 3.3.2.

Figures B.28-B.37 in Appendix B shows the timeshifts in each interval defined in the subsurface, i.e the timeshifts throught the formations in the cases where both horizons represent formation top.

Figures B.28-B.30, which represent the timeshifts from the seafloor down to Intra1 Naust and from Intra1 Naust down to Intra2 Naust, and from Intra2 Naust down to the top of the Kai formation, show almost no timeshifts. In figure B.31, timeshifts are visible in a clear pattern following the outline of the faults in the Brygge formation. These timeshifts are gone on the next figure (figure B.32) which represents the timeshifts from top of the Brygge formation down to Intra Brygge, as well as on figure B.33 representing the timeshifts from Intra Brygge to a reflector inside the Tare formation, Intra Tare.

In figures B.35 and B.36 the timeshifts are clearly visible. In figure B.35 which shows the timeshifts from the top of the Springar formation down to the top of the Lyr formation, small negative timeshifts are visible in Segment D and G. These negative timeshifts cover larger areas in Segment C, D and G, as well as some positive timeshifts in Segment C, E and G in figure B.36 which shows the timeshifts through the Lyr formation.

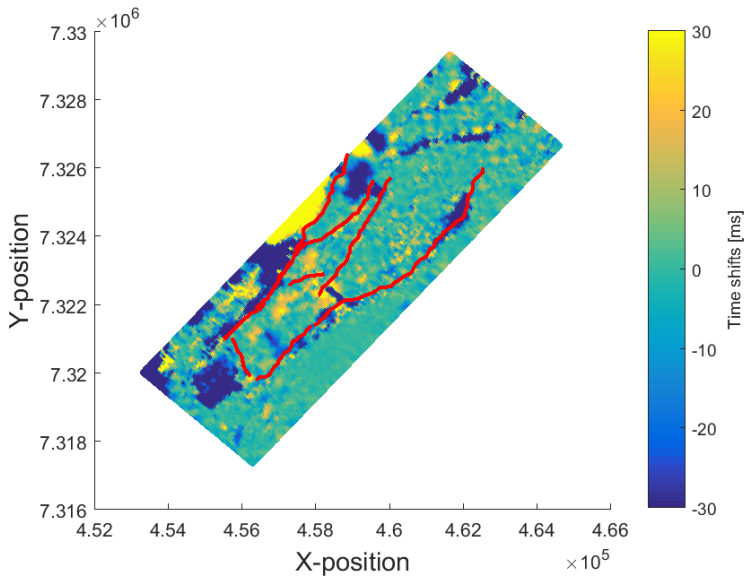

Figure A.13: Timeshifts from the top of the Spekk formation down to top of the Garn formation, i.e. through the Spekk formation, using Method 2.

On figure B.37 which shows the timeshifts from the top of the Spekk formation down to the top of the Garn formation, i.e. the timeshifts through the Spekk formation, the timeshifts are covering an even bigger area, but the timeshifts that were negative through Lyr have become positive through Spekk, and the timeshift that were positive have become negative.

On figure A.14 the pattern that was visible in the two previous figures is no longer present. Some negative timeshifts are visible along the fault line in Segments E and G. Positive timeshifts are visible between Segments C and G.

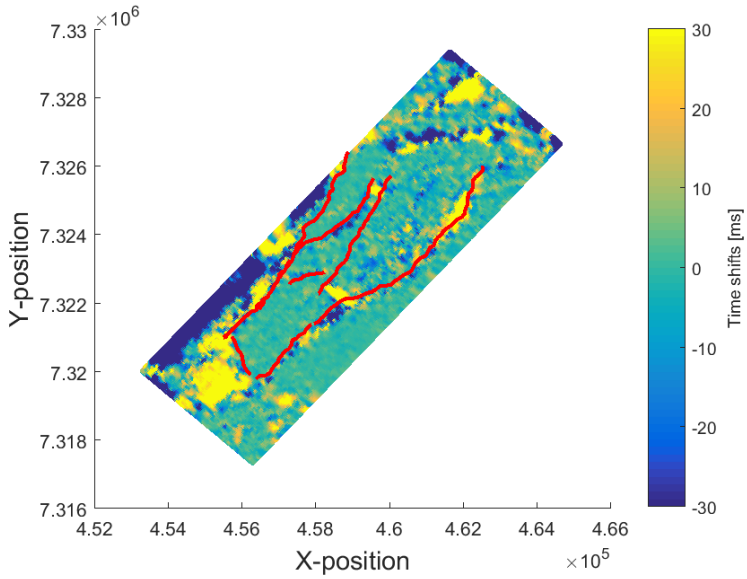

Figure A.14: Timeshifts from the top of the Garn formation to top of the Not formation, i.e. through the Garn formation, using Method 2.

A.2.2 Relative Timeshift Analysis

Figures B.38-B.47 show the relative timeshifts in the subsurface related to Method 2. As expected, the relative timeshifts at shallow depths in the subsurface are very small. When reaching the formations where timeshifts are visible (as mentioned previously in this section), so are the relative timeshifts. In figure B.41 which are showing the relative timeshifts at the top of the Brygge formation, both negative and positive timeshifts are visible, creating a pattern probably due to the faults in the formation. The same pattern is visible in figure B.42 which shows the timeshifts through the upper part of the Brygge formation. In figure B.44, which is showing the relative timeshifts through the Springar formation, there are visible relative timeshfits that might be following the fault pattern. In addition, there are negative

relative timeshifts in Segment C, D and G, as well as some positive relative timeshift scattered around. The relative timeshifts increase a lot on the following plots, and in figure A.16 the whole surface is covered in timeshifts, indicating that all points in the Garn formation have been affected by something that results in either positive (slow-down) or negative (speed-up) timeshifts.

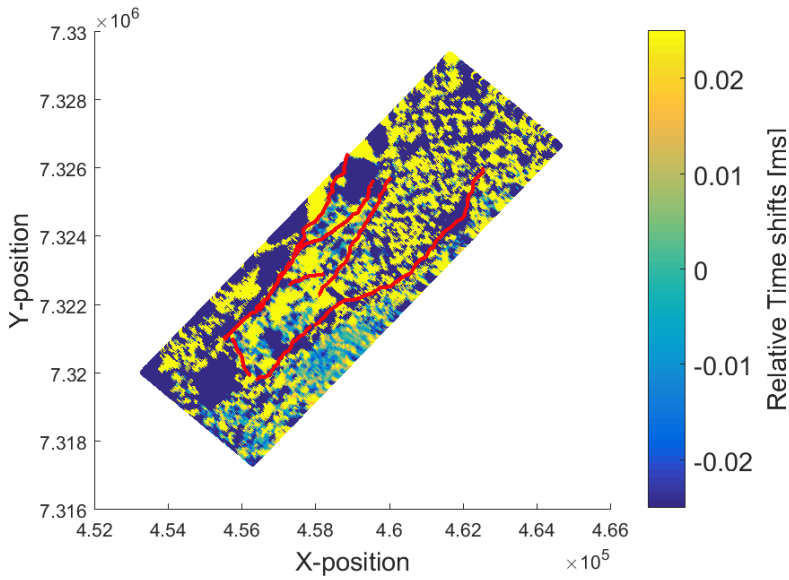

Figure A.15: Relative timeshifts from the top of the Spekk formation down to top of the Garn formation, i.e. through the Spekk formation, using Method 2.

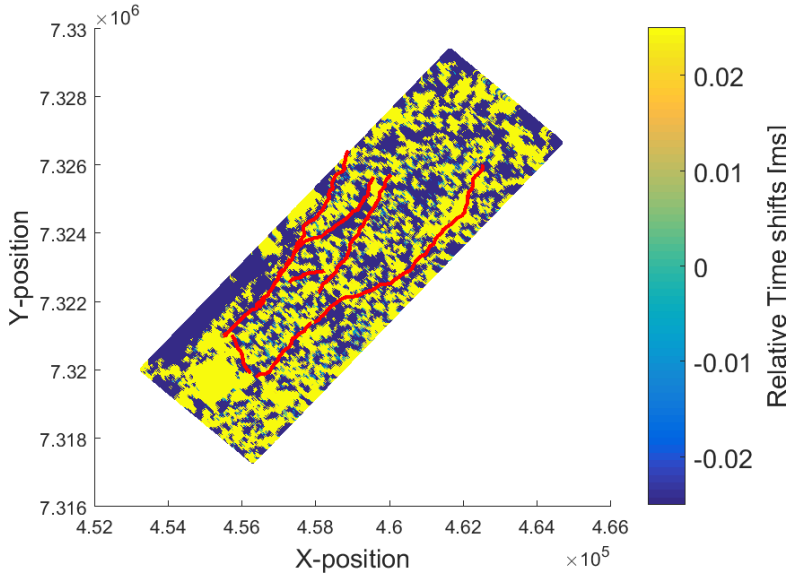

Figure A.16: Relative timeshifts from the top of the Garn down to top of the Not formation, i.e. through the Garn formation, using Method 2.

A.2.3 Analysis of Relative Velocity Change

Figures B.48-B.57 show the relative velocity change ($\frac{\Delta(V_p)}{V_p} = 2 * \sum \Delta A$) between each horizon from Intra1 Naust to the top of the Garn formation. The first two figures, B.48-B.49 show the velocity change from the seafloor to Intra1 Naust, and from Intra1 Naust to Intra2 Naust. The figures show a significant relative velocity change in the upper part of the subsurface. The velocity change does not continue in the following intervals from the top of the Kai formation to the reflector inside the Brygge formation, Intra Brygge, as seen in figures B.50 to B.52.

According to figure B.53 the lower part of the Brygge formation down to a reflector inside the Tare formation, Intra Tare, experience a velocity change. The velocity continue to change, mostly as a slow-down, from Intra Tare to the top of the Springar formation, according to figure B.54. According to figure B.55, the Springar formation experience little velocity change, while figure B.56 show some velocity changes through the Lyr formation, but in a meaningless pattern randomly distributed around the surface.

Figure B.57 show velocity changes in a more meaningfull pattern than the previous figures. It looks like Segment G experience a slow down in the area close to Segment C (south-west) while there is a speed up in the outer part of the segment

(north-east). The other segments experience a slight velocity change compared to the other parts of the figure. The same pattern is visible in figure A.18 but the difference is that the velocity changes in Segment C, D and E are larger than the changes in Segment G. The velocity change in Segment C and D indicate mostly a slow-down, while the velocity change in Segment E indicate a speed-up.

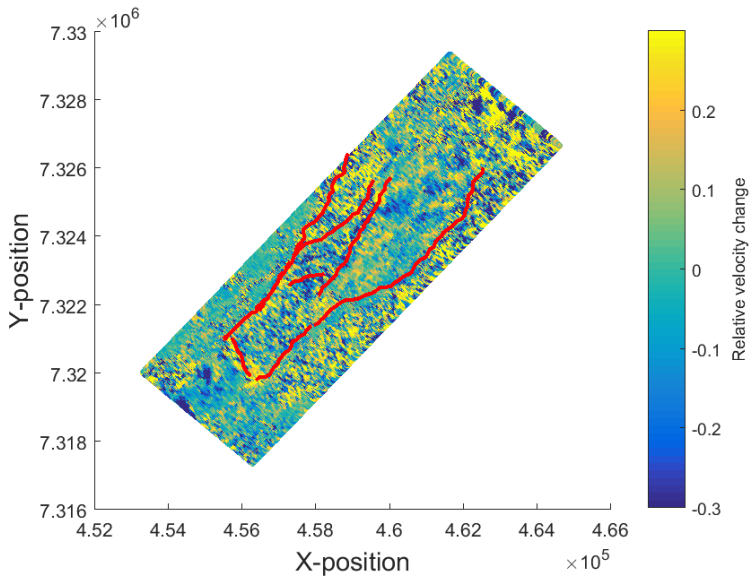

Figure A.17: Relative velocity changes from the top of the Spekk formation down to top of the Garn formation, i.e. through the Spekk formation, using Method 2.

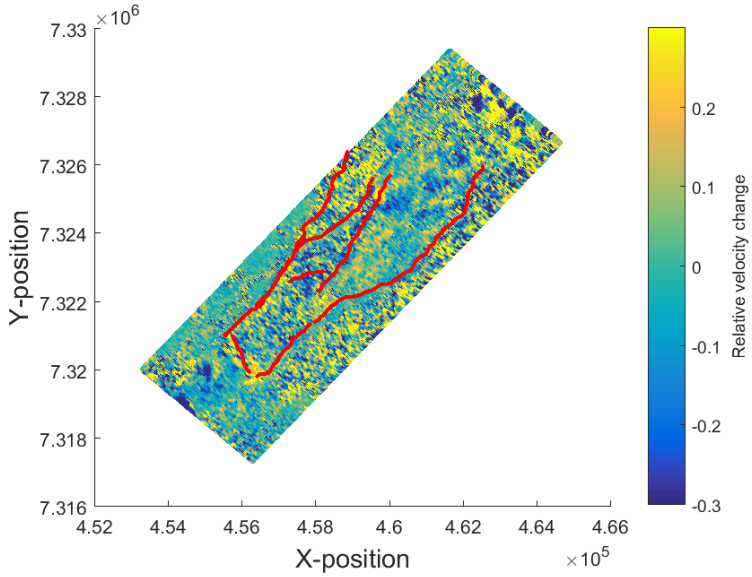

Figure A.18: Relative velocity changes from the top of the Garn formation down to top of the Not formation, i.e. through the Garn formation, using Method 2.

A.3 Well Panels

As previously mentioned, the points in Segments C, D and G represents the location of three exploration wells. The gamma-ray and P-wave velocity logs are available for these wells, thus the timeshifts, relative timeshifts, relative velocity change and vertical strain have been plotted together with the logs for comparison.

A.3.1 Well 6608/10-2

Figure A.19 shows the well panel corresponding to well 6608/10-2 where Method 2 have been used to calculate the timeshifts, relative timeshfits, relative velocity change and vertical strain.

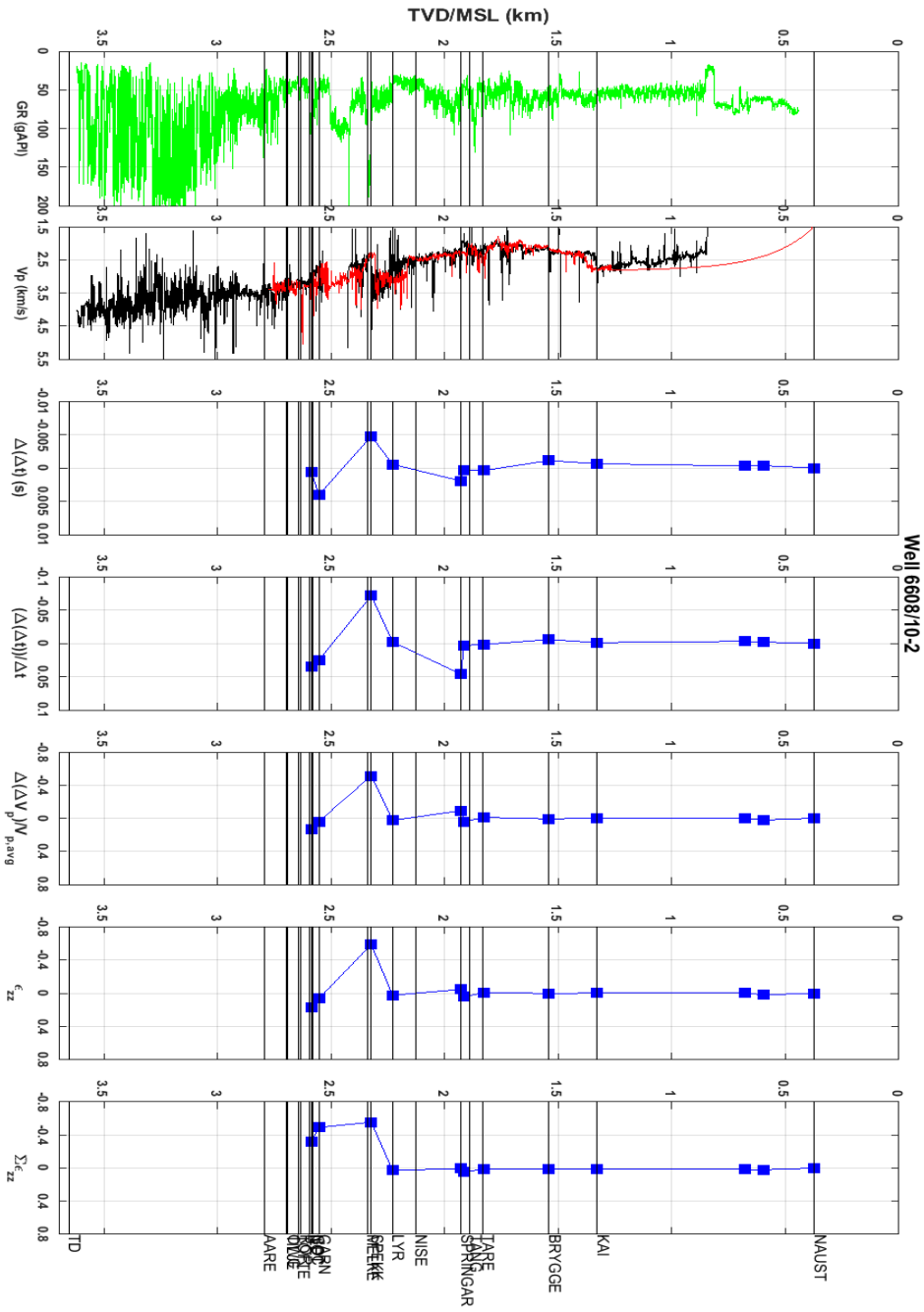

Figure A.19: Well panel showing gamma-ray log, P-wave velocity log, timeshifts, relative timeshifts, relative velocity change, calculated strain and accumulated calculated strain in well 6608/10-2, using Method 2.

The behaviour of the velocity log, timeshift-plot, relative timeshfit-plot, relative velocity change-plot and calculated strain-plot have been analyzed in order to see whether the speed-ups and slow-downs coincide, and are listed in table 4.3.

Interval	$V_p - log$	$\Delta(\Delta t)$	$\frac{\Delta(\Delta t)}{\Delta t}$	$\frac{\Delta(\Delta V_p)}{\bar{V}_p}$	ϵ_{zz}
Intra1 Naust	-	Speed-up	Speed-up	Speed-up	-
Intra2 Naust	-	Speed-up	Speed-up	-	Positive
Kai	Speed-up	Speed-up	Speed-up	-	Negative
Brygge	Slow-down	Speed-up	Speed-up	-	-
Intra Brygge	Slow-down	Slow-down	Slow-down	Slow-down	-
Intra Tare	Speed-up	Slow-down	Slow-down	Speed-up	Positive
Springar	Speed-up	Slow-down	Slow-down	Slow-down	Negative
Lyr	Speed-up	Speed-up	Speed-up	Speed-up	Positive
Spekk	Speed-up	Speed-up	Speed-up	Slow-down	Negative
Garn	Speed-up	Slow-down	Slow-down	Speed-up	Positive
Not	Speed-up	Speed-up	Speed-up	Speed-up	Positive

Table A.1: The velocity behaviour indicated by the timeshifts, relative timeshifts, relative velocity change, calculated strain and the accumulated calculated strain in well 6608/10-2, using Method 2.

The trend of the relative timeshift and relative velocity change plots can be further verified by figure A.20 where the mean of each relative timeshift and relative velocity change interval is plotted together with the actual values for both parameters.

When the mean of the relative timeshift is negative it indicates a speed-up while when the mean is positive it indicates a slow-down. When the mean of the relative velocity change is positive it indicates a speed-up, while when the mean is negative it indicates a slow-down.

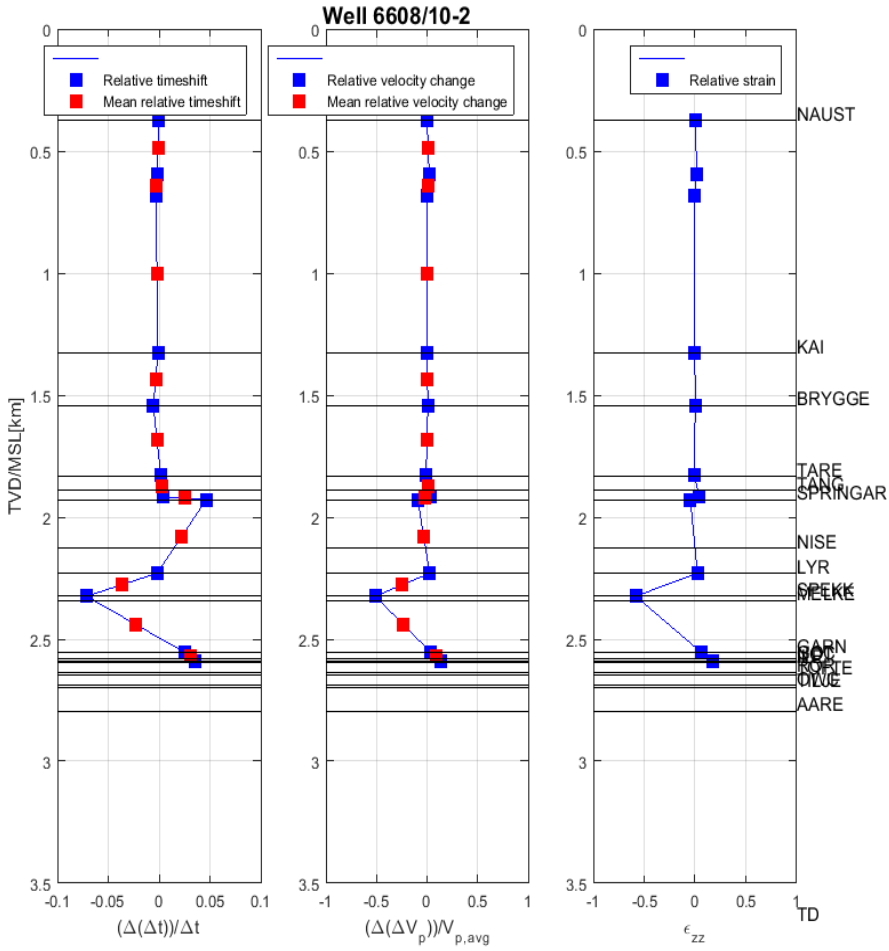

Figure A.20: Relative timeshifts and relative velocity change plotted together with the mean of the start- and end-point of each interval marked with red squares, vertical strain and R-factor for well 6608/10-2, using Method 2.

Table A.2 shows the calculated relative timeshifts, relative velocity changes and vertical strain in well 6608/10-2 using both Method 1 and Method 2.

When using Method 1, the magnitude of the calculated strains are realistic in the deeper intervals, i.e. from the seafloor down to the top of the Springar formation and down.

When using Method 2, the magnitude of the calculated strains are realistic in the shallow intervals, down to Intra Brygge. After that the magnitude of the calculated strain becomes unrealistically large.

Interval	**Method 1**			**Method 2**		
	$\frac{\Delta(\Delta t)}{\Delta t}$	$\frac{\Delta(\Delta V_p)}{\bar{V_p}}$	ϵ_{zz}	$\frac{\Delta(\Delta t)}{\Delta t}$	$\frac{\Delta(\Delta V_p)}{\bar{V_p}}$	ϵ_{zz}
Seafloor	0	0	0	0	0	0
Intra1 Naust	-0.185%	2.17%	1.98%	-0.185%	2.17%	1.98%
Intra2 Naust	-0.229%	1.37%	1.14%	- 0.308%	-0.21%	-0.52%
Kai	-0.148%	0.383%	0.236%	-0.108%	-0.091%	-0.2%
Brygge	-0.226%	0.473%	0.246%	-0.565%	0.86%	0.29%
Intra Brygge	-0.154%	-1.11%	-1.26%	0.155%	-0.98%	-0.83%
Intra Tare	-0.122%	0.388%	0.266%	0.35%	3.88%	4.23%
Springar	2.05E-02%	8.32E-02%	0.104%	4.65%	-9.2%	-4.56%
Lyr	-1.5E-02%	0.558%	0.543%	-0.201%	2.55%	2.35%
Spekk	-0.286%	-2.6E-02%	-0.312%	-7.14%	-51.19%	-58.33%
Garn	-5.0E-02%	0.288%	0.238%	2.54%	3.87%	6.41%
Not	-1.8E-02%	0.408%	0.390%	3.54%	13.48%	17.01%

Table A.2: Comparison of relative timeshifts, relative velocity change and calculated strain using Method 1 and Method 2 in well 6608/10-2.

A.3.2 Well 6608/10-3

Figure A.21 shows the well panel corresponding to well 6608/10-3 where Method 2 have been used to calculate the timeshifts, relative timeshfits, relative velocity change and vertical strain.

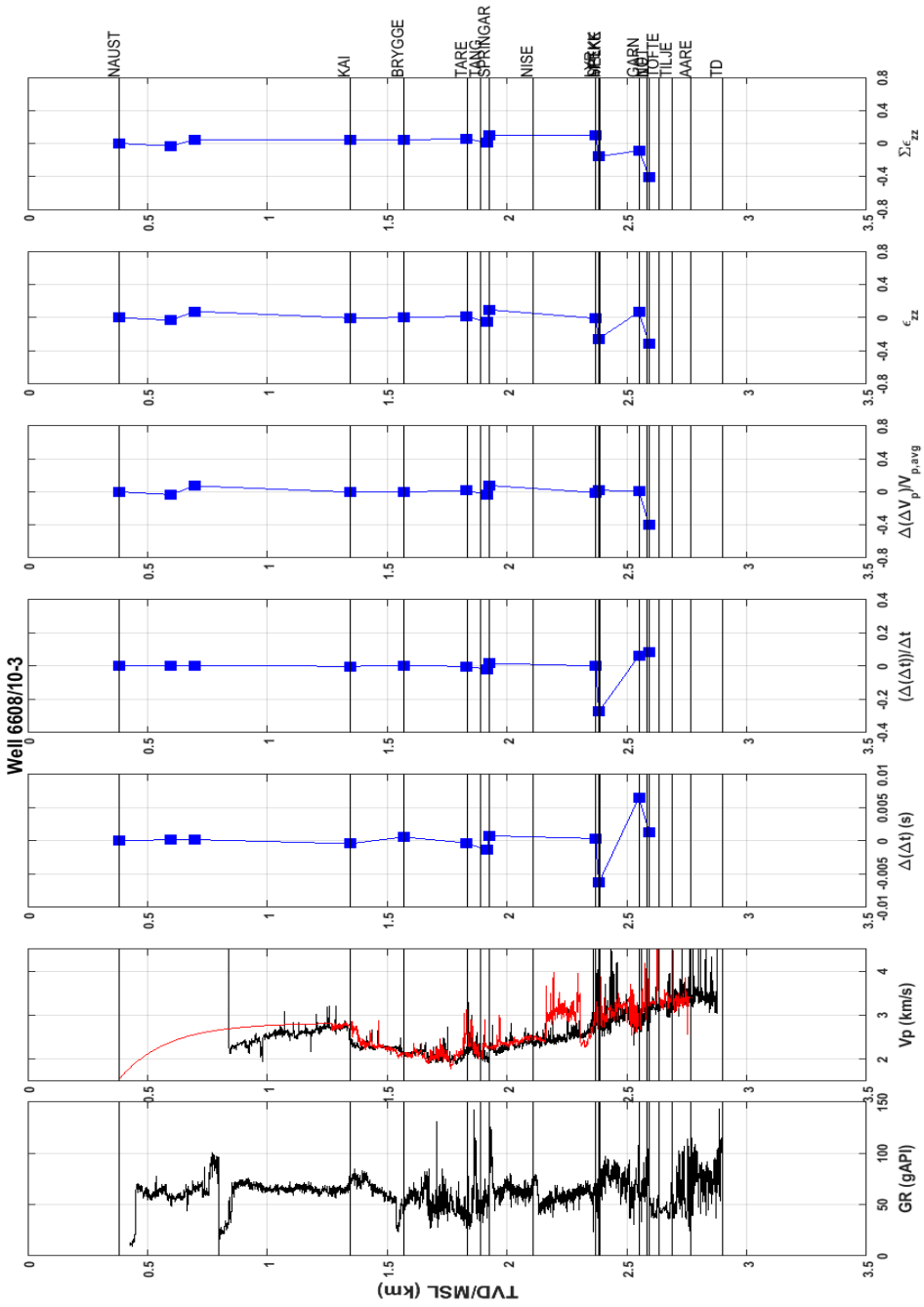

Figure A.21: Well panel showing gamma-ray log, P-wave velocity log, timeshifts, relative timeshifts, relative velocity change, calculated strain and accumulated calculated strain in well 6608/10-3, using Method 2.

The behaviour of the velocity log, timeshift-plot, relative timeshfit-plot, relative velocity change-plot and calculated strain-plot have been analyzed in order to see whether the speed-ups and slow-downs coincide, and are listed in table A.3.

Interval	$V_p - log$	$\Delta(\Delta t)$	$\frac{\Delta(\Delta t)}{\Delta t}$	$\frac{\Delta(\Delta V_p)}{\bar{V}_p}$	ϵ_{zz}
Intra1 Naust	-	-	-	Slow-down	Negative
Intra2 Naust	-	-	-	Speed-up	Positive
Kai	Speed-up	Speed-up	-	Slow-down	-
Brygge	Slow-down	Slow-down	-	-	-
Intra Brygge	Speed-up	Speed-up	-	-	-
Intra Tare	Speed-up	Speed-up	Speed-up	Slow-down	Negative
Springar	Speed-up	Slow-down	Slow-down	Speed-up	Positive
Lyr	Speed-up	Speed-up	Speed-up	Slow-down	Negative
Spekk	Speed-up	Speed-up	Speed-up	Speed-up	Negative
Garn	Speed-up	Slow-down	Slow-down	-	Positive
Not	Speed-up	Speed-up	Slow-down	Slow-down	Negative

Table A.3: The velocity behaviour indicated by the timeshifts, relative timeshifts, relative velocity change, calculated strain and the accumulated calculated strain in well 6608/10-3, using Method 2.

The trend of the relative timeshift and relative velocity change plots can be further verified by figure A.22 where the mean of each relative timeshift and relative velocity change interval is plotted together with the actual values for both parameters.

When the mean of the relative timeshift is negative it indicates a speed-up while when the mean is positive it indicates a slow-down. When the mean of the relative velocity change is positive it indicates a speed-up, while when the mean is negative it indicates a slow-down.

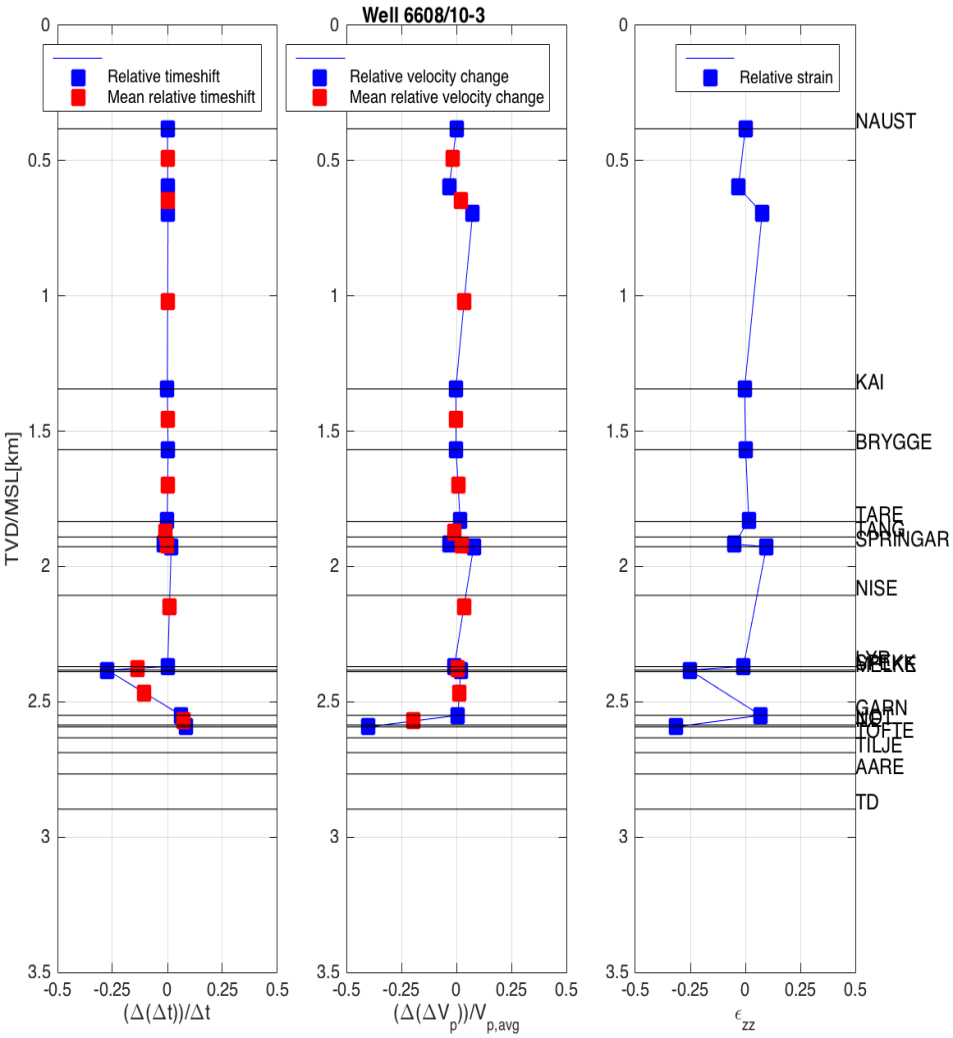

Figure A.22: Relative timeshifts and relative velocity change plotted together with the mean of the start- and end-point of each interval marked with red squares, vertical strain and R-factor for well 6608/10-3, using Method 2.

A.3.3 Well 6608/10-4

Figure 4.25 shows the well panel corresponding to well 6608/10-4 where Method 2 have been used to calculate the timeshifts, relative timeshfits, relative velocity change and vertical strain.

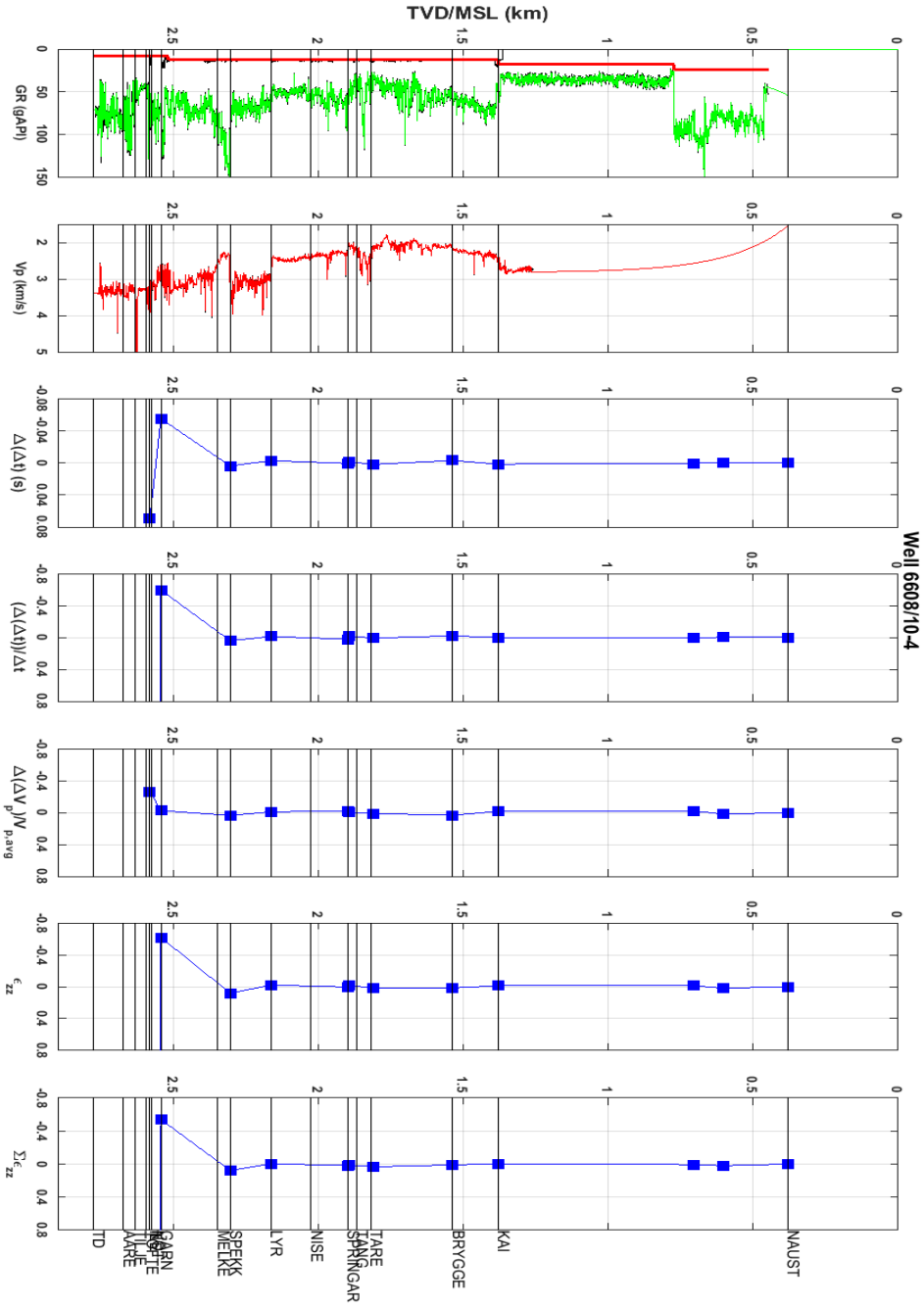

Figure A.23: Well panel showing gamma-ray log, P-wave velocity log, timeshifts, relative timeshifts, relative velocity change, calculated strain and accumulated calculated strain in well 6608/10-4, using Method 2.

The behaviour of the velocity log, timeshift-plot, relative timeshfit-plot, relative velocity change-plot and calculated strain-plot have been analyzed in order to see whether the speed-ups and slow-downs coincide, and are listed in table A.4.

Interval	$V_p - log$	$\Delta(\Delta t)$	$\frac{\Delta(\Delta t)}{\Delta t}$	$\frac{\Delta(\Delta V_p)}{\bar{V}_p}$	ϵ_{zz}
Intra1 Naust	-	-	-	-	-
Intra2 Naust	-	-	-	Slow-down	Negative
Kai	Speed-up	-	-	-	-
Brygge	Slow-down	Speed-up	Speed-up	Speed-up	Positive
Intra Brygge	Speed-up	Slow-down	Slow-down	Slow-down	-
Intra Tare	Slow-down	Speed-up	-	-	Negative
Springar	Slow-down	Slow-down	Slow-down	Slow-down	Positive
Lyr	Speed-up	Speed-up	Speed-up	Speed-up	Negative
Spekk	Speed-up	Slow-down	Slow-down	Speed-up	Positive
Garn	Speed-up	Speed-up	Speed-up	Slow-down	Negative
Not	Slow-down	Slow-down	Slow-down	Slow-down	Positive

Table A.4: The velocity behaviour indicated by the timeshifts, relative timeshifts, relative velocity change, calculated strain and the accumulated calculated strain in well 6608/10-4, using Method 2.

The trend of the relative timeshift and relative velocity change plots can be further verified by figure A.24 where the mean of each relative timeshift and relative velocity change interval is plotted together with the actual values for both parameters.

When the mean of the relative timeshift is negative it indicates a speed-up while when the mean is positive it indicates a slow-down. When the mean of the relative velocity change is positive it indicates a speed-up, while when the mean is negative it indicates a slow-down.

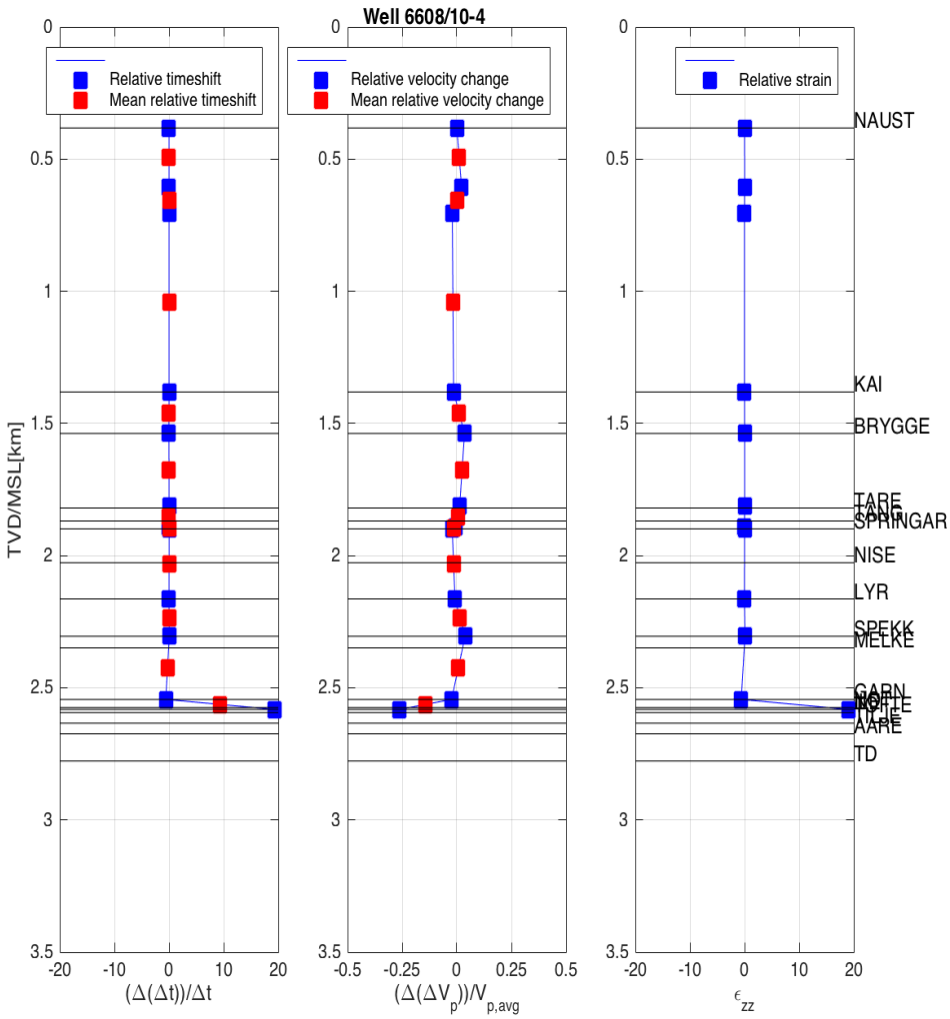

Figure A.24: Relative timeshifts and relative velocity change plotted together with the mean of the start- and end-point of each interval marked with red squares, vertical strain and R-factor for well 6608/10-4, using Method 2.

Appendix B

Timeshift Analysis for all Formation Tops

B.1 Method 1

B.1.1 Timeshifts

The following figures (B.1 - B.9) show the timeshifts from the seafloor down to every interpreted horizon, down to the top of the Spekk formation, where Method 1 have been used.

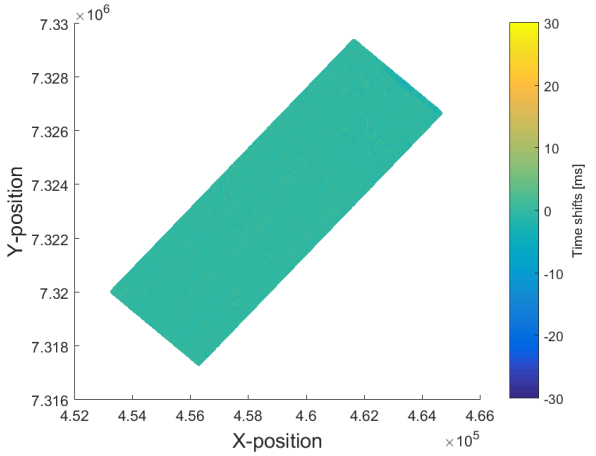

Figure B.1: Timeshifts from the seafloor down to Intra1 Naust formation, using Method 1.

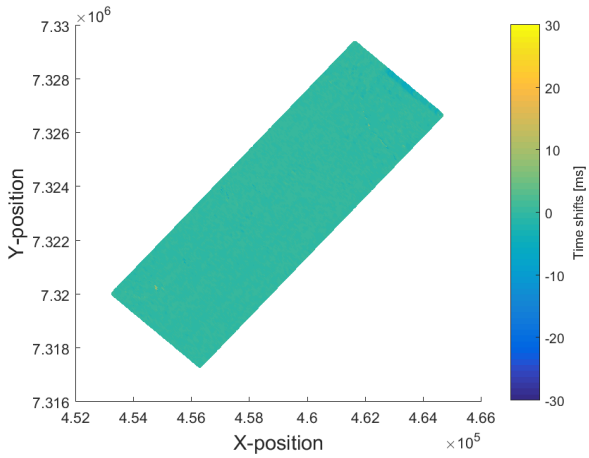

Figure B.2: Timeshifts from the seafloor down to Intra2 Naust formation, using Method 1.

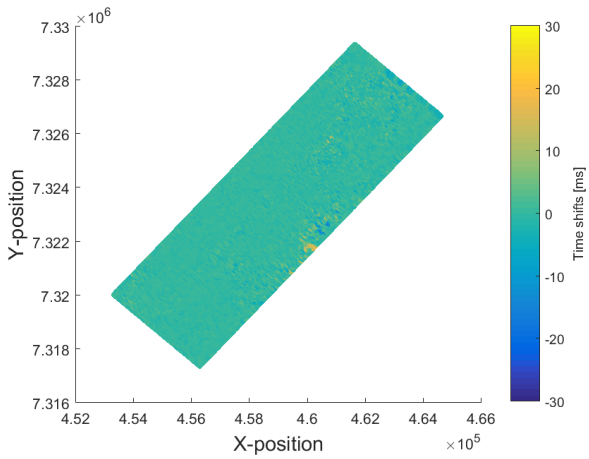

Figure B.3: Timeshifts from the seafloor down to top of Kai formation, using Method 1.

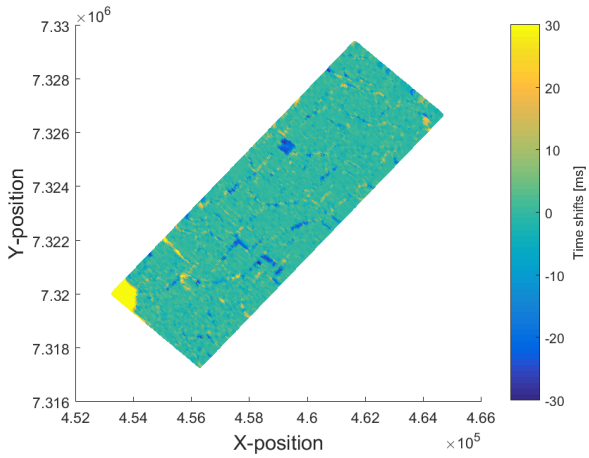

Figure B.4: Timeshifts from the seafloor down to top of Brygge formation, using Method 1.

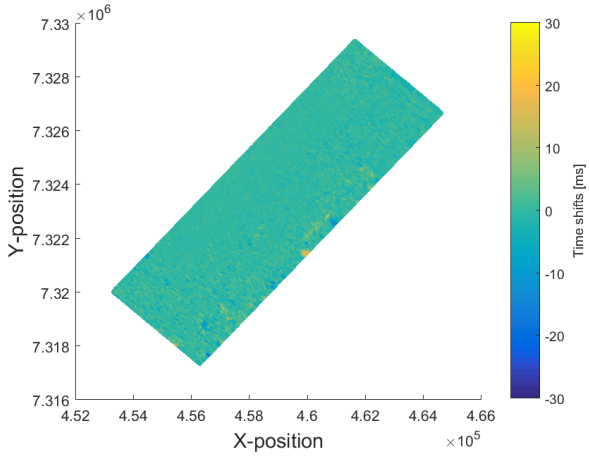

Figure B.5: Timeshifts from the seafloor down to top of Intra Brygge formation, using Method 1.

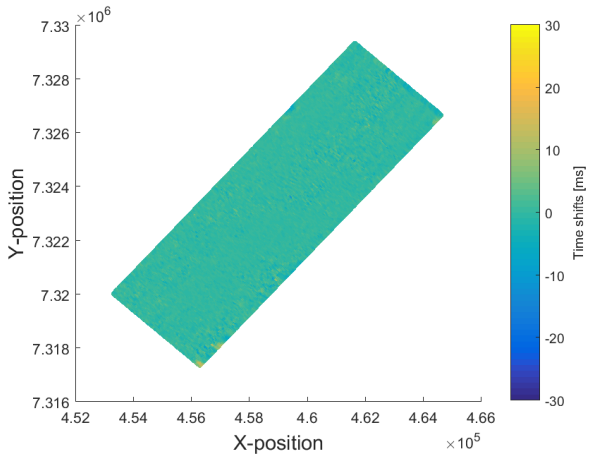

Figure B.6: Timeshifts from the seafloor down to top of Intra Tare formation, using Method 1.

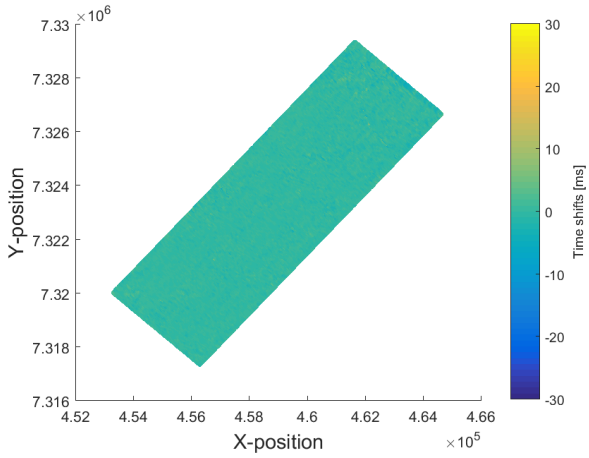

Figure B.7: Timeshifts from the seafloor down to top of Springar formation, using Method 1.

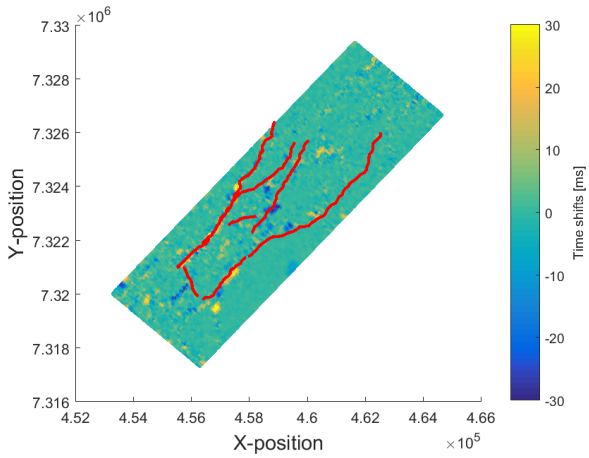

Figure B.8: Timeshifts from the seafloor down to top of Lyr formation, using Method 1.

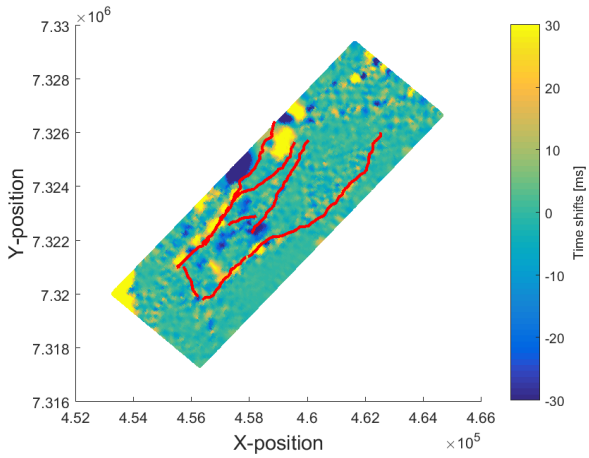

Figure B.9: Timeshifts from the seafloor down to top of the Spekk formation, using Method 1.

B.1.2 Relative Timeshifts

The following figures (B.10 - B.18) show the relative timeshifts from the seafloor down to every interpreted horizon, down to the top of the Spekk formation, where Method 1 have been used.

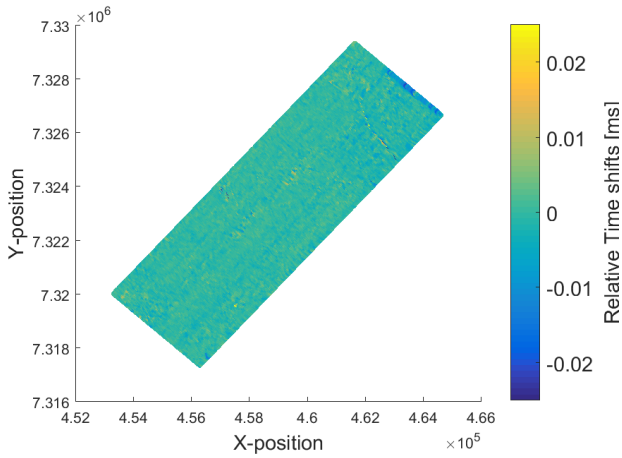

Figure B.10: Relative timeshifts from the seafloor down to top of the Intra1 Naust, using Method 1.

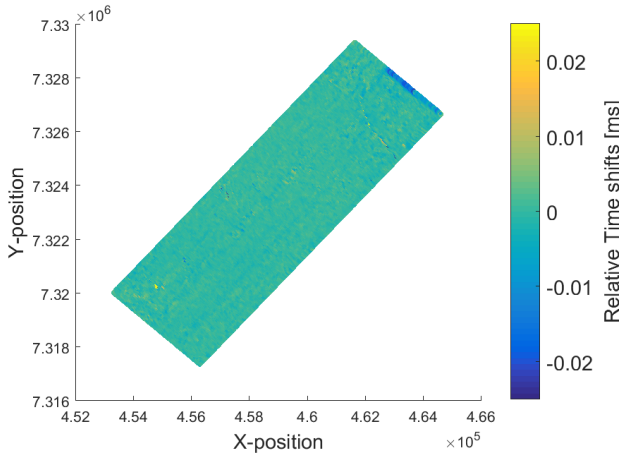

Figure B.11: Relative timeshifts from the seafloor down to top of the Intra2 Naust, using Method 1.

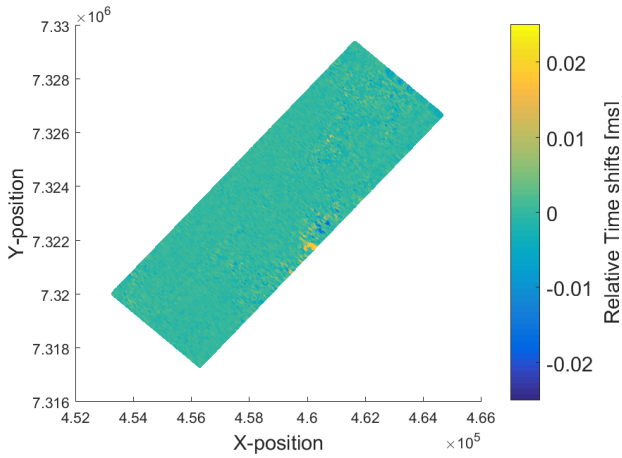

Figure B.12: Relative timeshifts from the seafloor down to top of the Kai formation, using Method 1.

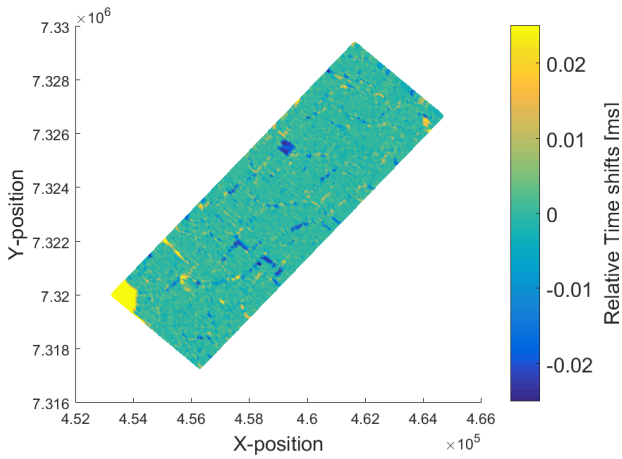

Figure B.13: Relative timeshifts from the seafloor down to top of the Brygge formation, using Method 1.

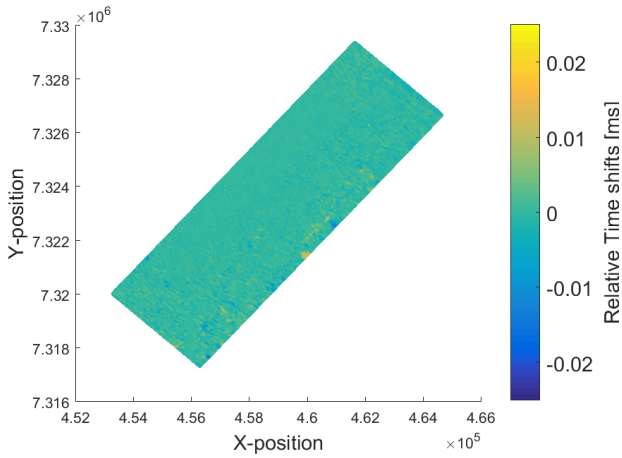

Figure B.14: Relative timeshifts from the seafloor down to top of the Intra Brygge formation, using Method 1.

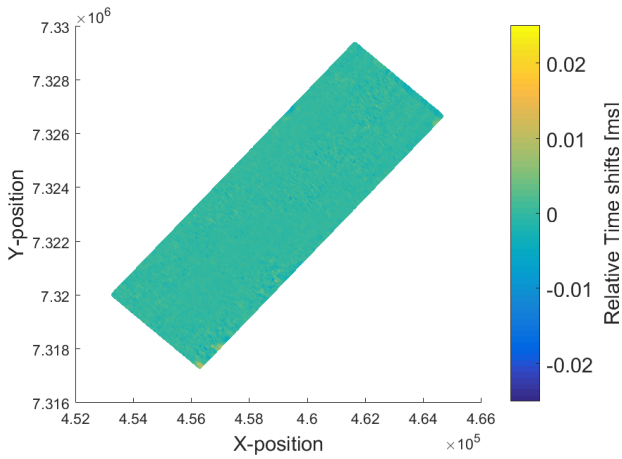

Figure B.15: Relative timeshifts from the seafloor down to top of the Intra Tare formation, using Method 1.

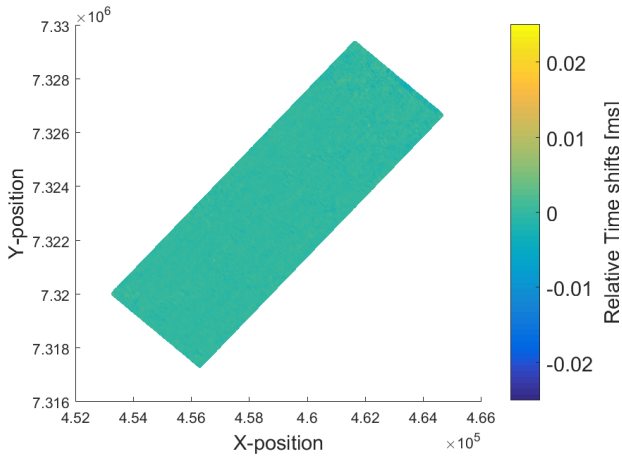

Figure B.16: Relative timeshifts from the seafloor down to top of the Springar formation, using Method 1.

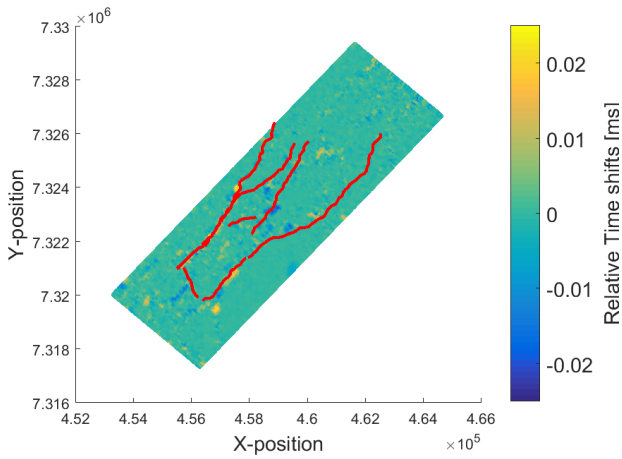

Figure B.17: Relative timeshifts from the seafloor down to top of the Lyr formation, using Method 1.

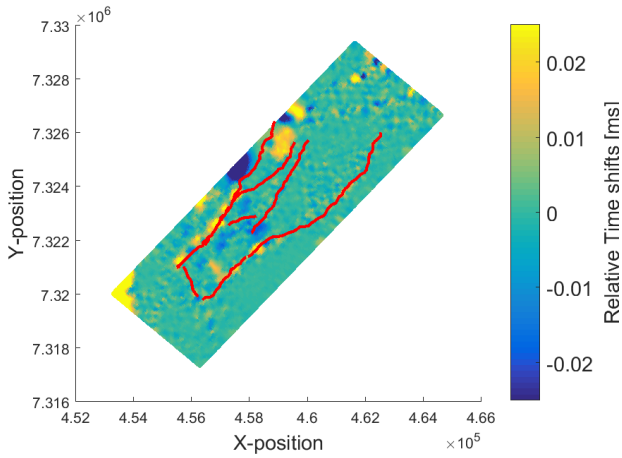

Figure B.18: Relative timeshifts from the seafloor down to top of the Spekk formation, using Method 1.

B.1.3 Relative Velocity Change

The following figures (B.19 - B.27) show the relative velocity change from the seafloor down to every interpreted horizon, down to the top of the Spekk formation, where Method 1 have been used.

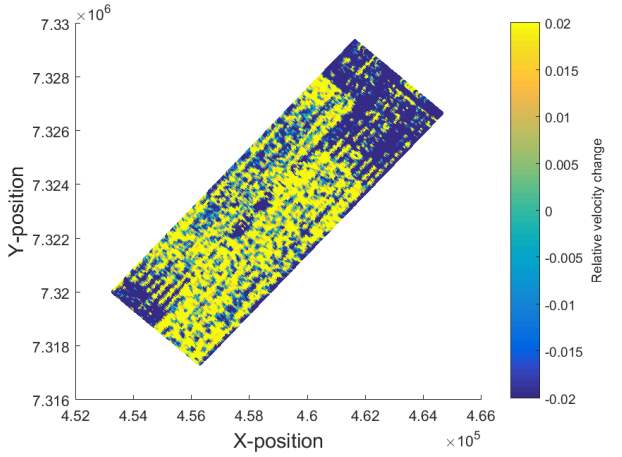

Figure B.19: Relative change in velocity from the seafloor down to top of Intra1 Naust, using Method 1.

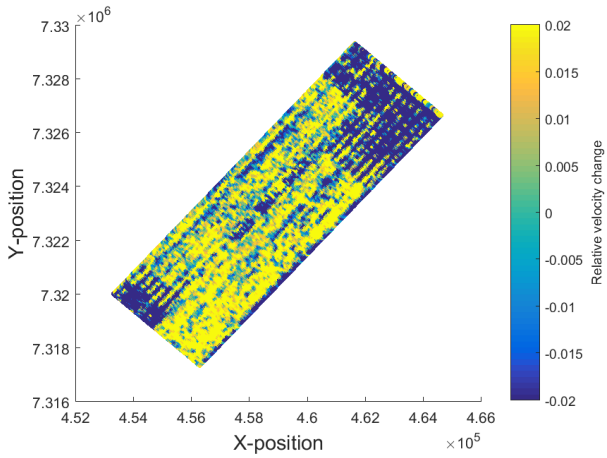

Figure B.20: Relative change in velocity from the seafloor down to top of Intra2 Naust, using Method 1.

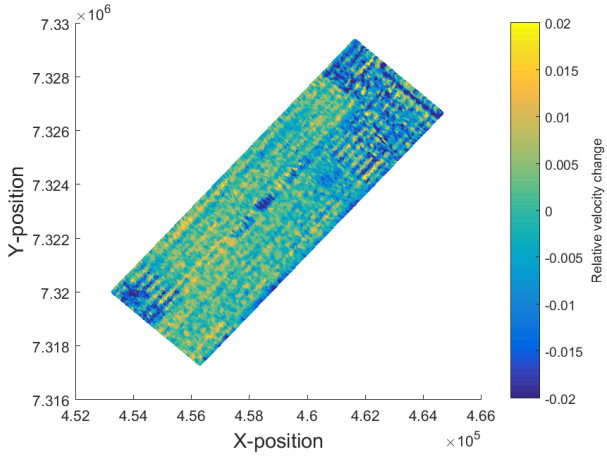

Figure B.21: Relative change in velocity from the seafloor down to top of the Kai formation, using Method 1.

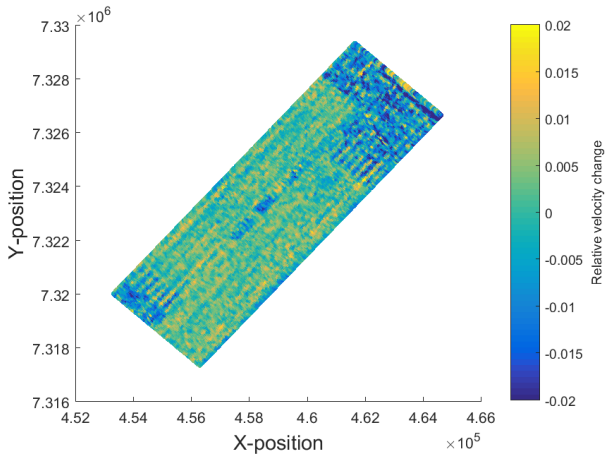

Figure B.22: Relative change in velocity from the seafloor down to top of the Brygge formation, using Method 1.

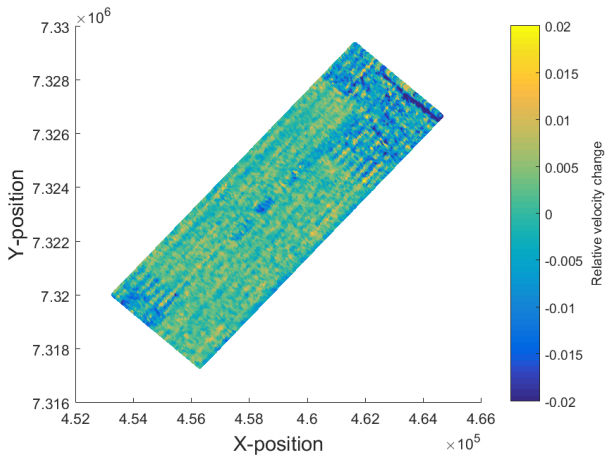

Figure B.23: Relative change in velocity from the seafloor down to top of the Intra Brygge formation, using Method 1.

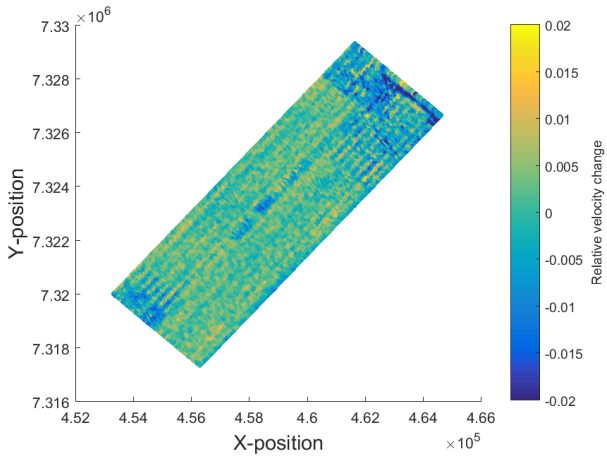

Figure B.24: Relative change in velocity from the seafloor down to top of the Intra Tare formation, using Method 1.

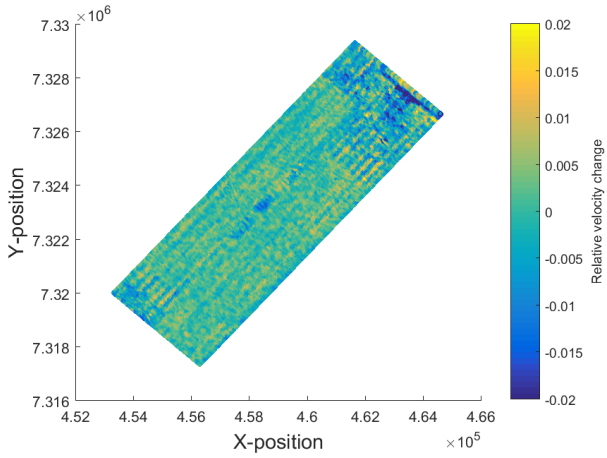

Figure B.25: Relative change in velocity from the seafloor down to top of the Springar formation, using Method 1.

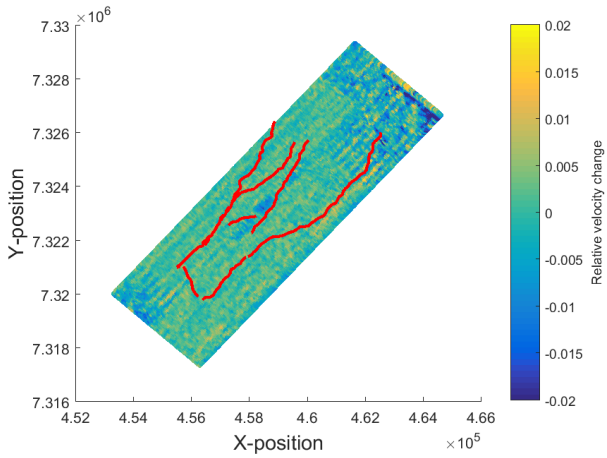

Figure B.26: Relative change in velocity from the seafloor down to top of the Lyr formation, using Method 1.

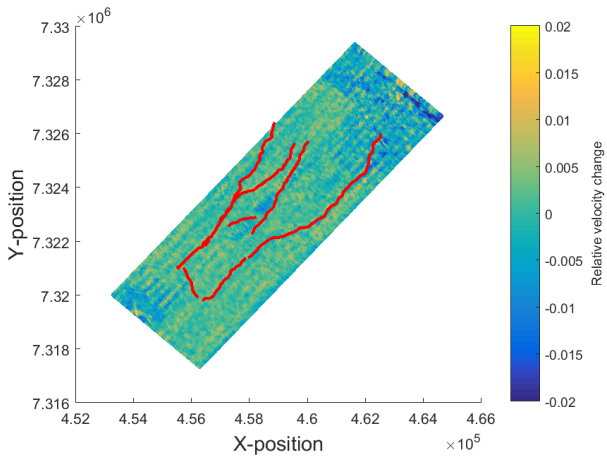

Figure B.27: Relative change in velocity from the seafloor down to top of the Spekk formation, using Method 1.

B.2 Method 2

B.2.1 Timeshifts

The following figures (B.28 - B.36) show the timeshifts in each interval, down to the top of the Spekk formation, where Method 2 have been used.

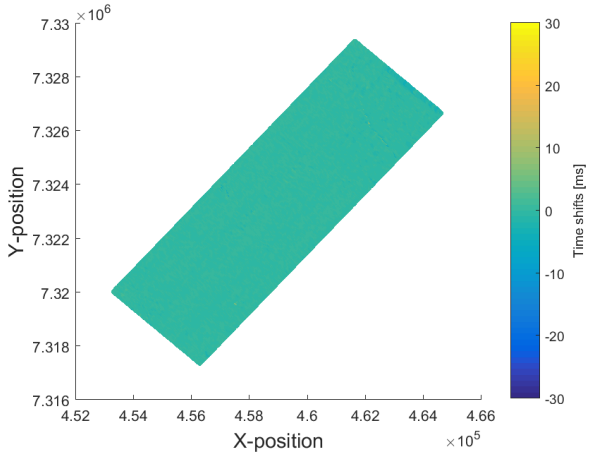

Figure B.28: Timeshifts from the seafloor down to top Intra1 Naust formation, using Method 2.

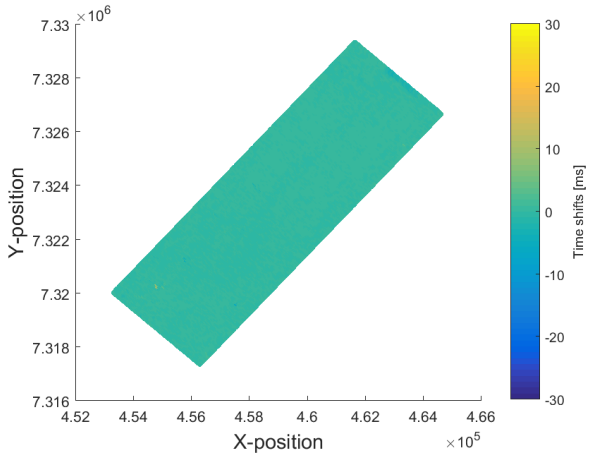

Figure B.29: Timeshifts from Intra1 Naust down to Intra2 Naust, using Method 2.

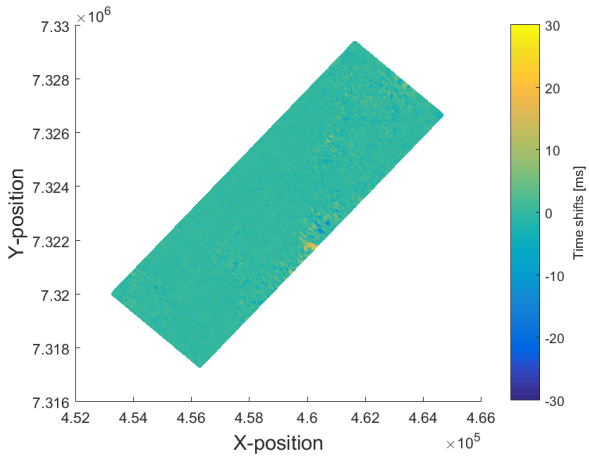

Figure B.30: Timeshifts from Intra2 Naust down to the top of the Kai, using Method 2.

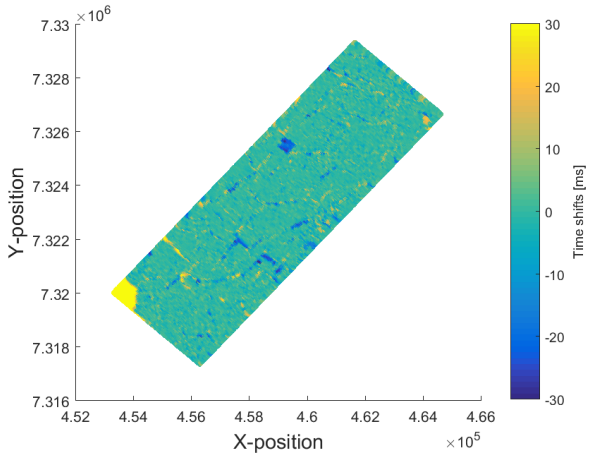

Figure B.31: Timeshifts from top of the Kai fomration down to top of the Brygge formation, i.e. the timeshifts through the Kai formation, using Method 2.

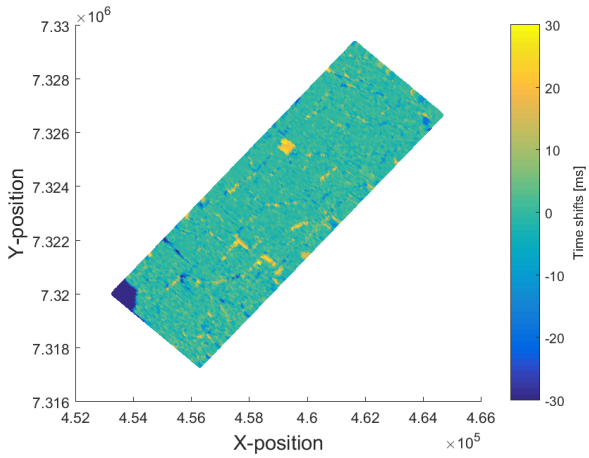

Figure B.32: Timeshifts from top of the Brygge fomration down Intra Brygge, i.e. the timeshifts through the upper part of the Brygge formation, using Method 2.

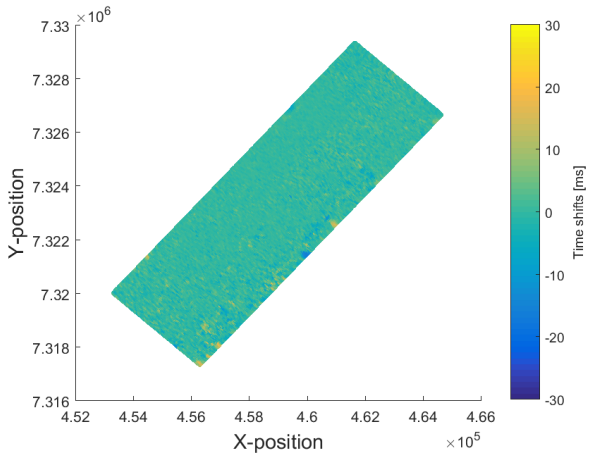

Figure B.33: Timeshifts from Intra Brygge formation down Intra Tare, i.e. the timeshifts through the lower part of the Brygge formation and the upper part of the Tare formation, using Method 2.

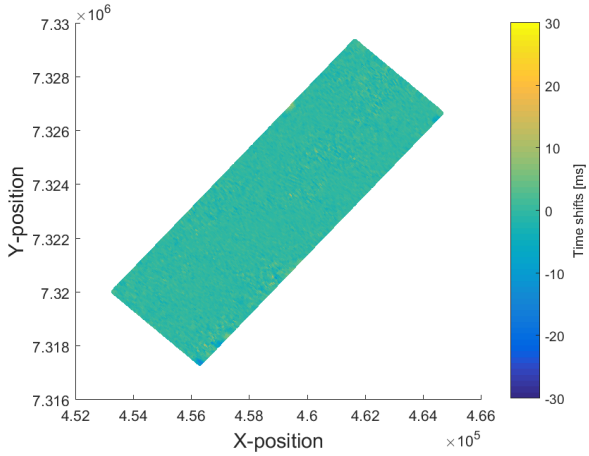

Figure B.34: Timeshifts from a reflector inside the Tare formation (Intra Tare) down to the top of the Springar formation, i.e. the timeshifts through the lower part of the Tare formation and the Tang formation, using Method 2.

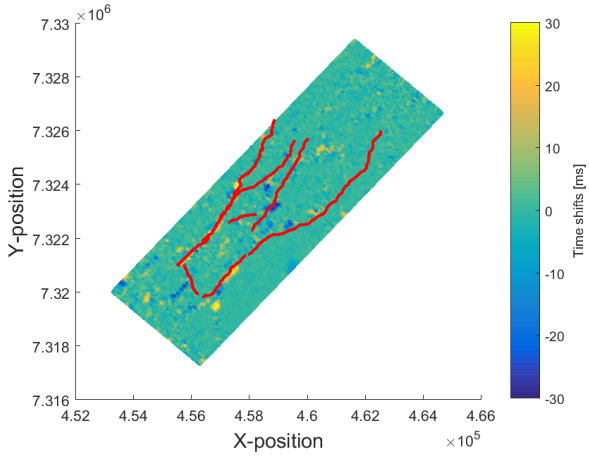

Figure B.35: Timeshifts from the top of the Springar formation down to top of the Lyr formation, i.e. the timeshifts through the Springar formation, using Method 2.

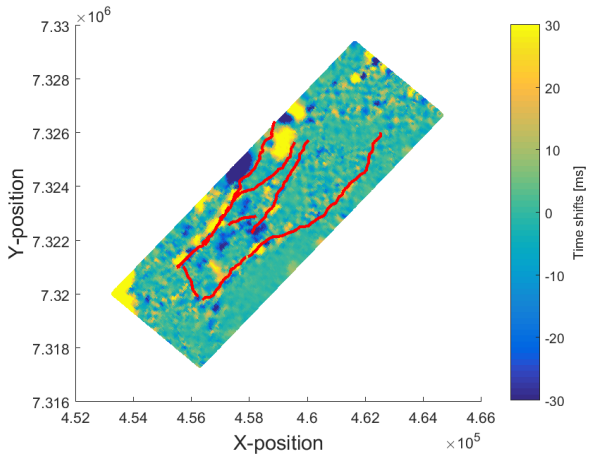

Figure B.36: Timeshifts from the top of the Lyr formation down to the top of the Spekk formation, i.e. the timeshifts through the Lyr formation, using Method 2.

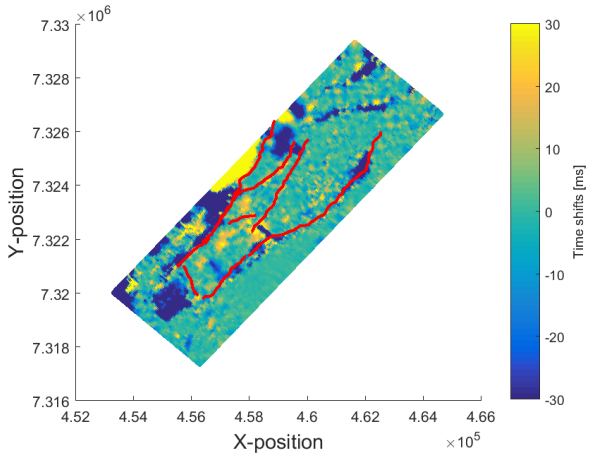

Figure B.37: Timeshifts from the top of the Spekk formation down to the top of the Garn formation, i.e. the timeshifts through the Spekk formation, using Method 2.

B.2.2 Relative Timeshifts

The following figures (B.38 - B.46) show the relative timeshifts in each interval, down to the top of the Spekk formation, where Method 2 have been used.

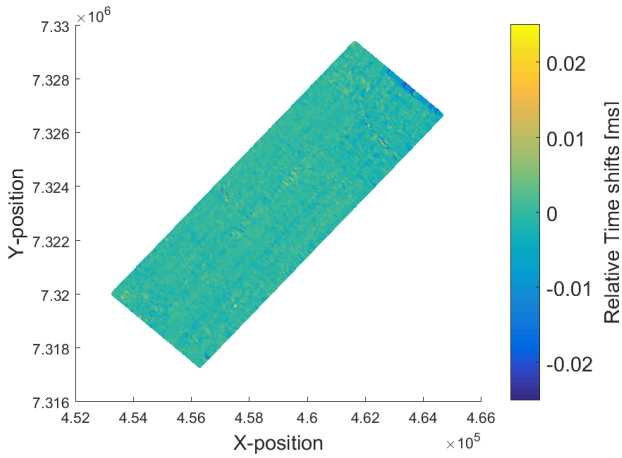

Figure B.38: Relative timeshifts from seafloor down to Intra1 Naust, i.e. the relative timeshfits through the upper most part of the Naust formation, using Method 2.

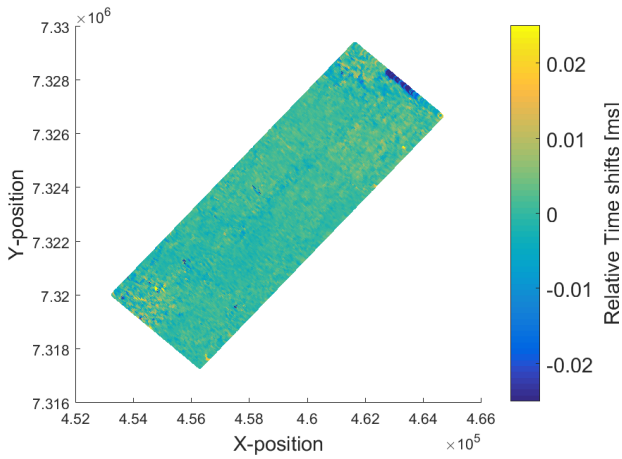

Figure B.39: Relative timeshifts from Intra1 Naust down to Intra2 Naust, i.e. the relative timeshifts through the middle part of the Naust formation, using Method 2.

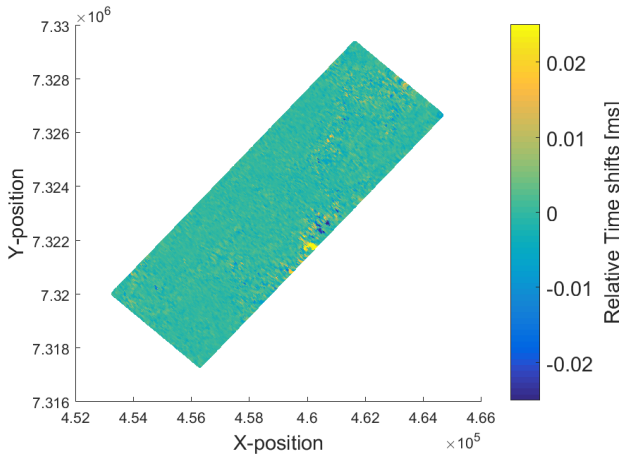

Figure B.40: Relative timeshifts from Intra2 Naust down to the top of the Kai formation, i.e. the relative timeshifts through the lower most part of the Naust formation, using Method 2.

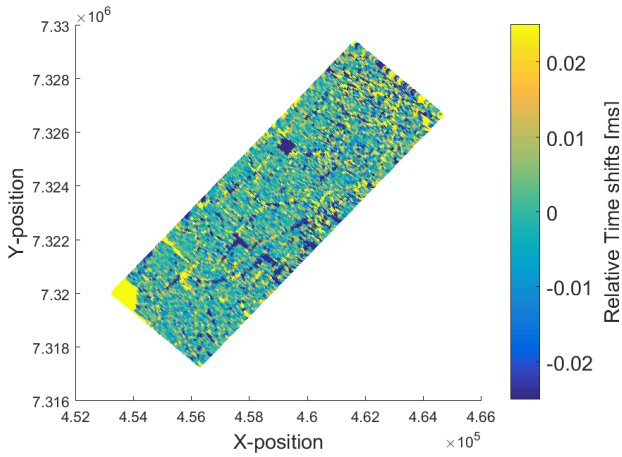

Figure B.41: Relative timeshifts from the top of the Kai formation down to the top of the Brygge formation, i.e. the relative timeshifts through the Kai formation, using Method 2.

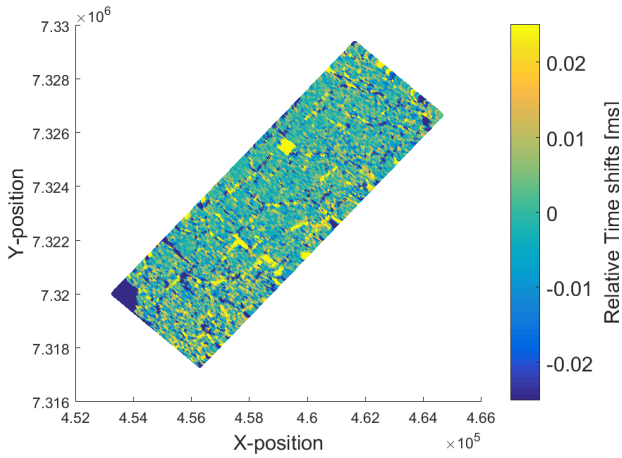

Figure B.42: Relative timeshifts from the top of the Brygge formation down to Intra Brygge, i.e. the relative timeshifts through the upper part of the Brygge formation, using Method 2.

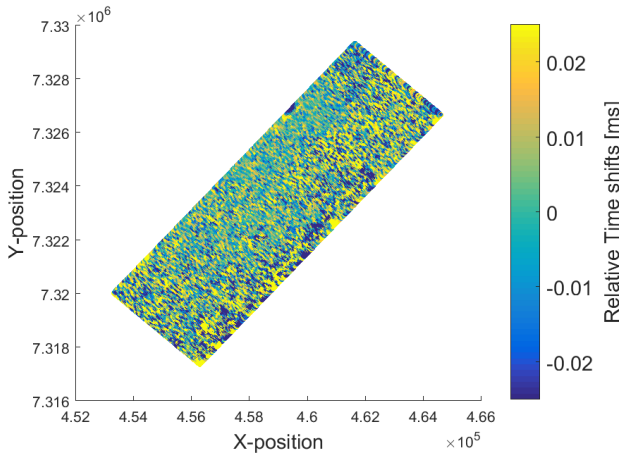

Figure B.43: Relative timeshifts from Intra Brygge down to Intra Tare, i.e. the relative timeshifts through the lower part of the Brygge formation and the upper part of the Tare formation, using Method 2.

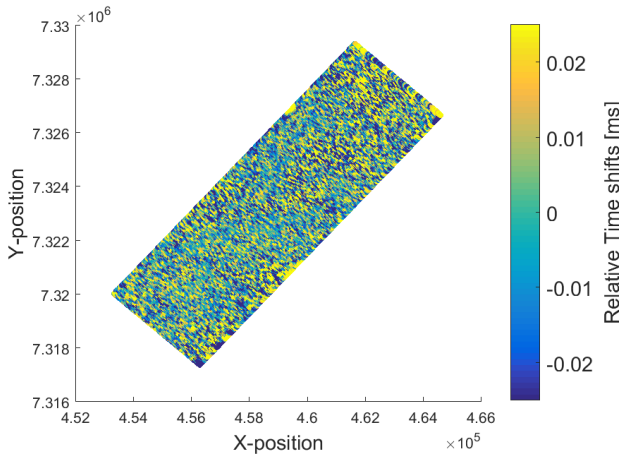

Figure B.44: Relative timeshifts from Intra Tare down to the top of the Springar formation, i.e. the relative timeshifts through the lower part of the Tare formation and the Tang formation, using Method 2.

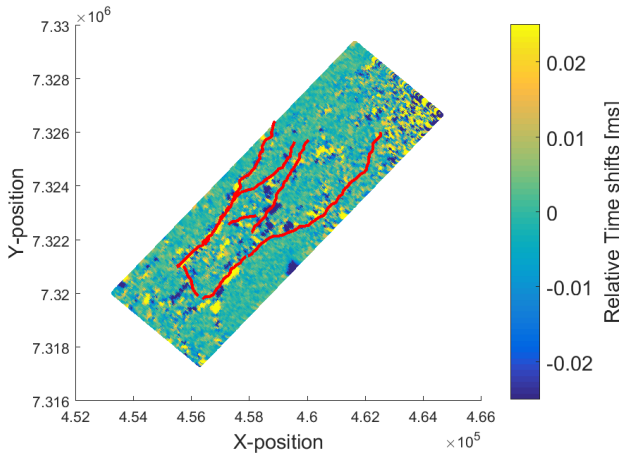

Figure B.45: Relative timeshifts from the top of the Springar formation down to the top of the Lyr formation, i.e. the relative timeshifts through the Springar formation, using Method 2.

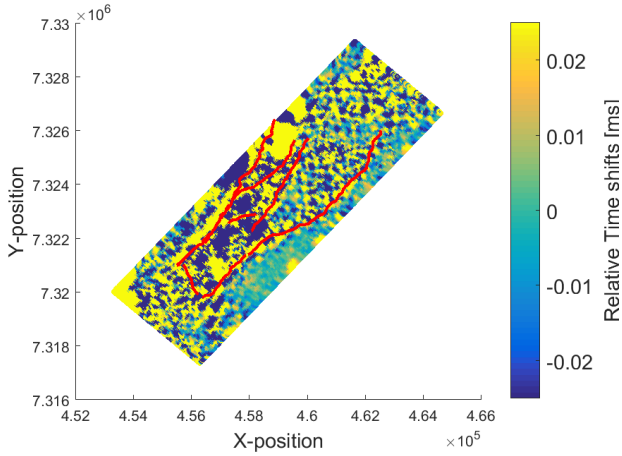

Figure B.46: Relative timeshifts from the top of the Lyr formation down to the top of the Spekk formation, i.e. the relative timeshifts through the Lyr formation, using Method 2.

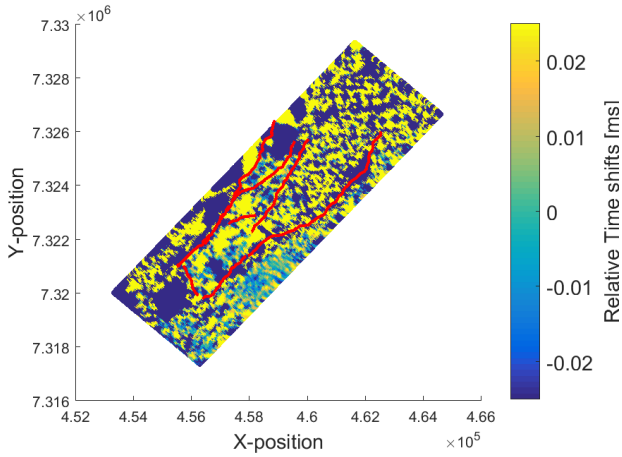

Figure B.47: Relative timeshifts from the top of the Spekk formation down to the top of the Garn formation, i.e. the relative timeshifts through the Spekk formation, using Method 2.

B.2.3 Relative Velocity change

The following figures (B.48 - B.56) show the relative velocity change in each interval, down to the top of the Spekk formation, where Method 2 have been used.

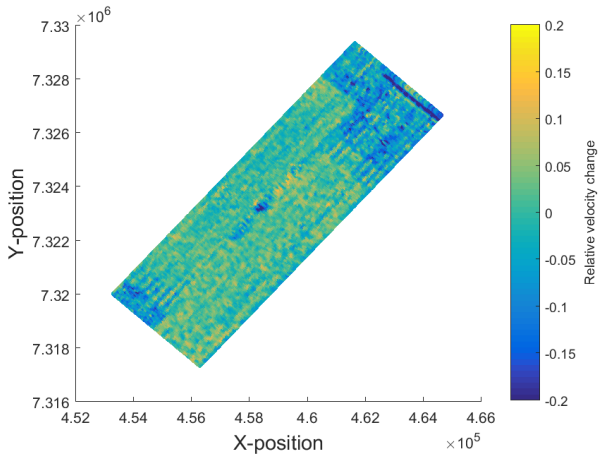

Figure B.48: Relative change in velocity from the seafloor down to Intra1 Naust, using Method 2.

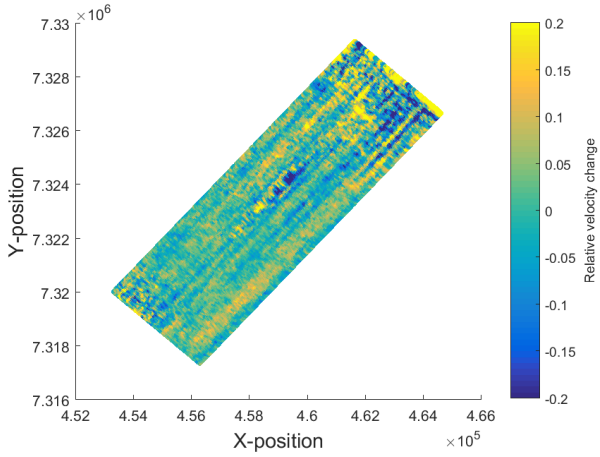

Figure B.49: Relative change in velocity from Intra1 Naust down to Intra2 Naust, using Method 2.

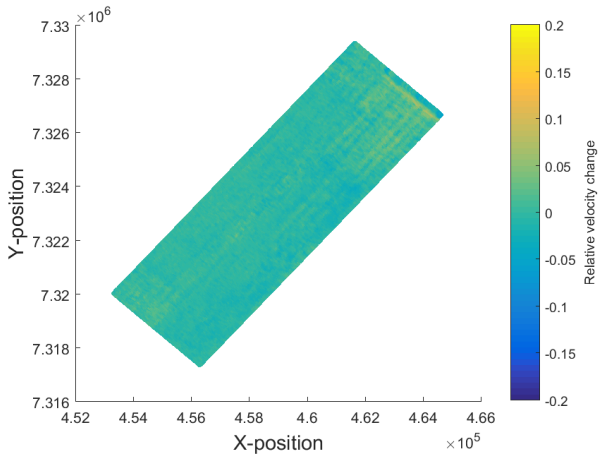

Figure B.50: Relative change in velocity from Intra2 Naust down to top of the Kai formation, using Method 2.

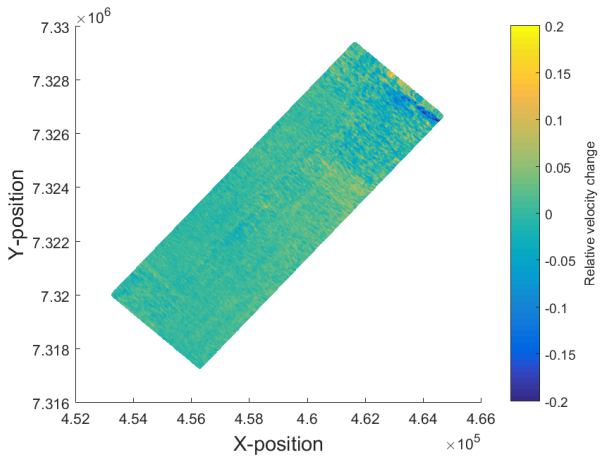

Figure B.51: Relative change in velocity from the top of the Kai formation down to top of the Brygge formation, using Method 2.

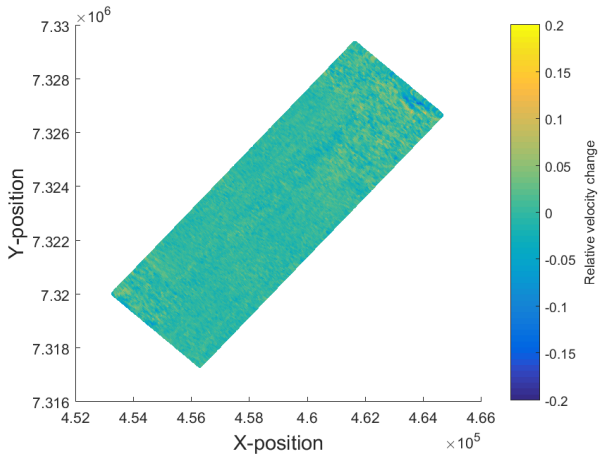

Figure B.52: Relative change in velocity from the top of the Brygge formation down to Intra Brygge, using Method 2.

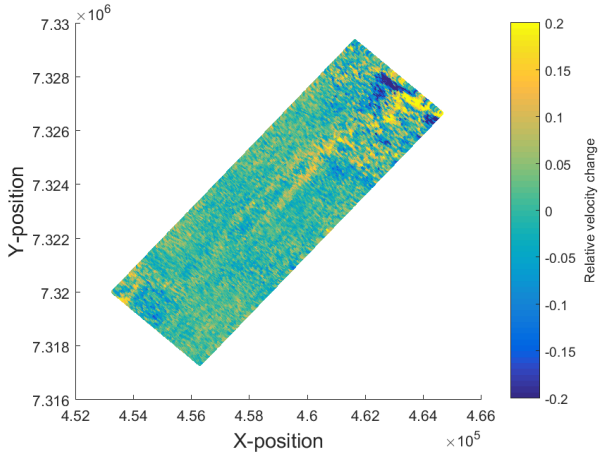

Figure B.53: Relative change in velocity from Intra Brygge down to Intra Tare, using Method 2.

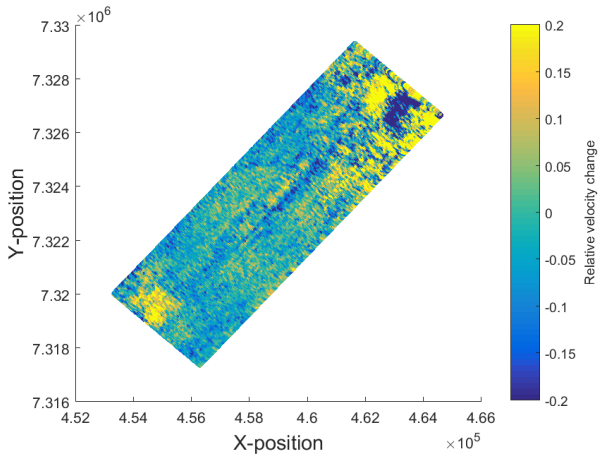

Figure B.54: Relative change in velocity from Intra Tare down to the top of the Springar formation, using Method 2.

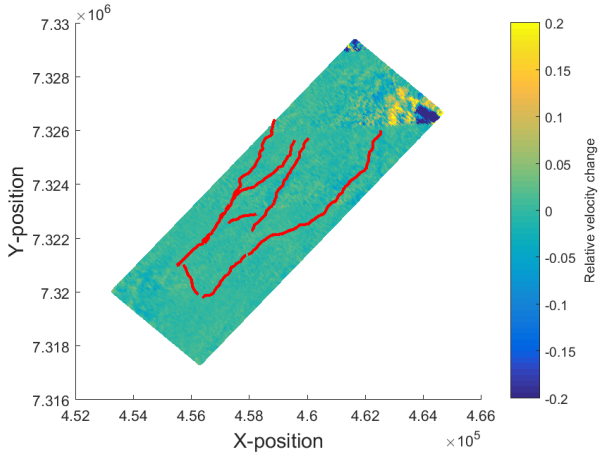

Figure B.55: Relative change in velocity from the top of the Springar formation down to the top of the Lyr formation, using Method 2.

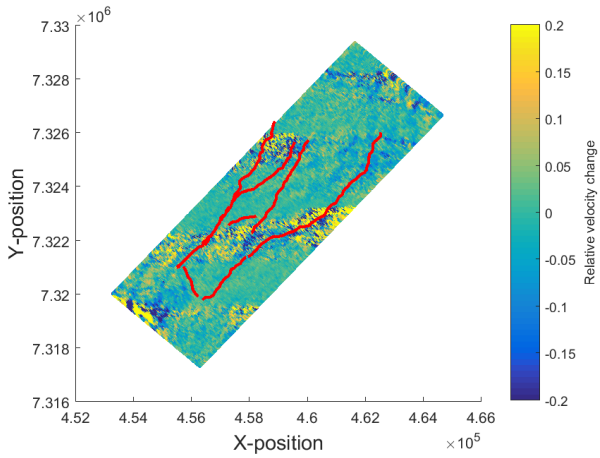

Figure B.56: Relative change in velocity from the top of the Lyr formation down to the top of the Spekk formation, using Method 2.

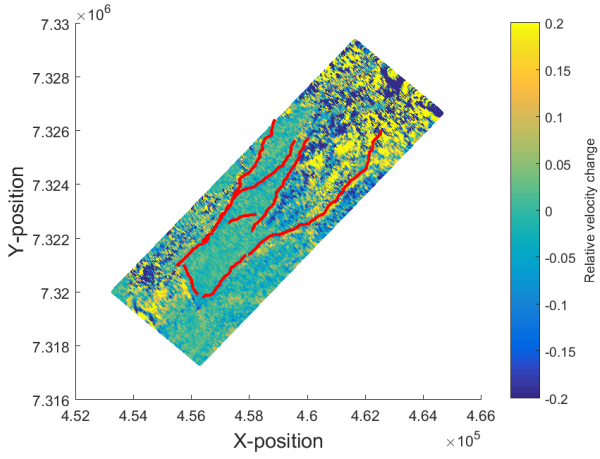

Figure B.57: Relative change in velocity from the top of the Spekk formation down to top of the Garn formation, using Method 2

B.3 Bar Plots

B.3.1 Method 2

.1 Accumulated Timeshifts The following figures (B.58 - B.61) show the accumulated timeshifts in each of the four analyzed locations, where Method 2 have been used. The figures are identical to figures 4.3, 4.6, 4.6 and 4.12 which shows the accumulated timeshifts using Method 2.

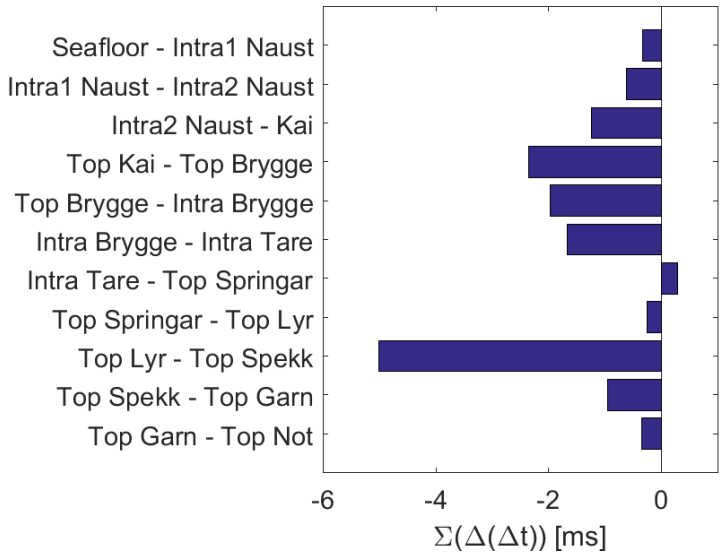

Figure B.58: Accumulated timeshifts from the seafloor down to each horizon in well 6608/10-2, using Method 2.

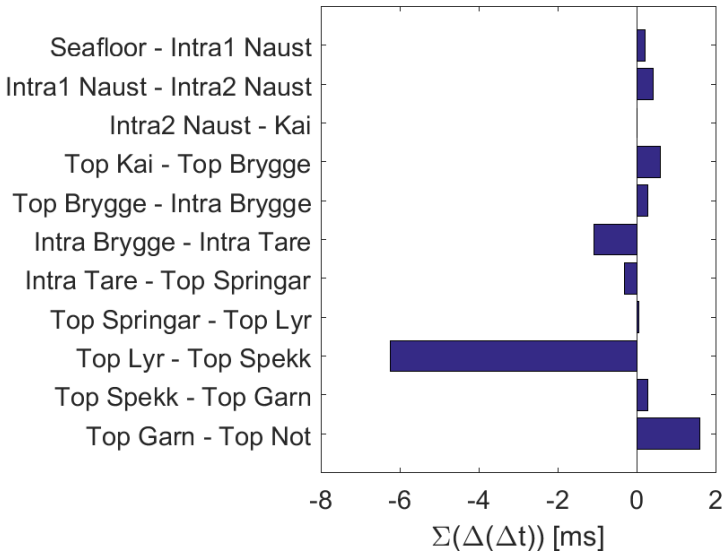

Figure B.59: Accumulated timeshifts from the seafloor down to each horizon in well 6608/10-3, using Method 2.

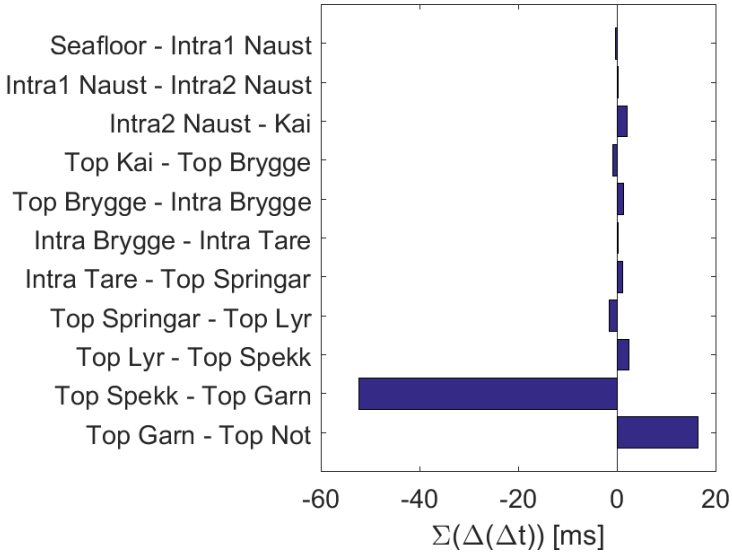

Figure B.60: Accumulated timeshifts from the seafloor down to each horizon in well 6608/10-4, using Method 2.

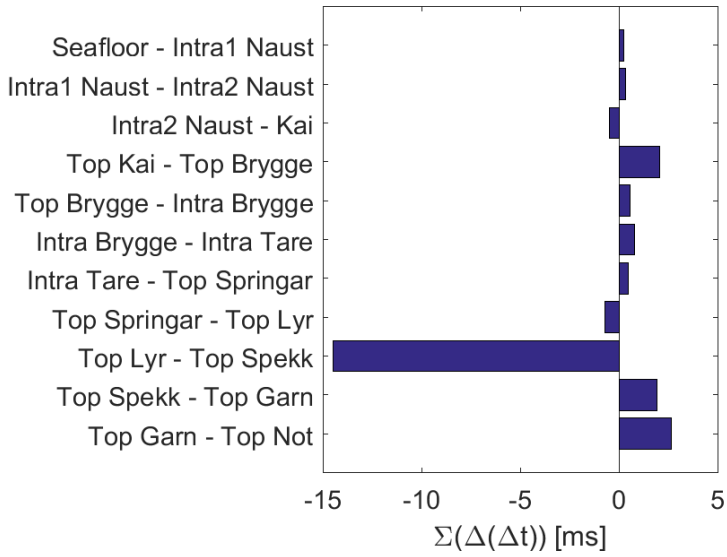

Figure B.61: Accumulated timeshifts from the seafloor down to each horizon in Segment D, using Method 2.

A Accumulated relative velocity change

The following figures (B.62 - B.65) show the accumulated relative velocity change in each of the four analyzed points, where Method 2 have been used. The figures are not identical to figures 4.5, 4.8, 4.8 and 4.14 which shows the accumulated relative velocity change using Method 2. This confirm the uncertainty related to the intercept-cube as the two methods of accumulating the relative velocity change does not yield the same result.

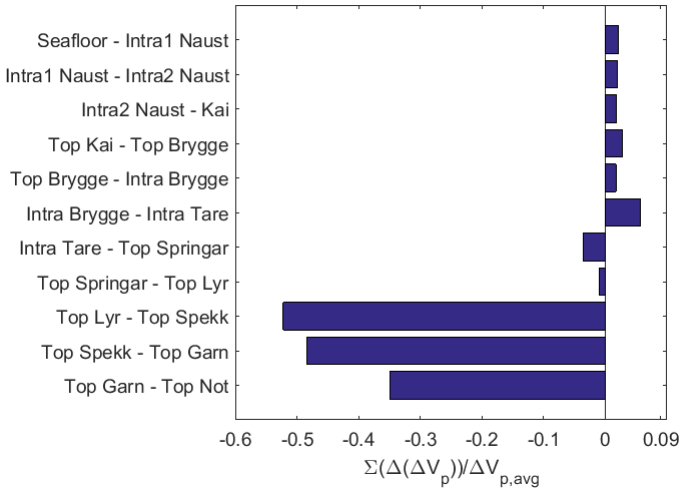

Figure B.62: Accumulated relative velocity change from the seafloor down to each horizon in well 6608/10-2, using Method 2.

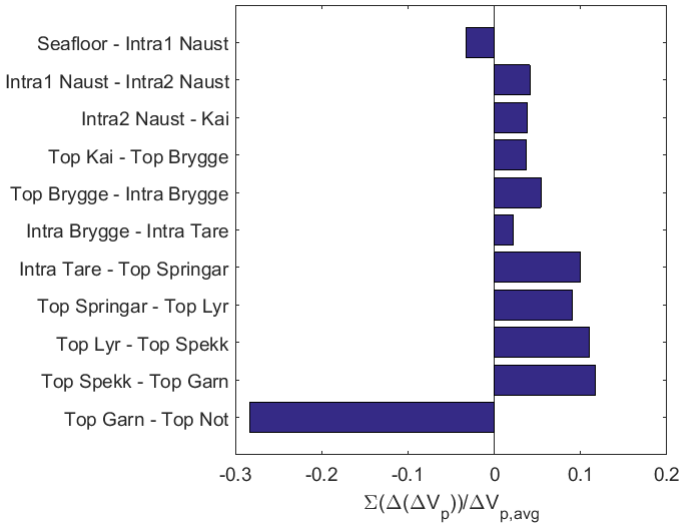

Figure B.63: Accumulated relative velocity change from the seafloor down to each horizon in well 6608/10-3, using Method 2.

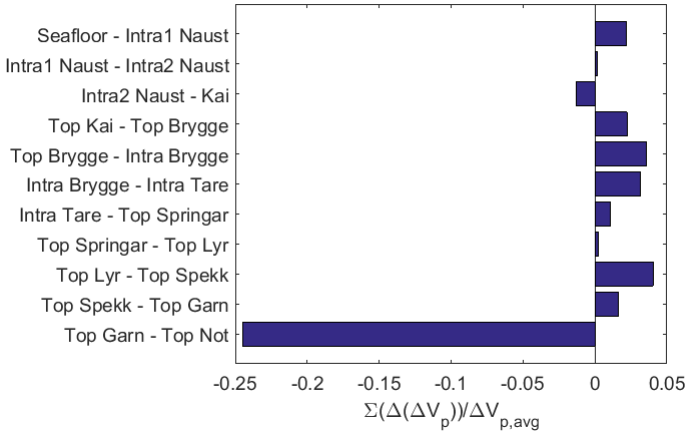

Figure B.64: Accumulated relative velocity change from the seafloor down to each horizon in well 6608/10-4, using Method 2.

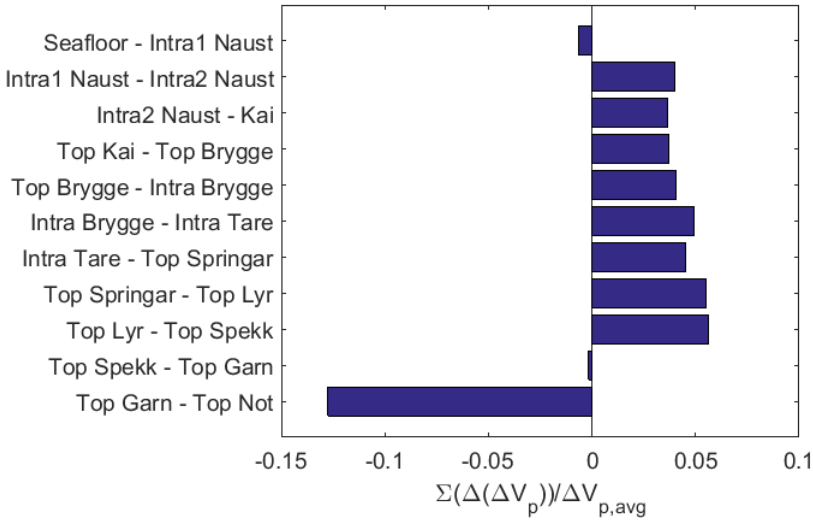

Figure B.65: Accumulated relative velocity change from the seafloor down to each horizon in Segment D, using Method 2.

Appendix C

Well Panels

C.1 Slope of each Interval

C.1.1 Well 6608/10-2

Figures C.1 and C.2 show the slope of the relative timeshifts and relative velocity changes in each interval in well 6608/10-2, using Method 1 and Method 2, respectively.

A Method 1

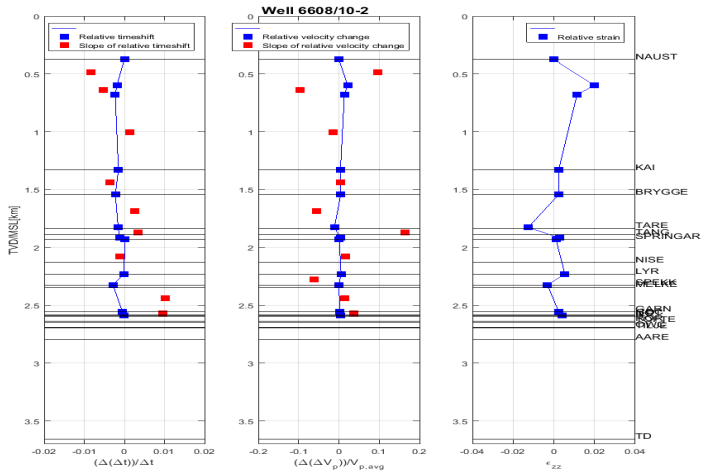

Figure C.1: The slope of the relative timeshifts and relative velocity change in well 6608/10-2, using Method 1.

B Method 2

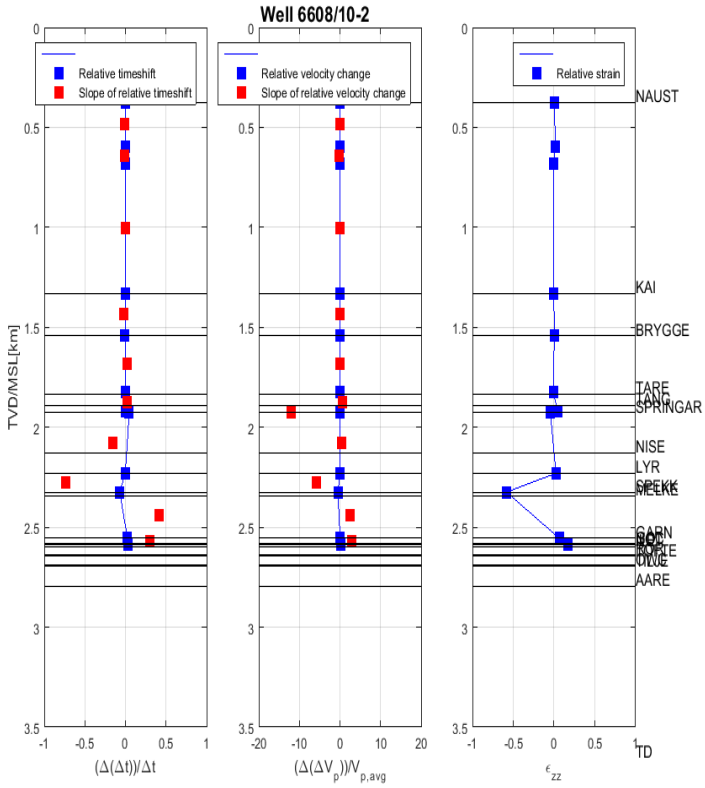

Figure C.2: The slope of the relative timeshifts and relative velocity change in well 6608/10-2, using Method 2.

C.1.2 Well 6608/10-3

Figures C.3 and C.4 show the slope of the relative timeshifts and relative velocity changes in each interval in well 6608/10-3, using Method 1 and Method 2, respectively.

A Method 1

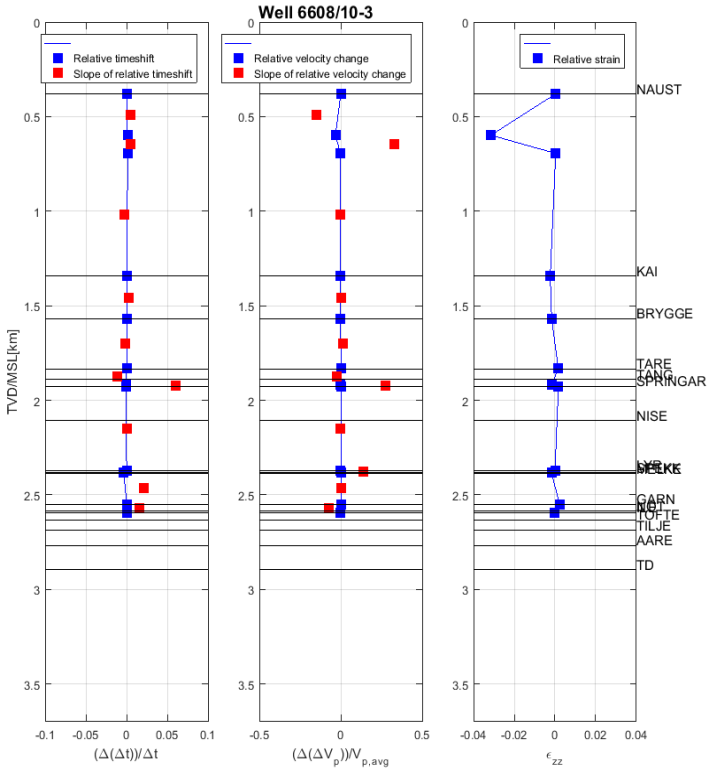

Figure C.3: The slope of the relative timeshifts and relative velocity change in well 6608/10-3, using Method 1.

B Method 2

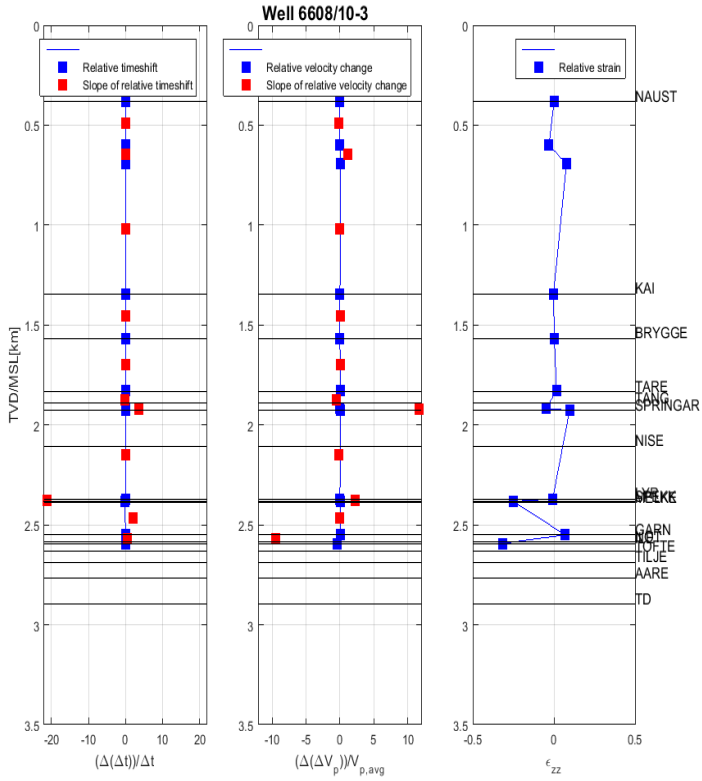

Figure C.4: The slope of the relative timeshifts and relative velocity change in well 6608/10-3, using Method 2.

C.1.3 Well 6608/10-4

Figures C.5 and C.6 show the slope of the relative timeshifts and relative velocity changes in each interval in well 6608/10-4, using Method 1 and Method 2, respectively.

A Method 1

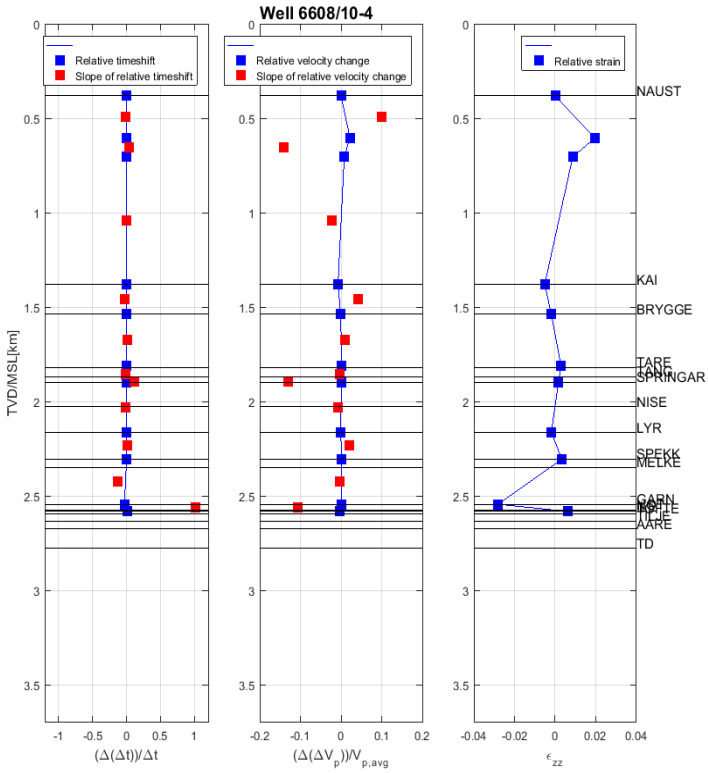

Figure C.5: The slope of the relative timeshifts and relative velocity change in well 6608/10-4, using Method 1.

B Method 2

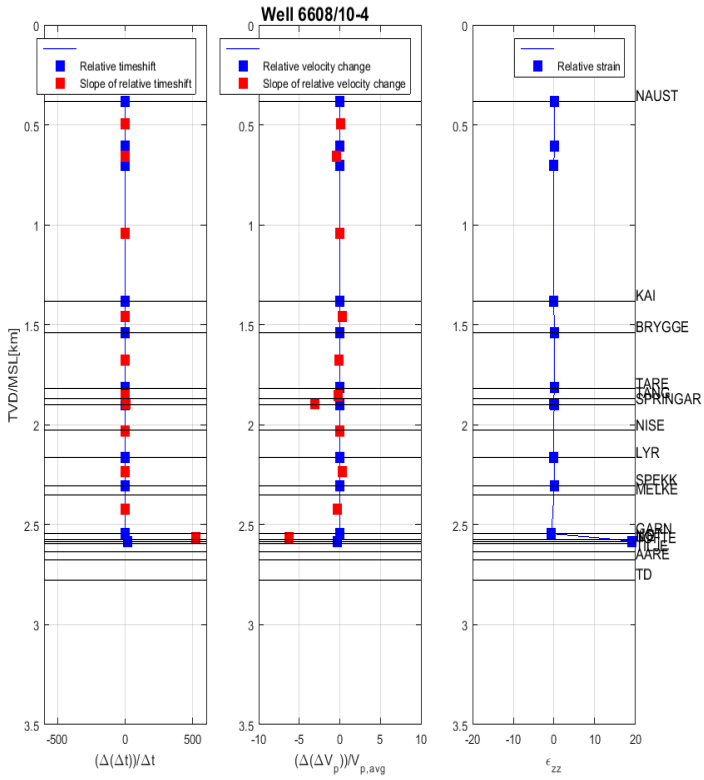

Figure C.6: The slope of the relative timeshifts and relative velocity change in well 6608/10-4, using Method 2.

C.2 R-factor

The R-factor express how sensitive a rock is to strain changes. As seen by the figures C.7-C.12 the strain sensitivity is very different in each formation.

C.2.1 Well 6608/10-2

Figures C.7 and C.8 show the relative velocity change, calculated strain and calculated R-factor in well 6608/10-2, using Method 1 and Method 2, respectively.

A Method 1

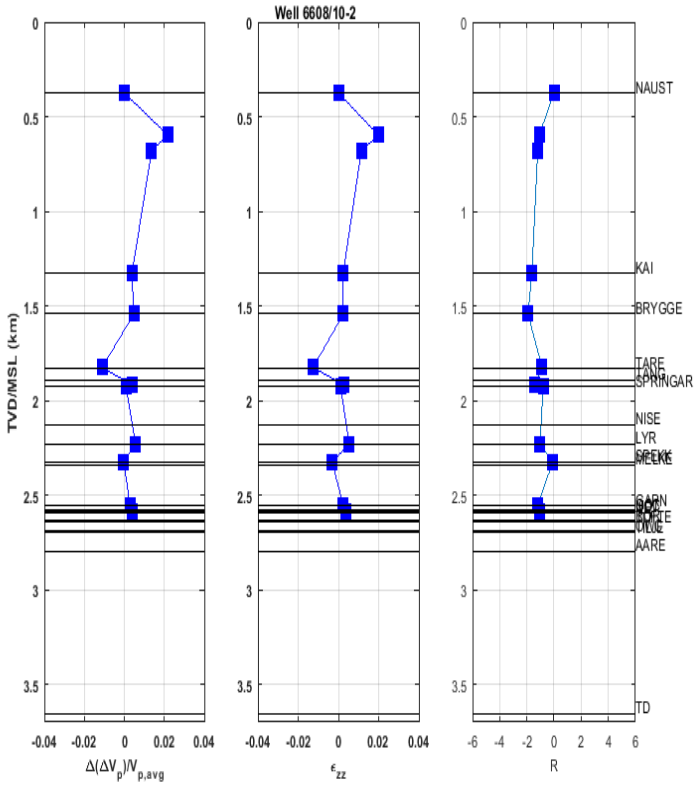

Figure C.7: The relative velocity change, strain and R-values versus depth in well 6608/10-2, using Method 1.

B Method 2

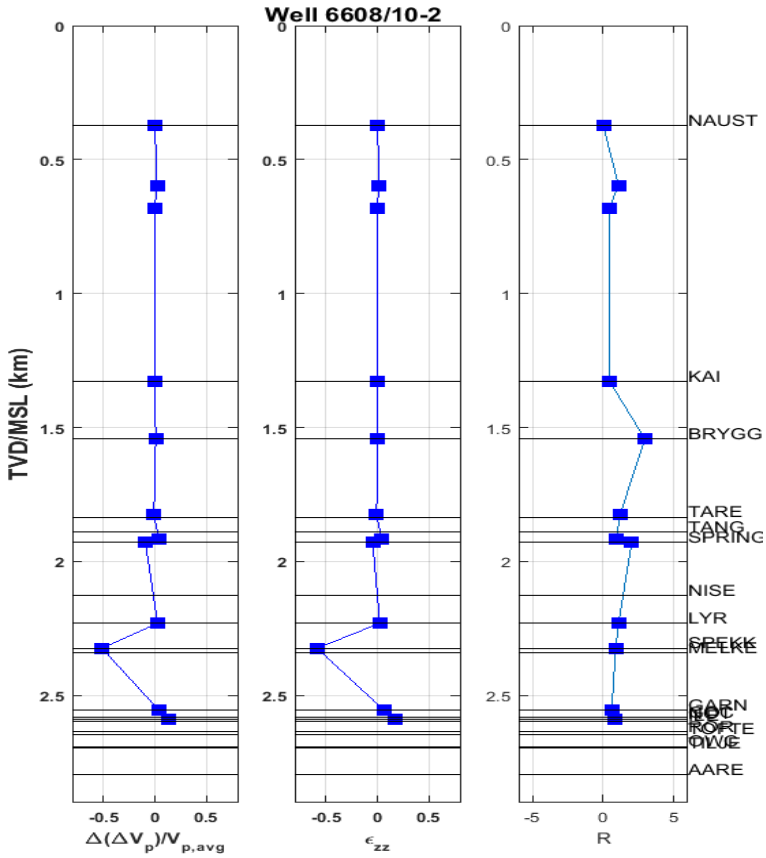

Figure C.8: The relative velocity change, strain and R-values versus depth in well 6608/10-2, using Method 2.

C.2.2 Well 6608/10-3

Figures C.9 and C.10 show the relative velocity change, calculated strain and calculated R-factor in well 6608/10-3, using Method 1 and Method 2, respectively.

A Method 1

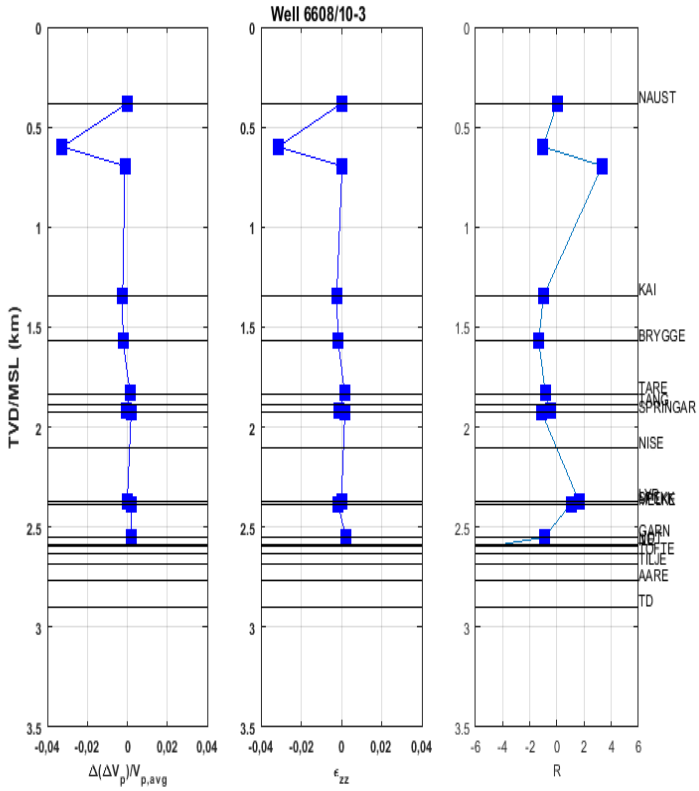

Figure C.9: The relative velocity change, strain and R-values versus depth in well 6608/10-3, using Method 1.

B Method 2

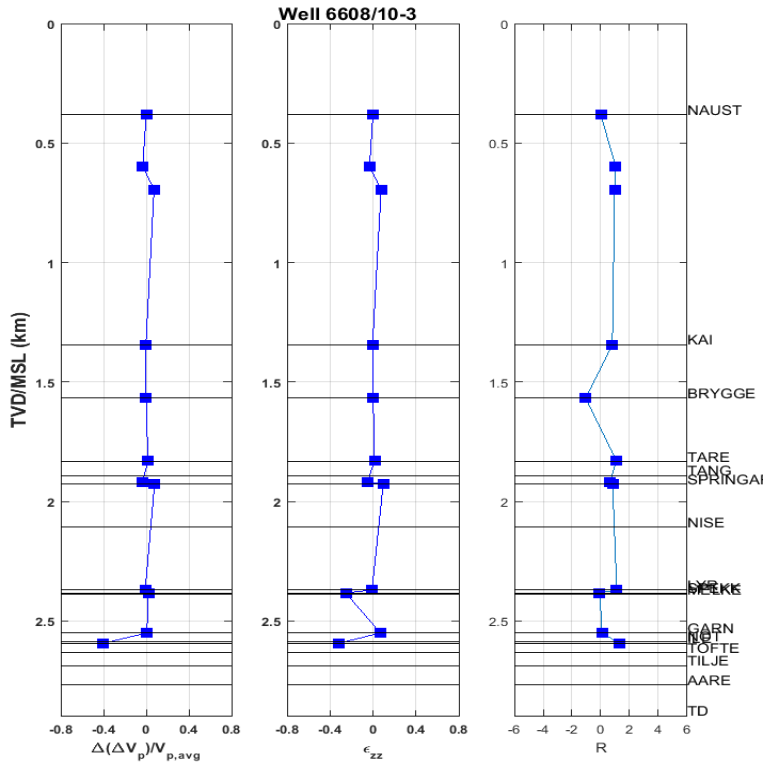

Figure C.10: The relative velocity change, strain and R-values versus depth in well 6608/10-3, using Method 2.

C.2.3 Well 6608/10-4

Figures C.11 and C.12 show the relative velocity change, calculated strain and calculated R-factor in well 6608/10-4, using Method 1 and Method 2, respectively.

A Method 1

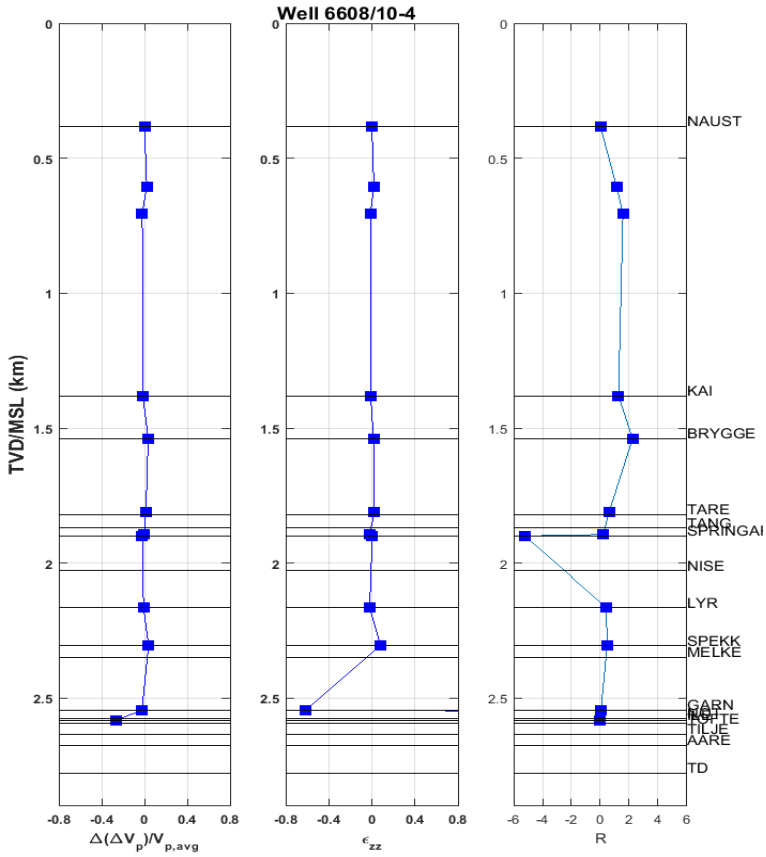

Figure C.11: The relative velocity change, strain and R-values versus depth in well 6608/10-4, using Method 1.

B Method 2

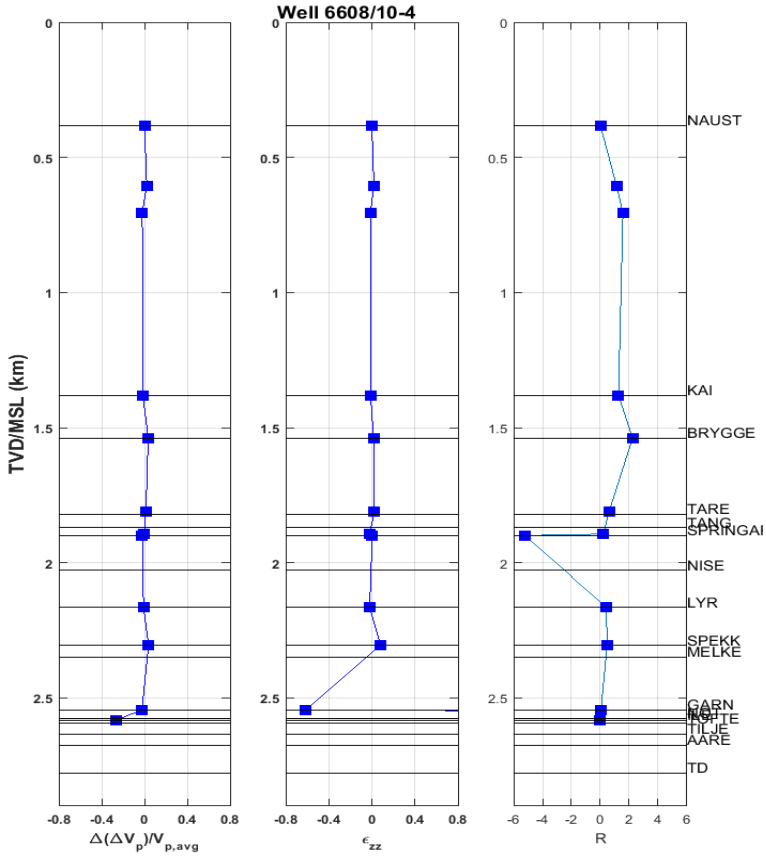

Figure C.12: The relative velocity change, strain and R-values versus depth in well 6608/10-4, using Method 2.

Appendix D

Vertical Strain Along a Disk-Shaped Reservoir using Geertsma's Nucleus of Strain Model

D.1 Geertsma's Nucleus of Strain

Geertsma's Nucleus of Strain Model is a numerical model that can be used to calculate stress and strain changes around a compacting reservoir [35]. The model can also be used to calculate how the compaction of a reservoir propagates through the overburden. Geertsma's strain model assume that superposition is allowable, and calculate the compaction of a small sphere, then calculate the total vertical displacement by adding the compaction of many such spheres. The model is only valid if there is no elastic contrasts between the reservoir and the surrounding rock, meaning that both the overburden and reservoir rock respond to stress change in the same manner. The parameters needed in order to model the displacement are listed in table (D.1) below.

The uniaxial compressibility, C_m, is the inverse of the uniaxial compaction modulus, as given by the equation below.

$$C_m = \frac{1}{E_{fr}} \frac{(1-\nu_{fr})(1-2\nu_{fr})}{1-\nu_{fr}} = \frac{1}{H_{fr}} \tag{D.1}$$

Displacement outside a depleting sphere, taking into account that the vertical stress is zero at the surface is given by [9],

Parameters	Description	SI-unit
D	Reservoir depth	m
R	Reservoir radius	m
z	Vertical depth	m
Δ h	Estimated reservoir compaction	m
h	Reservoir height	m
V	Volume of depleted region	m^3
G	Shear modulus	Pa
$\Delta\ p_f$	Pressure depletion	Pa
E_{fr}	Youngs modulus	Pa
C_m	Uniaxial compressiblity	Pa^{-1}
ν	Poisson's ratio	Dimensionless
α	Biot's coefficient	Dimensionless
H_fr	Uniaxial compaction modulus	Pa

Table D.1: Parameters in Geertsma's nucleus of strain model, equation (D.2).

$$\overrightarrow{u} = \frac{C_m}{4\pi}\left(\frac{\overrightarrow{R_1}}{R_1^3} + (3-4\nu)\frac{\overrightarrow{R_2}}{R_2^3} - \frac{6z(z+D)\overrightarrow{R_2}}{R_2^5} + \frac{2\hat{z}}{R_2^3}\Big[(3-4\nu)(z+D) - z\Big]\right) V\alpha\Delta p_f, \quad \text{(D.2)}$$

where the parameters used are given in table (D.1) above, in addition to R_1 and R_2 given as the distance from the nucleus to the surface point we are considering and the radius from the surface point at a distance -D from the surface, respectively.

If the vertical component ($\overrightarrow{R_1}$) is extracted from equation (D.2) and integrated over the reservoir, we get an approximate expression for the vertical displacement along the centre line through a disk-shaped reservoir,

$$u_z = -\frac{1}{2}C_m h\alpha\Delta p_f\left(3-4\nu + \frac{D-z}{|D-z|} - \frac{D-z}{\sqrt{R^2+(D-z)^2}} - \frac{(D+z)(3-4\nu)}{\sqrt{R^2+(D+z)^2}} + \frac{2R^2 z}{(R^2+(D+z)^2)^{3/2})}\right) \quad \text{(D.3)}$$

And by letting $z = 0$ we get the subsidence at the surface, as plotted in figure (D.1)

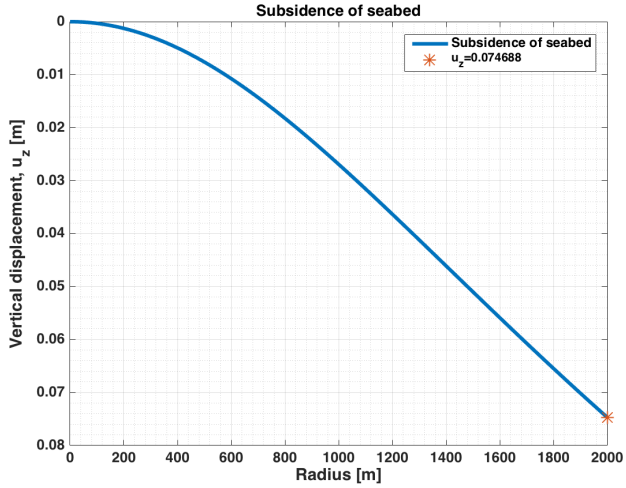

Figure D.1: Seabed subsidence versus radius

$$u_z = w = 2C_m h \alpha \Delta p_f (1-\nu)\left(1 - \frac{D}{\sqrt{D^2+R^2}}\right) \tag{D.4}$$

The expression for estimated reservoir compaction is a part of the equation above, and can be written as

$$\Delta h = C_m h \Delta p_f \tag{D.5}$$

D.1.1 Superposition

The principle of superposition is based on the theory of combining forces. When two or more single forces act simultaneously on an object, the total force that act on that object is equal to the vector sum of all the single forces. The sum of all the forces is called net force ($\overrightarrow{F}_{net}$), given by equation (D.6) below,

$$\overrightarrow{F}_{net} = \overrightarrow{F}_1 + \overrightarrow{F}_2 + ... + \overrightarrow{F}_n, \tag{D.6}$$

where $\overrightarrow{F}_n$ is the single force number n acting on the object, [28].

When using Geertsma's nucleus of strain model, calculation of the total sea floor subsidence is based on the principle of superposition. The subsidence caused by compaction of a small sphere is calculated, and then the total subsidence is

calculated by summing the influence of many small spheres, as in the equation below, as presented in [9]

$$u_{z,total} = u_{z,1} + u_{z,2} + ... + u_{z,n} = \sum_{n=1}^{N} u_{z,n} \tag{D.7}$$

where $u_{z,total}$ is the total subsidence and $u_{z,n}$ is the subsidence caused by compaction of sphere n, and N is the total number of spheres.

D.2 The R-factor

The R-factor, also known as the dilation factor, is a parameter that express how sensitive a rock is to strain changes, often induced by pressure depletion and compaction. The R-factor is related to the P-wave velocity and stress and strain in a formation. As the stress and strain increases with depth, so will the velocity. Thus, the R-factor is expected to be high in magnitude close to the seabed, and will quickly decrease with depth [36].

The R-factor was first derived by Røste [15] and Hatchell [11], and generalized alternatives have later been presented, such as the expression presented by Holt [36]. The determination of the R-factor is based on the fractional velocity and thickness change in a rock body.

The R-factor presented by Røste and Hatchell [15, 11] is expressed as

$$R = -\frac{\frac{\Delta V_p}{V_p}}{\frac{\Delta z}{z}} \tag{D.8}$$

The fractional change in path length is equal to the average vertical strain in that specific layer, thus $\frac{\Delta z}{z}$ can be replaced by ϵ_{zz}, the vertical component of the strain tensor, rewriting equation (D.8) to

$$\frac{\Delta V_p}{V_p} = -R\epsilon_{z_z} \tag{D.9}$$

D.3 Modeled Vertical Strain

The input parameters applied when modelling the vertical displacement along the centre-line of a disk shaped reservoir using Geertsma's nucleus of strain model

(equation (D.3)) are presented in table (D.2) below.

Parameter	**Symbol**	**Value**
Reservoir depth	D	2000 m
Reservoir radius	R	2000 m
Vertical depth	z	4000 m
Estimated compaction, assuming uniaxial deformation	$C_m h\ \Delta\ \mathrm{p}_f$	0.17 m
Reservoir thickness	h	100 m
Subsidence at the surface at $r = 0$	$u_z(z = 0)$	0.07 m
Shear modulus	G	2 GPa
Pore Pressure Depletion	$\Delta\ \mathrm{p}_f$	10 MPa
Poisson's ratio	ν	0.25
Biot's Coefficient	α	1 [9]
Density	ρ	2200 kg/m^3
Reservoir strain	Δ h/h	0.17%

Table D.2: Reservoir properties used when modelling vertical displacement along the centre of a disk shaped reservoir, [9]

Figure (D.2) displays the approximate solution to Geertsma's strain model versus depth, using input values presented in table D.2.

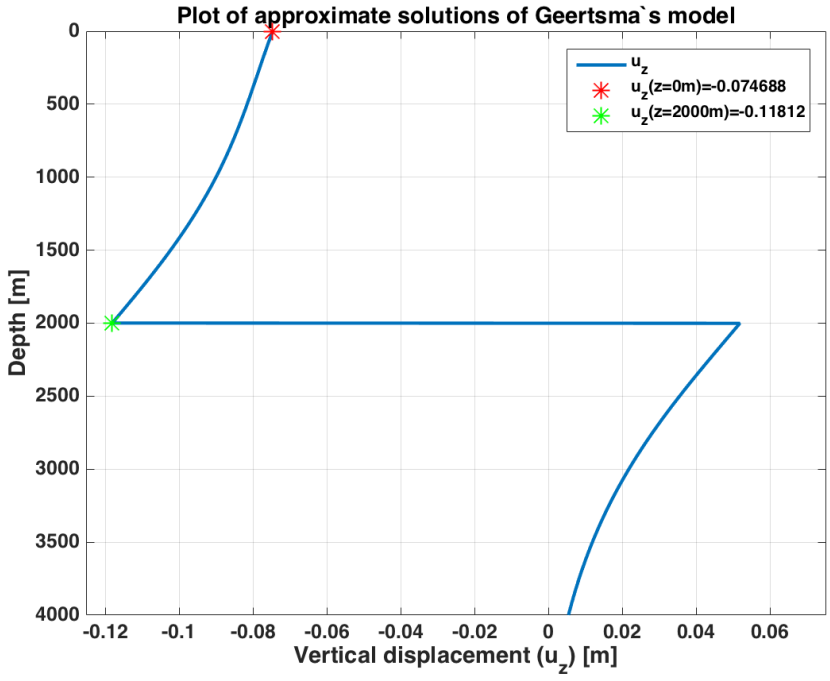

Figure D.2: Vertical displacement versus depth along the centre line of a disc shaped reservoir.